Large-Eddy Simulation of Turbulent Combustion

Heinz Pitsch

Department of Mechanical Engineering, Stanford University, Stanford, California 94305;
email: H.Pitsch@stanford.edu

Key Words

computational combustion, scalar mixing, scalar dissipation rate,
nonpremixed combustion, premixed combustion

Abstract

Large-eddy simulation (LES) of turbulent combustion is a relatively new research
field. Much research has been carried out over the past years, but to realize the full
predictive potential of combustion LES, many fundamental questions still have to be
addressed, and common practices of LES of nonreacting flows revisited. The focus
of the present review is to highlight the fundamental differences between Reynolds-
averaged Navier-Stokes (RANS) and LES combustion models for nonpremixed and
premixed turbulent combustion, to identify some of the open questions and modeling
issues for LES, and to provide future perspectives.

450

4-76

2. LES OF NONPREMIXED TURBULENT COMBUSTION

2.1. Overview

In nonpremixed combustion, fuel and oxidizer are initially separated. Chemical reactions occur only because of diffusive molecular mixing of these components. If the chemistry is fast enough, a reaction layer forms at approximately stoichiometric conditions. In this layer, fuel and oxygen are consumed and reaction products are formed. For hydrogen and hydrocarbon chemistry in engineering devices, combustion is typically controlled by the rate of molecular mixing, although the chemistry becomes important if the chemical timescale compares with the timescale of the turbulence. In that case, local flame extinction might occur. Also, the chemistry of pollutant formation is often governed by slow chemical reactions.

In RANS modeling it has long been realized that the direct closure of the mean chemical source term in the averaged species transport equations can hardly be accomplished, and conserved scalar methods have been used in many applications. Using so-called coupling functions, the rate of mixing of fuel and oxidizer can be described by a nonreactive scalar, the mixture fraction. Different definitions have been used for the mixture fraction (Bilger 1976, Pitsch & Peters 1998), but essentially the mixture fraction is a measure of the local equivalence ratio. Hence, the mixture fraction is a conserved scalar, independent of the chemistry. This leads to the so-called conserved scalar method, which forms the basis for most of the combustion models for nonpremixed turbulent combustion. Considering the simplest case of infinitely fast chemistry, all species mass fractions and the temperature are a function of mixture fraction only. If the subfilter probability distribution of the mixture fraction is known, the Favre-filtered mass fractions $\tilde{Y}_i$, for instance, can then be obtained as

$$\tilde{Y}_i = \int_0^1 Y_i(Z) f(Z)\, dZ, \tag{1}$$

where Z is the mixture fraction and $f(Z)$ is the marginal density-weighted filter probability density function (FPDF) of the mixture fraction. Applications of simple conserved scalar models in LES have been based on infinitely fast irreversible chemistry (Pierce & Moin 1998) and equilibrium chemistry (Cook & Riley 1994).

The flamelet model and the conditional moment closure (CMC) model are conserved scalar models that account for finite-rate chemistry effects. Many models that

4-17

have been formulated for LES are variants of these and some are discussed below. These models essentially provide state relationships for the reactive scalars as functions of mixture fraction and other possible parameters, such as the scalar dissipation rate. Filtered quantities are then obtained by a relation similar to Equation 1, but using a presumed joint FPDF of the mixture fraction and, for example, the scalar dissipation rate.

Because the probability density function (PDF) plays a central role in most models for nonpremixed combustion, it is necessary to emphasize the special meaning of the FPDF in LES. Here, the example of the marginal FPDF of the mixture fraction is discussed, but similar arguments can be made for the joint composition FPDF. In Reynolds-averaged methods, a one-point PDF can be determined by repeating an experiment many times and recording the mixture fraction at a given time and position in space. For a sufficiently large number of samples, the PDF of the ensemble can be determined with good accuracy. In LES, assuming a simple box filter, the data of interest is a one-time, one-point probability distribution in a volume corresponding to the filter size surrounding the point of interest. If an experimentally observed spatial mixture fraction distribution is considered at a given time, the FPDF cannot simply be evaluated from these data, because the observed distribution is characteristic of this particular realization and it is not a statistical property. As a statistical property, the FPDF must be defined by an ensemble that can potentially have an arbitrary large number of samples. In the context of transported PDF model formulations for LES, which are discussed below, Pope (1990) introduced the notion of the filtered density function (FDF), which describes the local subfilter state of the considered experiment. The FDF is not an FPDF, because it describes a single realization. The FPDF is defined only as the average of the FDF of many realizations given the same resolved field (Fox 2003). It is important to distinguish between the FDF and the FPDF, especially in using direct numerical simulation (DNS) data to evaluate models, and in the transported FDF models discussed below. Only the FDF can be evaluated from typical DNS data, whereas the FPDF is required for subfilter modeling.

For conserved scalar models, a presumed shape of the FPDF has to be provided. Similar to RANS models, a beta-function distribution is usually assumed for the marginal FPDF of the mixture fraction, and parameterized by the first two moments of the mixture fraction. The filtered mixture fraction is determined by the solution of a transport equation, whereas algebraic models are mostly used for the subfilter scalar variance. The beta-function is expected to be a better model for the FPDF in LES than for the PDF in RANS, because the FPDF is generally more narrow, and hence the exact shape is less important. It can also be expected that intermittency, which is a main source of error when using the beta-function in RANS, will mostly occur on the resolved scales. The validity of the beta-function representation of the FPDF of the mixture fraction has been investigated by several authors using DNS data of nonpremixed reacting flows of both constant and variable density (Cook & Riley 1994, Jimenez et al. 1997, Wall et al. 2000). The main conclusion of these studies is that the beta-function distribution provides a good estimate for the FPDF of the mixture fraction and that this estimate is even better in LES than in RANS models. Furthermore, the model is particularly good when evaluated using the mixture fraction variance

454

taken from DNS data, suggesting that the beta-function as a model for the statistical distribution of the mixture fraction performs much better than the commonly used subgrid-scale models for the mixture fraction variance. However, recent studies by Tong (2001) and Tong et al. (2005) show that the FPDF often substantially deviates from the beta-function. This is discussed in more detail below.

In the following, different variants of the flamelet model, the CMC model, and the transported FDF model are discussed in more detail. Because all such models require the scalar dissipation rate, modeling of this quantity is discussed first.

2.2. Modeling the Scalar Dissipation Rate

Although different conceptual ideas and assumptions are used in the combustion models discussed here, most of them need a model for the scalar dissipation rate. The dissipation rate of the mixture fraction is a fundamental parameter in nonpremixed combustion, which determines the filtered reaction rates, if combustion is mixing controlled. High rates of dissipation can also lead to local or global flame extinction. Models based on presumed FPDFs also require a model for the subfilter scalar variance. Here, the most commonly used model formulations for LES are reviewed briefly, differences with the typical RANS models are pointed out, and potential areas of improvement are discussed.

An illustration of the importance of the scalar variance and dissipation rate in LES of nonpremixed combustion modeling is given by the following example. Pope (2004) pointed out that LES is an incomplete model if the filter size can be arbitrarily specified. This is an important issue, especially for combustion LES, because of the importance of the subfilter models. To fix the arbitrariness of the filter, Raman & Pitsch (2005a) proposed a recursive filter refinement method, where the local filter width is determined such that the ratio of subfilter scalar variance to the maximum possible variance is smaller than a specified value. The maximum possible variance can be expressed in terms of the resolved mixture fraction as $\tilde{Z}(1 - \tilde{Z})$. It was demonstrated in the simulation of a bluff-body stabilized flame that this method better resolves high scalar variance and dissipation regions, which leads to significant improvement in results. Some of these results are shown in **Figure 1**.

In RANS models, typically a transport equation is solved for the scalar variance $\langle Z'^2 \rangle$, in which the Reynolds-averaged scalar dissipation rate $\langle \chi \rangle$ appears as an unclosed sink term that requires modeling. The additional assumption of a constant ratio of the integral timescale of the velocity τ_t and the scalar fields leads to the expression

$$\langle \chi \rangle = c_\phi \frac{1}{\tau_t} \langle Z'^2 \rangle, \qquad (2)$$

where c_ϕ is the so-called timescale ratio.

In the models most commonly used in LES (Girimaji & Zhou 1996, Pierce & Moin 1998), the scalar variance transport equation and the timescale ratio assumption are actually used in the opposite sense. Instead of solving the subfilter variance equation, the assumption that the scalar variance production appearing in that equation equals the dissipation term leads to an algebraic model for the dissipation rate of the form
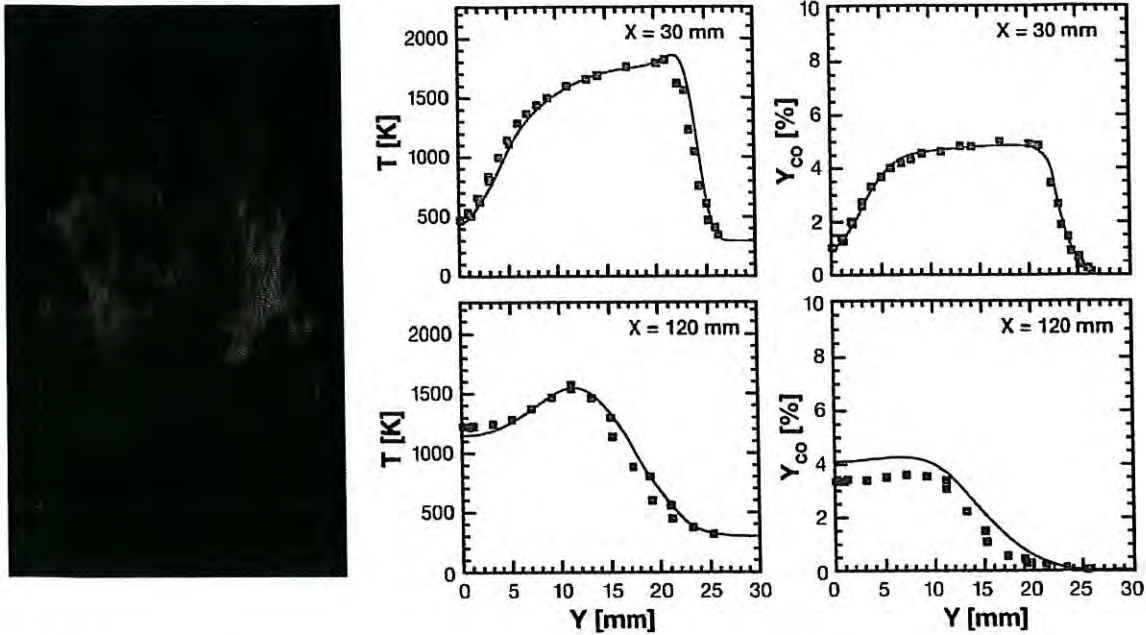
455

4-19

Figure 1

Results from large-eddy simulation of the Sydney bluff-body flame (Raman & Pitsch 2005a). Flame representation from simulation results (*left*) and time-averaged radial profiles of temperature and CO mass fraction at $x = 30$ mm and $x = 120$ mm, which are in and downstream of the recirculation region, respectively. The left figure shows computed chemiluminescence emissions of CH collected in an observation plane with a ray tracing technique (M. Hermann, private communication). Experimental data are taken from Dally et al. (1998).

$$\tilde{\chi} = 2D_t \left(\nabla \tilde{Z}\right)^2, \tag{3}$$

where an eddy diffusivity model was used for the subfilter scalar flux in the production term. $D_t = (c_Z\Delta)^2 \tilde{S}$ is the eddy diffusivity, where c_Z can be determined using a dynamic procedure and $\tilde{S} = |2\tilde{S}_{ij}\tilde{S}_{ij}|^{1/2}$ is the characteristic Favre-filtered rate of strain. Writing Equation 2 for the subfilter scales and combining it with Equation 3 then leads to the model for the scalar variance

$$\widetilde{Z'^2} = c_V\Delta^2 \left(\nabla \tilde{Z}\right)^2, \tag{4}$$

where $\tau_{t,\Delta} \sim 1/\tilde{S}$ is assumed, and a new coefficient c_V is introduced, which can be determined dynamically following Pierce & Moin (1998). From Equations 2 and 3, and the dynamically determined coefficients of the eddy diffusivity and the scalar variance, the timescale ratio c_ϕ can be determined as $c_\phi = 2c_Z^2/c_V$.

Alternative models for LES, where a transport equation for the scalar variance is solved, have also been proposed (Jiménez et al. 2001). It seems that then the production/dissipation balance assumption would not be required, but this is not the case. The assumption of constant timescale ratio still has to be made and an equation of

4-2B

the form of Equation 2 implicitly assumes that production equals dissipation. This is because the dissipation rate can only be used in evaluating the timescale at the filter scale, if the scale invariance assumption is made for the scalar dissipation rate. This assumption implies that production is equal to dissipation.

Although the production/dissipation balance assumption seems to be inherently used in all models for the dissipation rate, there is strong evidence that it is not always applicable, which might have severe consequences for turbulent combustion modeling. Tong (2001) showed from filtering experimental data in nonreactive jets that the occurrence of so-called ramp-cliff structures leads to locally high scalar dissipation rates and bi-modal subfilter distributions of the conserved scalar, which cannot be described by the beta-function distribution. Because the ramp-cliff structures are a direct result of the large-scale turbulent motion, and not of the energy cascade, they cannot be described by the production/dissipation balance assumption. More recently, the same conclusions were found by analyzing experimental data of a jet diffusion flame (Tong et al. 2005). Although the bi-modal FDFs are observed with a low probability (roughly 15% in the diffusion flame experiment at $x/D = 15$), because of the locally high dissipation rates, these might be very important for the dynamics of the flame structure. This also indicates that the accuracy of mixing models used in transported FDF models in LES is very important.

Another complication of using models for scalar variance and dissipation rate in LES is of numerical nature. It is common practice in nonreactive, as in combustion, LES to use implicit filtering, which means that the filter is given by the numerical grid spacing. It follows that the smallest resolved scales are actually under-resolved. Because of numerical diffusion, the energy content of these scales is underpredicted. For nonreactive LES, this is usually less important, because the flow dynamics are mostly governed by the large scales of the turbulence. For reactive flows this is different: As shown by Equations 3 and 4, the models for scalar dissipation rate and variance depend on the square of the resolved scalar gradient. This quantity, however, is largest on the smallest resolved scales. Similarly, the production term in the scalar variance equation depends on the same quantity, and therefore the solution of the scalar variance equation also underpredicts the scalar variance. Consequently, models of the form of Equation 3 or 4, or models involving the subfilter variance transport equation, should only be used with explicit filtering or numerical schemes of higher-order accuracy.

Clearly, there is a need for new modeling approaches for scalar variance and dissipation rate that account for the small-scale structure of the scalar field.

2.3. Models for Nonpremixed Combustion LES

2.3.1. Steady and unsteady flamelet models.
Flamelet models for nonpremixed combustion were introduced by Peters (1983, 1984). The basic assumption is that the chemical timescales are short enough that reactions occur in a thin layer around stoichiometric mixture on a scale smaller than the small scales of the turbulence. This has two consequences: The structure of the reaction zone remains laminar, and diffusive transport occurs essentially in the direction normal to the surface of

4-21

stoichiometric mixture. Then, the scalar transport equations can be transformed to a system where the mixture fraction is an independent coordinate. A subsequent asymptotic approximation leads to the flamelet equations,

$$\frac{\partial Y_i}{\partial \tau} - \rho \frac{\chi}{2} \frac{\partial^2 Y_i}{\partial Z^2} - \dot{m}_i = 0, \tag{5}$$

where τ is the time, ρ is the density, and $\dot{m}_i$ are the chemical production rates. Similar equations can be derived for other scalars such as temperature. The steady laminar flamelet model is developed by assuming the flame structure is in steady state. Then, the time derivative in Equation 5 can be neglected. The solution is then only a function of the scalar dissipation rate and the boundary conditions, and can be precomputed and tabulated in terms of these quantities. This model was considered in some of the early a priori studies of LES combustion models (Cook & Riley 1998, De Bruyn Kops et al. 1998) and has also been successfully applied in simulations of experimental configurations (Kempf et al. 2003, Raman & Pitsch 2005a).

The steady flamelet model is often used, especially in LES, because of its simplicity and considerable improvements over fast chemistry assumptions. However, the steady-state assumption is inaccurate if slow chemical or physical processes have to be considered (Pitsch et al. 1998). Examples of such processes include the formation of pollutants and radiative heat transfer. In these cases, the full unsteady equations should be solved.

Pitsch & Steiner (2000a,b) used the Lagrangian flamelet model (LFM) (Pitsch et al. 1998) as a subfilter combustion model for LES in an application to a piloted methane/air diffusion flame (Barlow & Frank 1998) using a 20-step reduced chemical scheme based on the GRI 2.11 mechanism (Bowman et al. 1995). The unsteady flamelet equations are solved coupled with the LES solution to provide the filtered density and other filtered scalar quantities using a presumed FPDF of the mixture fraction. The scalar dissipation rate required to solve Equation 5 is determined from the LES fields as a cross-sectional conditionally averaged value using a model similar to the conditional source term estimation method by Bushe & Steiner (1999), which is described below. The unconditional scalar dissipation rate was determined from a dynamic model (Pierce & Moin 1998). This study is the first demonstration of combustion LES of a realistic configuration using a detailed description of the chemistry. The results are promising, especially for NO, but because of the cross-sectional averaging of the scalar dissipation rate, local fluctuations of this quantity are not considered and the potential of LES is not fully realized. Also, this model cannot be easily applied in simulations of more complex flow fields. In a more recent formulation, the Eulerian flamelet model (Pitsch 2002), the flamelet equations are rewritten in an Eulerian form, which leads to a full coupling with the LES solver, and thereby enables the consideration of the resolved fluctuations of the scalar dissipation rate in the combustion model. Examples of the results are shown in **Figure 2**. The resolved scalar dissipation rate field is dominated by features occurring on the large scale of the turbulence. Layers of high dissipation rate alternate with low dissipation rate regions. In the LFM results, as well as in several earlier RANS-type modeling studies (Barlow 2000), where these fluctuations are not considered, some heat

458

LES of Pitsch gives good agreement with CO + NO profiles - jet flame

Temperature distribution

Scalar dissipation rate distribution

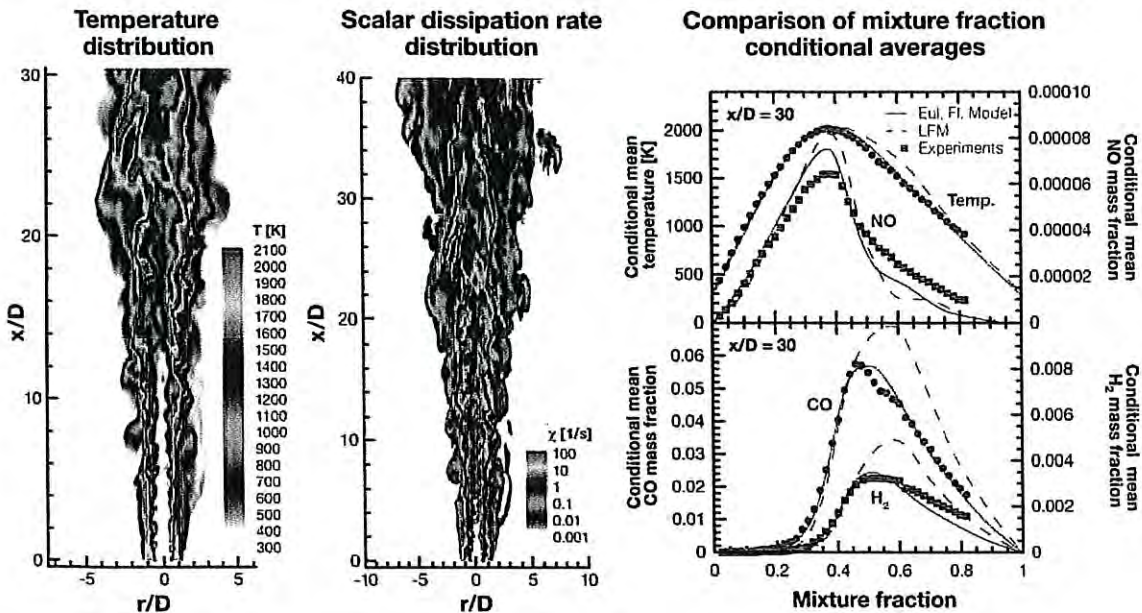**Comparison of mixture fraction conditional averages**

Figure 2

Results from large-eddy simulation of Sandia flame D (Pitsch 2002, Pitsch & Steiner 2000a) using the Eulerian flamelet model (*solid lines*) and the Lagrangian flamelet model (*dashed lines*) compared with experimental data of Barlow & Frank (1998). Temperature distribution (*left*), scalar dissipation rate distribution (*center*), and comparison of mixture fraction–conditioned averages of temperature and mass fractions of NO, CO, and H_2 at $x/D = 30$.

release occurs on the rich partially premixed side of the flame, which leads to strong CO formation in these regions. Accounting for the richness of the predicted spatial distribution of the scalar dissipation rate substantially improves the comparison with the experimental data by suppressing the heat release in the rich regions, and hence the formation of CO.

2.3.2. Flamelet/Progress variable method. A model that was developed specifically for LES is the flamelet/progress variable model (FPV) by Pierce & Moin (2001, 2004). The model uses a steady-state flamelet library, but is substantially different from the typical steady laminar flamelet model (SLFM) used by others (Branley & Jones 2001, Cook & Riley 1998, De Bruyn Kops et al. 1998, Kempf et al. 2003). Instead of using the scalar dissipation rate as a parameter in the flamelet library, the reaction progress variable is used for the parameterization. A transport equation is solved for the filtered reaction progress variable, which can, for example, be defined as the sum of the mass fractions of CO_2, H_2O, CO, and H_2. The filtered chemical source term in this transport equation is closed using the flamelet library and a presumed joint FPDF of mixture fraction and reaction progress variable. The advantage of this different way of parameterizing the flamelet library is that it potentially gives a better description of local extinction and reignition phenomena and of flame

459

4-23

liftoff. Steady-state solutions of Equation 5 exist for all possible values of the reaction progress variable below the equilibrium value and can be used in the flamelet library. For higher scalar dissipation rates, the reaction progress variable becomes smaller because of diffusive effects until extinction occurs, where the solution jumps to the nonburning state. If the scalar dissipation rate is used in the parameterization, only the burning solutions are available.

One challenge of using the reaction progress variable is that, in order to close the model, the joint FPDF of mixture fraction and reaction progress variable needs to be provided. In the application of the model to a nonpremixed dump combustor geometry by Pierce & Moin (2001, 2004), a delta-function was used for the FPDF of the reaction progress variable. Comparison with experimental data demonstrated substantial improvement of the predictions compared with SLFM, caused by a more accurate description of the flame stabilization region. The FPV model can be interpreted as a two-variable intrinsically low dimensional manifold (ILDM) model (Maas & Pope 1992), where the ILDM tabulation is generated with a flamelet model.

In a priori tests using data from DNS of nonpremixed combustion in isotropic turbulence (Sripakagorn et al. 2004), Ihme et al. (2004) investigated potential areas for improvement of the FPV model. The model for the presumed FPDF for the reaction progress variable was identified as important. It was also found that the steady-state assumption of the flamelet solutions, especially during reignition at low scalar dissipation rate, is inaccurate. The beta function was proposed as a possible improvement for the reaction progress variable FPDF, and a closure model for the reactive scalar variance equation was provided. New developments include the evaluation and application of the statistically most likely distribution (Pope 1979) as a new model for the reactive scalar FPDF (Ihme & Pitsch 2005), and the extension of the model to an unsteady flamelet library formulation (Pitsch & Ihme 2005).

2.3.3. Conditional moment closure. In the CMC model, originally proposed in a RANS context by Klimenko (1990) and Bilger (1993), transport equations are derived for mixture fraction–conditioned averages of the reactive scalars. The resulting equations are dependent on time, three spatial dimensions, and the mixture fraction. The mixture fraction conditioning greatly simplifies the modeling of the averaged chemical source term, but makes it difficult to solve these equations in LES. Kim & Pitsch (2005) formulated the CMC model for LES. Models are provided for all unclosed terms, and most of the models are tested using DNS data. Also, a lower-dimensional model is developed and tested, where the number of independent spatial coordinates was reduced by integrating the reactive scalar transport equations in one direction. For first-order closure, this model is very similar to the Eulerian flamelet model (Pitsch 2002). Higher-order closure changes the modeling of the unclosed terms in the CMC model, whereas in the Eulerian flamelet model, ensembles of flamelets would be computed simultaneously. For an application of the full CMC model in LES of a practical configuration, several issues regarding boundary conditions and numerical efficiency are important and have to be addressed (Bilger et al. 2005, Kim & Pitsch 2005).

Another interesting formulation of the CMC model for LES is the so-called conditional source term estimation model by Bushe & Steiner (1999). Here, transport

equations are solved for all reactive scalars appearing in the applied chemical scheme. The chemical source terms are closed using the conditionally averaged scalar values and the mixture fraction FPDF. The CMC concept is used to determine the conditionally filtered scalars from the unconditional values obtained from the solution of the transport equations. For this, the integrals of the form of Equation 1 are inverted for a certain region of the flow field using the presumed mixture fraction FPDF and assuming homogeneous statistics in that region. It is apparent that the model cannot be used for radical species, which peak in thin layers on the subfilter scale. It is also important that the assumption of statistical homogeneity, which is used in the deconvolution, has to be restricted to regions smaller than the large scales of the turbulence, because, otherwise, the full potential of LES is again not realized.

2.3.4. Transported FDF models. The transported joint scalar and joint scalar/velocity PDF method has been applied to turbulent reacting flows using RANS methods in many studies (Chen et al. 1989, Pope 1985, Saxena & Pope 1998, Xu & Pope 2000), and has also been extended to LES by using the FDF originally introduced by Pope (1990) and further studied and extended by Gao & O'Brien (1993), Colucci et al. (1998), Sheikhi et al. (2003), and others. The transport equation for the one-point one-time joint FDF of all reactive scalars and temperature or enthalpy is given by

$$\frac{\partial F}{\partial t} + \nabla \cdot (\tilde{\mathbf{v}} F) + \nabla \cdot (\widetilde{\mathbf{v}' | \psi} F) = -\frac{\partial}{\partial \psi} \left[\left(\frac{1}{\rho} \overline{\nabla \cdot \rho D \nabla \phi | \psi} + \mathbf{S}(\psi) \right) F \right], \quad (6)$$

where $F(\psi)$ is the density-weighted FDF, t is the time, $\mathbf{v}$ is the velocity, ϕ and ψ are the vector of scalars and its sample space representation, respectively, and D is the molecular diffusivity. The tilde stands for mass weighted, the overline for conventional filtering, and the prime for a fluctuation. In Equation 6, the chemical source term $\mathbf{S}(\psi)$ appears in closed form. Molecular mixing, however, depends on multipoint information and therefore has to be modeled. This is a severe restriction of the transported FDF models for applications in combustion, where transport is usually rate controlling, and hence more important than the details of the chemistry. Because molecular mixing occurs on the smallest scales, the mixing models used in LES so far are the same as those developed for RANS.

The joint scalar FDF depends on space, time, and all independent scalars. Therefore, the FDF transport equation cannot be solved using finite-volume or finite-difference methods and is commonly represented by an equivalent system of notional particles. For each particle, ordinary differential equations are solved for particle motion, temperature or enthalpy, and species mass fractions (Pope 1985). Because the accuracy of the method scales with the square root of the number of notional particles, typically a large number of particles per cell is required. If the error of the method with only one particle per cell is estimated to be the root mean square of the described quantity, then 100 particles per cell are required to achieve an error on the order of 10% of the root mean square (RMS). For RANS simulations of statistically stationary problems, good statistics can be achieved by collecting large ensembles of particles over time.

The main challenges in applying FDF methods in LES are the computational cost and the formulation of robust and consistent algorithms. Because of the inherent unsteadiness in LES, the requirement of statistical convergence has to be satisfied at each time step. For an LES with 2 million cells and 100 particles per cell, approximately 200 million particles are required. For each of these particles, the equations for the species mass fractions have to be solved. Especially the integration of the chemical source terms is very time consuming and renders the FDF method in LES virtually impossible without special treatment of the chemical source terms. Pope (1997) proposed the in situ adaptive tabulation (ISAT) method for the chemical source term integration, and has demonstrated substantially reduced integration times for applications in RANS. The assessment and algorithmic optimization of the method in LES was recently initiated by Lu et al. (2004).

To reduce the cost of FDF/LES, it is desirable to use a small number of particles per cell. Applications of the FDF method in LES show that if a practical number of 50 particles per cell is used, large fluctuations in the filtered density occur because of statistical errors, causing problems for numerical solvers. Muradoglu et al. (1999) proposed a hybrid scheme, which considerably improves the robustness of the method. Here, a transport equation for the energy is solved. The chemical source term in that equation is evaluated from the joint PDF, which can be evaluated from the particles. Using this method, the filtered density can be evaluated in three different fashions: from the particle weights, which are assigned at the beginning of the simulation and which are fixed in time; from the joint composition FDF; and from the solution of the energy equation. It is important to ensure time-accurate consistency of these densities throughout the simulation. Zhang & Haworth (2004) have provided an appropriate algorithm for unsteady RANS. For LES, more work is still required.

Applications of the transported FDF method to realistic flame geometries have mostly been restricted to solving for the FDF of the mixture fraction in combination with the laminar flamelet model (Raman et al. 2005, Sheiki et al. 2005). However, although the application of the transported FDF method substantially increases computational times, the feasibility of the method for LES has been demonstrated in simulations of the Sandia flames D and E with a reduced 17-step mechanism based on the GRI-2.11 mechanism (Raman & Pitsch 2005b). These simulations used a mesh of approximately 3 million computational cells. For mixing, the interaction-by-exchange-with-the-mean (IEM) model was employed with the timescale ratio determined from a dynamic model. Results for flame E, where local extinction and reignition is important, are shown in **Figure 3**. The conditional averages show that, because of local extinction, unreacted molecular oxygen remains even at stoichiometric conditions ($Z_{st} = 0.35$). Comparisons for other species show generally good agreement, but the CO mass fraction, for instance, is overpredicted at rich conditions. Extinguished parts of the flame can also be seen in the instantaneous temperature field given for flame E.

Finally, note that usually in applications of transported FDF methods in LES the difference between the FDF, as a description of a single subfilter realization, and the FPDF, as the probability of finding a certain subfilter composition, has not been considered. This distinction is not unique to FDF and FPDF. It also needs to be considered for all other filtered quantities, such as the filtered velocities and the
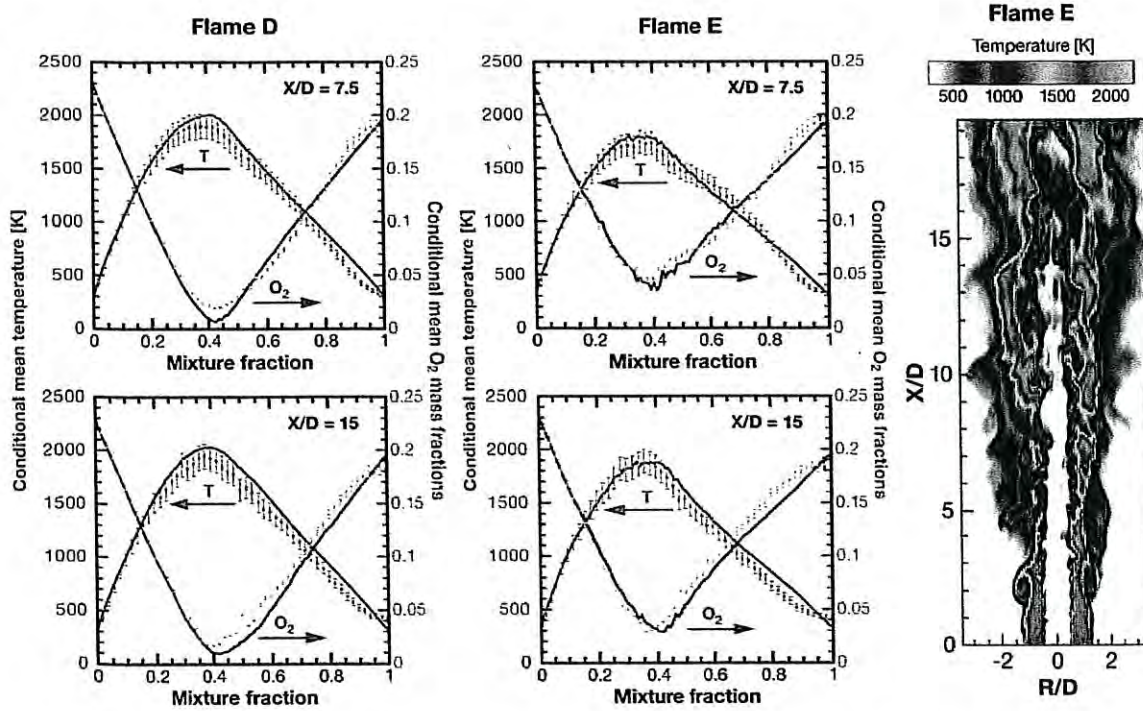
Figure 3

Results from large-eddy simulation of Sandia flame D and flame E (Raman & Pitsch 2005b) using the transported filtered density function model compared with experimental data of Barlow & Frank (1998). Comparison of mixture fraction–conditioned averages of temperature and O_2-mass fractions at $x/D = 7.5$ and $x/D = 15$ and temperature distribution (*right*). The extent of local extinction can be seen in the mass fraction of unburned O_2 at stoichiometric conditions ($Z_{st} = 0.35$) and is apparent in the instantaneous temperature field.

subfilter stress tensor. For these, however, this is usually done implicitly by modeling the unclosed subfilter terms in a statistical sense, which also implies that the filtered quantity obtained from the solution of the modeled equations has statistical meaning. Similarly, modeling of the mixing term in the FDF equation cannot be done for a single subfilter realization, but only for a statistical distribution on the subfilter scale. Therefore, to model the transport equation, it has to be written for the FPDF rather than the FDF.

12.9.2 Filtered Navier-Stokes Equations

The governing equations employed for LES are obtained by filtering the time-dependent Navier-Stokes equations in either Fourier (wave-number) space or configuration (physical) space. The filtering process effectively filters out the eddies whose scales are smaller than the filter width or grid spacing used in the computations. The resulting equations thus govern the dynamics of large eddies.

A filtered variable (denoted by an overbar) is defined by

$$\overline{\phi}(\mathbf{x}) = \int_{\mathcal{D}} \phi(\mathbf{x}')G(\mathbf{x}, \mathbf{x}')d\mathbf{x}' \qquad (12.9\text{-}1)$$

where $\mathcal{D}$ is the fluid domain, and G is the filter function that determines the scale of the resolved eddies.

In **FLUENT**, the finite-volume discretization itself implicitly provides the filtering operation:

$$\overline{\phi}(\mathbf{x}) = \frac{1}{V} \int_{\mathcal{V}} \phi(\mathbf{x}')\, d\mathbf{x}', \quad \mathbf{x}' \in \mathcal{V} \qquad (12.9\text{-}2)$$

here V is the volume of a computational cell. The filter function, $G(\mathbf{x}, \mathbf{x}')$, implied here is then

$$G(\mathbf{x}, \mathbf{x}') \begin{cases} 1/V, & \mathbf{x}' \in \mathcal{V} \\ 0, & \mathbf{x}' \text{ otherwise} \end{cases} \qquad (12.9\text{-}3)$$

The LES capability in **FLUENT** is applicable to compressible flows. For the sake of concise notation, however, the theory is presented here for incompressible flows.

Filtering the Navier-Stokes equations, one obtains

$$\frac{\partial \rho}{\partial t} + \frac{\partial}{\partial x_i}(\rho \overline{u}_i) = 0 \qquad (12.9\text{-}4)$$

and

$$\frac{\partial}{\partial t}(\rho \overline{u}_i) + \frac{\partial}{\partial x_j}(\rho \overline{u}_i \overline{u}_j) = \frac{\partial}{\partial x_j}\left(\mu \frac{\partial \sigma_{ij}}{\partial x_j}\right) - \frac{\partial \overline{p}}{\partial x_i} - \left(\frac{\partial \tau_{ij}}{\partial x_j}\right) \qquad (12.9\text{-}5)$$

sgs

↑ new subgrid scale term to be modeled

where σ_{ij} is the stress tensor due to molecular viscosity defined by

4-28

$$(12.9\text{-}6)$$

Indeed, this term can be re-written as $T_{ll} = \gamma M^2_{sgs} \bar{p}$ where M_{sgs} is the subgrid Mach number. This subgrid Mach number can be expected to be small when the turbulent Mach number of the flow is small.

FLUENT offers four models for μ_t: the Smagorinsky-Lilly model, the dynamic Smagorinsky-Lilly model, the WALE model, and the dynamic kinetic energy subgrid-scale model.

Subgrid-scale turbulent flux of a scalar, ϕ, is modeled using s subgrid-scale turbulent Prandtl number by

$$q_j = -\frac{\mu_t}{\sigma_t}\frac{\partial \phi}{\partial x_j} \qquad (12.9\text{-}14)$$

where q_j is the subgrid-scale flux.

In the dynamic models, the subgrid-scale turbulent Prandtl number or Schmidt number is obtained by applying the dynamic procedure originally proposed by Germano [116] to the subgrid-scale flux.

Smagorinsky-Lilly Model

This simple model was first proposed by Smagorinsky [337]. In the Smagorinsky-Lilly model, the eddy-viscosity is modeled by

$$\mu_t = \rho L_s^2 \left|\bar{S}\right| \qquad (12.9\text{-}15)$$

Same formulas as Kuo for $\nu_T = \dfrac{\mu_t}{\rho}$

where L_s is the mixing length for subgrid scales and $\left|\bar{S}\right| \equiv \sqrt{2\bar{S}_{ij}\bar{S}_{ij}}$ In FLUENT, L_s is computed using

$$L_s = \min\left(\kappa d, C_s V^{1/3}\right) \qquad (12.9\text{-}16)$$

where κ is the von Kármán constant, d is the distance to the closest wall, C_s is the Smagorinsky constant, and V is the volume of the computational cell.

Lilly derived a value of 0.17 for C_s for homogeneous isotropic turbulence in the inertial subrange. However, this value was found to cause excessive damping of large-scale fluctuations in the presence of mean shear and in transitional flows as near solid boundary, and has to be reduced in such regions. In short, C_s is not an universal constant, which is the most serious shortcoming of this simple model. Nonetheless, C_s value of around 0.1 has been found to yield the best results for a wide range of flows, and is the default value in **FLUENT**.

4-29

12.18 Setting Up the Large Eddy Simulation Model

If you choose the LES model, the following subgrid-scale submodels are available (Section 12.19.15):

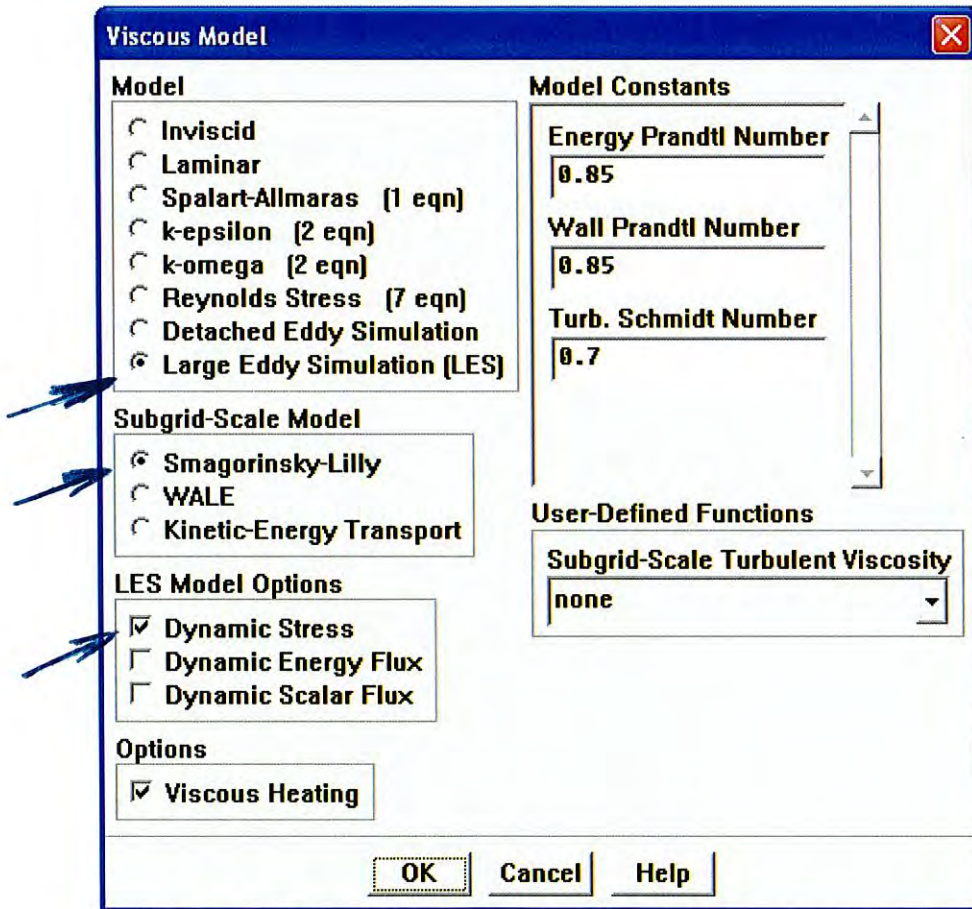- Smagorinsky-Lilly

- WALE

- Kinetic-Energy Transport

Figure 12.18.1: The **Viscous Model** Panel Displaying the Large Eddy Simulation Model Options

The LES options that are available for the Smagorinsky-Lilly are

- Dynamic Stress

- Dynamic Energy Flux (available only when the Dynamic Stress Model is enabled)

- Dynamic Scalar Flux

4-30

SLF = steady laminar
flamelet model
LES non premixed

Large-eddy simulation of a bluff-body stabilized nonpremixed flame

A. Kempf [a,b,*], R.P. Lindstedt [a], J. Janicka [b]

[a] *Thermofluids Division, Department of Mechanical Engineering, Imperial College London, London SW7 2AZ, UK*
[b] *Chair for Energy and Powerplant Technology, Department of Mechanical Engineering, Darmstadt Technical University, Petersenstr. 30, 64287 Darmstadt, Germany*

Abstract

Large-eddy simulations have been performed for a turbulent nonpremixed bluff-body stabilized CH_4:H_2 (50:50 vol.) flame at a Reynolds number of 15,800. The corresponding isothermal flow has also been computed. The Sydney bluff-body burner under consideration has been investigated experimentally by Masri and co-workers, who obtained velocity and scalar statistics. The focus of the current work is on flow and mixing effects with the thermochemistry evaluated using a steady-state laminar flamelet approach. The incompressible (low-Mach-number) governing equations for mass, momentum, and mixture-fraction have been solved on a structured cylindrical grid and resolution effects investigated using up to 3.643×10^6 nodes. The corresponding nonreactive case was resolved by 5.76×10^5 nodes, resulting in a resolution of more than 80% of the turbulence kinetic energy. The reacting case yields a resolution in excess of 75% on the finest grid—arguably sufficient to permit conclusions regarding the accuracy of submodels. Comparisons with experimental data show that for high resolutions comparatively good agreement is obtained for the flow field and for species other than nitric oxide. However, resolution effects are important and results obtained with 4.51×10^5 nodes show that a resolution of less than 70% of the turbulent kinetic energy is insufficient in the context of the Smagorinsky subgrid model combined with the dynamic procedure of Germano. The latter result is consistent with the analysis of Pope.
© 2005 The Combustion Institute. Published by Elsevier Inc. All rights reserved.

Keywords: LES; Flamelet; Nonpremixed; Turbulent; Bluff-body

1. Introduction

Large-eddy simulation (LES)-based techniques are becoming widely accepted as contenders to succeed the Reynolds-averaged Navier–Stokes simulation (RANS) approach to the computation of nonreactive turbulent flows away from solid boundaries. For reactive flows the situation is less clear with chemical reaction and heat release occurring in the fine (unresolved) scales. The influence of persistent non-gradient transport is also a particular problem in the context of premixed or partially premixed combustion. Many of the challenges associated with the inclusion of thermochemistry related terms are shared by the approaches of LES and RANS. Accordingly, many LES techniques for combusting flows are typically developed on the basis of already existing theories for turbulent reacting flows. A discussion of early

* Corresponding author.
  E-mail address: a.kempf@imperial.ac.uk (A. Kempf).

4–31

contributions can be found in the review presented by Vervisch and Poinsot [1].

Cook and Riley [2] presented a subgrid model for chemical reactions based on equilibrium chemistry and subsequently extended the model to a steady flamelet approach (see [3,4]). A posteriori analysis based on DNS data was also performed [5]. Branley and Jones [6] applied an equilibrium chemistry model for hydrogen combustion to an LES of a jet diffusion flame, leading to results that they found in reasonable accord with measurements. Forkel and Janicka [7,8] presented an efficient method for the LES of diffusion flames based on the assumption of equilibrium chemistry. Good results were obtained, but at the expense of significant numerical problems. Kempf et al. [9] extended this work to include a steady flamelet model and improved the numerical methods. Pitsch and Steiner [10,11] removed some of the limitations in the thermochemistry by applying an unsteady flamelet model to simulate the piloted Sandia/Sydney/Darmstadt D flame with encouraging results. Steiner and Bushe [12] applied the CME (conditional moment estimation) approach, a derivative of the CMC (conditional moment closure) approach developed by Bilger and Klimenko [13], to the same flame. Pitsch [14] also recently obtained results for the SANDIA D flame using an improved flamelet model that takes into account fluctuations in the scalar dissipation rate. The latter study resulted in improved predictions of the flame structure. Large-eddy simulations for complex configurations have also been performed and, typically, resolution issues come to the fore, with the inevitable consequence that more physics is relegated to the unresolved scales. Calhoon and Menon [15] accordingly developed a new subgrid model, featuring the linear eddy mixing model (LEM) of Kerstein [16], which was applied with promising results to aero-engine combustors.

A potential strength of LES techniques is associated with the more accurate flow field statistics. The present work attempts to fill the gap between LES of laboratory flames, which are well suited to model development, and the application to complicated combustors, which typically do not provide detailed information on the performance of model components. The current work accordingly considers the Sydney bluff-body burner [17,18], which features a nonpremixed flame stabilized in the recirculation zone downstream of a bluff body. Similar stabilization mechanisms are used in many technical applications. The geometry has proven surprisingly challenging due to an outer shear layer instability that is strongly influenced by boundary conditions [19–22]. Past studies include those of Dally et al. [18], who applied a Reynolds stress model, Kim [19], who used a conditioned moment closure, and Merci et al. [23],

who applied a modified k–ϵ model. Muradoglu et al. [24] used a hybrid PDF model to study the flow and mixing fields. Kuan and Lindstedt [20] applied unsteady RANS simulations with second moment closures for the velocity and scalar fields to obtain a (partial) resolution of coherent structures. In a further step, the unsteady RANS simulations were combined with a transported PDF method and closed at the joint scalar level and accurate predictions of the flow and species concentration were reported [25,26]. Other contributions to the workshop on turbulent nonpremixed flames (TNF) [19–21] emphasize the importance and challenging character of these bluff-body stabilized flames. The present work is thus focused on the fluid mechanics of the burner, the near-field impact of boundary conditions, and on requirements in terms of the sampling period and the spatial resolution. The thermochemistry is closed through the use of the steady-state laminar flamelet approximation with libraries determined through the use of comprehensive detailed chemistry [27,28].

2. The current large-eddy simulation approach

To compute the temporal development of large-scale features, the modeled transport equations for the filtered density $\bar{\rho}$, velocity $\widetilde{u_i}$, and mixture fraction $\tilde{f}$ are solved:

$$\frac{\partial \bar{\varrho}}{\partial t} + \frac{\partial}{\partial x_j}\left(\bar{\varrho}\widetilde{u_j}\right) = 0, \tag{1}$$

$$\begin{aligned}
\frac{\partial}{\partial t}\left(\bar{\varrho}\widetilde{u_i}\right) &+ \frac{\partial}{\partial x_j}\left(\bar{\varrho}\widetilde{u_i}\widetilde{u_j}\right) \\
&= \frac{\partial}{\partial x_j}\left[\bar{\varrho}(\nu_t + \nu)\left(\frac{\partial \widetilde{u_j}}{\partial x_i} + \frac{\partial \widetilde{u_i}}{\partial x_j}\right)\right. \\
&\quad \left. - \frac{2}{3}\bar{\varrho}(\nu_t + \nu)\frac{\partial \widetilde{u_k}}{\partial x_k}\delta_{ij}\right] \\
&\quad + \frac{1}{3}\frac{\partial}{\partial x_i}\bar{\varrho}\tau_{kk}^{sgs} - \frac{\partial \bar{p}}{\partial x_i} + \bar{\varrho}g_i, \tag{2}
\end{aligned}$$

$$\begin{aligned}
\frac{\partial}{\partial t}\left(\bar{\varrho}\tilde{f}\right) &+ \frac{\partial}{\partial x_j}\left(\bar{\varrho}\tilde{f}\widetilde{u_j}\right) \\
&= \frac{\partial}{\partial x_j}\left(\bar{\varrho}\left(\frac{\nu_t}{\sigma_t} + \frac{\tilde{\nu}}{\sigma}\right)\frac{\partial \tilde{f}}{\partial x_j}\right). \tag{3}
\end{aligned}$$

In the above equations, u_i is the velocity component in the x_i direction, ρ the fluid density, ν viscosity, and f the mixture fraction. Pressure and gravitational acceleration are given by p and g_i, while σ refers to the laminar Schmidt number. The definition of the mixture fraction f is discussed below. The continuity equation (1) is identical to the unfiltered equation, while the modeled transport equations (2) for momentum (Navier–Stokes equations) feature unclosed terms. The subgrid contribution to the momentum

flux is included via the eddy viscosity ν_t and the trace of the subgrid stress tensor τ_{kk}^{sgs}. In Eq. (3) for the filtered mixture fraction $\tilde{f}$, the subgrid contribution to the fluxes is modeled via the eddy diffusivity (ν_t/σ_t), which is computed from the turbulent Schmidt number ($\sigma_t = 0.4$) [10]. The turbulent viscosity ν_t is computed using the model of Smagorinsky [29] with the model parameter C_s obtained through the dynamic procedure of Germano et al. [30],

$$\nu_t = (C_s \Delta)^2 \left| \frac{1}{2}\left(\frac{\partial \tilde{u}_j}{\partial x_i} + \frac{\partial \tilde{u}_i}{\partial x_j} \right) \right|. \tag{4}$$

The filter width is denoted by Δ and the trace of the subgrid stress tensor τ_{kk}^{sgs} can be removed from (2) by introducing the pressure parameter $\bar{P} = \bar{p} - 1/3\bar{\varrho}\tau_{kk}^{\text{sgs}}$, which is determined from the pressure correction algorithm.

The derivation of the filtered transport equations features the application of a low-pass filter h to all the terms of the corresponding unfiltered equations. For example, the convolution of the mixture fraction field $f(x_j, t)$ with the filter function $h(x_j - x_j')$ yields the filtered field $\overline{f(x_j, t)}$,

$$\overline{f(x_j, t)} = \iiint\limits_{-\infty}^{\infty} f(x_j - x_j')h(x_j') \, dx_1' \, dx_2' \, dx_3'. \tag{5}$$

The difference between the filtered field $\overline{f(x_j, t)}$ and the original field $f(x_j, t)$ is typically called the "fine structure" $f'(x_j, t)$ of $f(x_j, t)$,

$$f(x_j, t) = \overline{f(x_j, t)} + f'(x_j, t). \tag{6}$$

In the present work, a top-hat filter, based on a computational grid cell of volume ΔV, is applied with $h_S = 1/\Delta V$ inside the cell and $h_S = 0$ otherwise. The approach corresponds to a Schumann filter [31], which is applied implicitly with finite-volume approaches by approximating the values at the center with the mean over the entire cell. The filter width Δ is thus defined as a characteristic length of the cell.

2.1. Modeling of combustion

The thermochemistry is here closed through a steady-state flamelet approach featuring comprehensive chemistry with 97 species and 629 chemical reactions [27,28]. Computations were performed with differential and equal diffusivity approximations and, following a preliminary analysis, the latter library was selected. The rates of strain included were $a = 50$, 100, 200, 400, 800, and 1200 s^{-1} and the computed extinction point was $a_q \sim 1300$ s^{-1}. For each strain rate, the scalar dissipation rate is a function of the mixture fraction. In the LES, the mixture fraction and the scalar dissipation rate are used to determine the corresponding rate of strain and thus the appropriate entry of the flamelet table. Fig. 1 shows the effect of strain on the flamelet solutions for the temperature and the mass fraction of hydroxyl (OH) as a function of the mixture fraction. The plot shows the table that was created for the LES by coarsening the flamelet solution to 200 equidistant points.

Bilger's definition [32] of the mixture fraction, which is based on the elemental mass fractions z_β, is applied in the current work:

$$f = \frac{\frac{z_C}{mW_C} + \frac{z_H}{nW_H} + 2\frac{x_{O_2,2} - z_O}{\nu_{O_2}' W_{O_2}}}{\frac{z_{C,1}}{mW_C} + \frac{z_{H,1}}{nW_H} + 2\frac{x_{O_2,2}}{\nu_{O_2}' W_{O_2}}}. \tag{7}$$

The molecular weight of atom β is denoted as W_β and the stoichiometric coefficients and the number of carbon (m) and hydrogen (n) atoms are determined from the corresponding global reaction step.

The species mass-fractions x_α are computed with a steady flamelet relation [4], given for unity Lewis numbers (8), where S_{x_α} denotes the chemical source terms:

$$-\varrho \frac{\chi}{2} \frac{\partial^2 x_\alpha}{\partial f^2} = S_{x_\alpha}. \tag{8}$$

The rate of scalar dissipation χ is a function of the coefficient of diffusion (ν/σ) and the mixture fraction field:

$$\chi = 2\frac{\nu}{\sigma}\left(\frac{\partial f}{\partial x_j} \frac{\partial f}{\partial x_j} \right). \tag{9}$$

Equations (8) and (9) yields the species concentrations x_α, as well as temperature, density, and viscosity, which are functions of the mixture fraction f and the scalar rate of dissipation χ only.

In the present context, only the filtered fields $\tilde{f}$ and $\tilde{\chi}$ are known. Since any dependent quantity is a nonlinear function of f and χ, the subgrid distribution must also be determined (as $\widetilde{\Phi}(f, \chi) \neq \Phi(\tilde{f}, \tilde{\chi})$). The distribution of the mixture fraction is here described by a presumed β-PDF, which is a function of the filtered mixture fraction $\tilde{f}$ and its subgrid variance $\widetilde{f''^2}$. The subgrid contribution to the scalar dissipation (which itself is typically assumed to be lognormal) is simply described by a Dirac δ-function, as recent work suggests that further investigations are required [33–35]. All dependent scalars $\widetilde{\Phi}$ can then be readily computed as $\widetilde{\Phi(f, \chi)} = \widetilde{\Phi}(\tilde{f}, \tilde{\chi}, \widetilde{f''^2})$. The function is preintegrated and tabulated with $\widetilde{\Phi}$ determined by linear interpolation between the six support points in the flamelet look-up table. The present table was resolved by (200 × 200) nodes in $(\tilde{f} \times \widetilde{f''^2})$ directions. The subgrid mixture fraction variance $\widetilde{f''^2}$ is modeled using the approach of Forkel [36], which
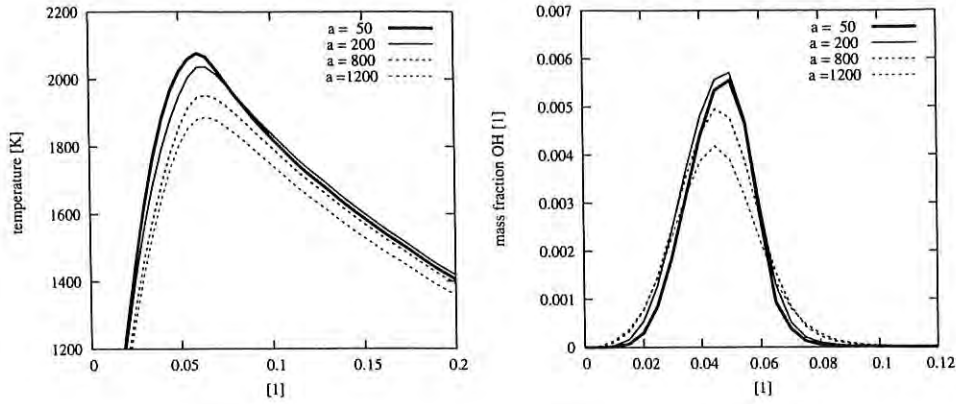
Fig. 1. Effect of the strain rate a on the laminar flamelet. Temperature versus mixture fraction (left) and hydroxyl (OH) mass fraction versus mixture fraction. The plots show the range around the stoichiometric mixture fraction $f = 0.05$ of the equidistant table used in the LES.

is based on the resolved variance obtained using a test-filter cell with a volume twice that of the nominal resolution. The filtered rate of scalar dissipation $\tilde{\chi}$ is modeled using an eddy viscosity approach as suggested by Girimaji and Zhou [37] and de Bruyn Kops et al. [38],

$$\tilde{\chi} = 2\left(\frac{\nu}{\sigma} + \frac{\nu_t}{\sigma_t}\right)\left(\frac{\partial \tilde{f}}{\partial x_j}\frac{\partial \tilde{f}}{\partial x_j}\right). \tag{10}$$

2.2. The numerical technique

The conservation equations for mass $\bar{\varrho}$ (1), momentum $\overline{\varrho u_i}$ (2), and the mixture fraction $\overline{\varrho f}$ (3) were transformed to cylindrical coordinates (x, r, ϕ) and discretized using a finite-volume technique [8] on a staggered grid. The time integration uses an explicit three-step low-storage Runge–Kutta scheme, which is third-order accurate for linear problems. For the scalars $\bar{\varrho}, \overline{\varrho f}$, each substep features a predictor/corrector approach to deal with nonlinear dependencies $\bar{\varrho}^{m+1} = \bar{\varrho}(\tilde{f}^{m+1}, \tilde{\chi}^{m+1}, \widetilde{f''2}^{m+1})$.

In the predictor step, $\bar{\varrho}^m$ and $\overline{\varrho f}^m$ are transported, leading to the prediction $\bar{\varrho}^{m+1*}$ and $\overline{\varrho f}^{m+1*}$, which results in the new mixture fraction field $\tilde{f}^{m+1} = \overline{\varrho f}^{m+1*}/\bar{\varrho}^{m+1*}$. For the latter, the chemistry table yields the corresponding "correct" density $\bar{\varrho}_c^{m+1}$, which is not necessarily identical to $\bar{\varrho}^{m+1*}$. The difference between these densities $\bar{\varrho}^{m+1*}$ and $\bar{\varrho}_c^{m+1}$ must then be eliminated by the pressure-correction scheme. This projection method adjusts the velocities in such a way that transport of $\bar{\varrho}^m$ would yield $\bar{\varrho}^{m+1} = \bar{\varrho}_c^{m+1}$ instead of $\bar{\varrho}^{m+1*}$.

In the subsequent correction step, $\bar{\varrho}^m$ and $\overline{\varrho f}^m$ are transported again, this time with the corrected velocities, which results in the solution $\bar{\varrho}^{m+1}$ and $\overline{\varrho f}^{m+1}$ for the new time step. With the present scheme, changes in $\bar{\rho}$ and $\overline{\rho f}$ are due only to fluxes over the cell boundaries, so the scheme can be implemented in a fully conservative way. Hence, the approach was named echt konservativer transport (EKT) [39].

With TVD schemes, the interpolation for Φ_f on the center of the cell face is based on the upwind values Φ_U, Φ_C and the downwind value Φ_D. The flux-limiter function $B(r)$ depends on the gradient ratio r:

$$\Phi_f = \Phi_C + \frac{B(r)(\Phi_C - \Phi_U)}{2}$$

$$\text{with } r = \frac{\Phi_D - \Phi_C}{\Phi_C - \Phi_U}. \tag{11}$$

The properties of the convection scheme are determined by $B(r)$ and here a smooth nonlinear limiter function, CHARM, has been applied [40]:

$$B(r) = \begin{cases} \frac{r(3r+1)}{(r+1)^2}, & r > 0, \\ 0, & r \leqslant 0. \end{cases} \tag{12}$$

The present TVD-schemes are second-order accurate away from sharp gradients. In contrast to momentum transport, central schemes are not suited to the transport of scalar fields, which do not benefit from the smoothing property of the pressure correction. However, in the present algorithm, TVD schemes are not applied for momentum and will thus hardly affect the predictions of the flow field.

3. The Sydney bluff-body burner

The Sydney burner consists of a cylindrical bluff-body with diameter $D = 50$ mm, which is located in a coaxial flow. On the centerline, a nozzle of diameter $d = 3.6$ mm ejects fuel into the recirculation zone. The geometry is shown in Fig. 2 along with superimposed mean streamlines. The fuel jet creates its own (inner) embedded recirculation zone. The flow
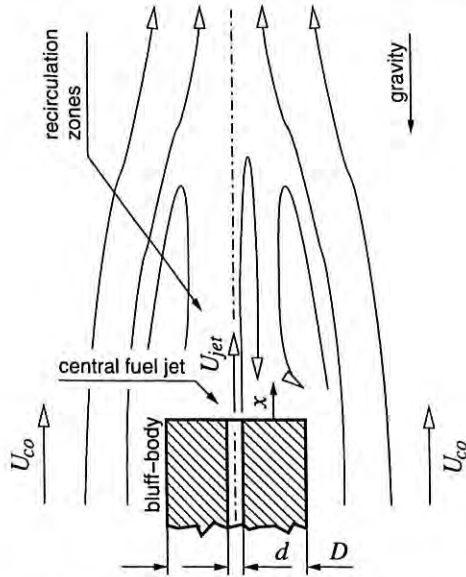
Fig. 2. Configuration of the cylindrical bluff-body burner. Fuel is injected into the recirculation zone from the coaxial pipe.

Table 1
Cases investigated in the present work

Name	U_{jet} (m/s)	$U_{co.}$ (m/s)	Velocity data	Scalar data	This work
NRBB	61	20	LDV	–	LES
HM1e	108	35	LDV	–	LES
HM1	118	40	–	R/R/LIF	LES

field features strong turbulence and intense mixing of reactants and combustion products. The fuel is a mixture of 50% hydrogen and 50% methane (by volume), resulting in a stoichiometric mixture-fraction of 0.05. The burner was first examined by Dally et al. [17,18] and subsequently by Kalt and Masri [22]. The velocity data were obtained by LDV (laser Doppler velocimetry) at the University of Sydney and the scalar fields were measured by single-point Raman–Rayleigh LIF (laser induced fluorescence) at Sandia National Laboratories. A total of five sets of conditions were investigated experimentally and the current work considers the first three (NRBB, HM1e, and HM1), as shown in Table 1.

Computational domain and boundary conditions

The experimental configuration was discretized using a cylindrical computational domain of diameter $8.8D$ and length $3D$ for the isothermal case. For the reactive case, immersed boundary conditions have been used and the domain size was increased to a length of $5D$. The domain was resolved by n_x axial, and the radius by n_r radial cells (see Table 2). The radius of the jet and of the bluff body were discretized by $n_{r,j}$ and $n_{r,b.}$ nodes, respectively. In the circumferential direction, n_ϕ cells were used. On the *fine* grid, this leads to a total of $n = 3,643,200$ cells. The temporal development was then studied for n_t time-steps.

At the inflow plane of the domain, the velocities were set by a transient Dirichlet condition and on the lateral boundary a simplified momentum equation

was solved to allow for entrainment. At the outflow plane, the velocity gradients were set to zero using a Neumann condition. The mixture fraction is given by a Dirichlet condition at the inflow and a Neumann condition on the lateral boundary and on the outflow surfaces. The ambient pressure was set on the shell of the domain, and for the inflow/outflow the pressure was specified by Neumann conditions. Neumann conditions do affect eddies that leave the computational domain. To reduce the influence of the boundaries, the computational domain was chosen to be significantly larger than the area of interest.

The turbulence and the dissipation rate entering the computational domain were set by specifying the Reynolds stress tensor $R_{ij}(x_0, r, \phi)$ and an integral length scale $L(x_0, r, \phi)$ at the inflow plane using the approach developed by Klein et al. [41] and enhanced by Kempf et al. [42]. This method features random inflow velocities that satisfy the prescribed mean velocities u_i, the Reynolds stress tensor R_{ij}, the length scale L, and a turbulent energy spectrum.[1] In the absence of experimental data, the length scales in the jet and in the co-flow were set to $L = \min(0.4\Delta y, L_{max})$, i.e., scaled with the distance Δy to the closest wall, but limited to L_{max}. Given the geometry of the bluff-body burner, $L_{max} = 3$ mm appears to be a reasonable physical limit. The Reynolds stress tensor R_{ij} in the central jet was set according to the data of Lawn [43], and for the co-flow based on the experiments presented at the TNF workshops [20,22]. To assess the quality of the results, a number of simulations were performed on different grids as outlined in Table 2.

The inflow boundary conditions and the grid-resolution were found to be crucial in determining the flow characteristics. In preliminary simulations, strong vortex-shedding was observed at the edge of the bluff body. The experimental data suggest that such structures do not occur to same extent. A significant sensitivity was observed with respect to numerical diffusion and the inflow-boundary conditions. Numerical diffusion of the mixture fraction leads to

---

[1] The spectrum for the inflow velocity can only comprise the large-scale structures and thus neglects the subgrid fluctuation.
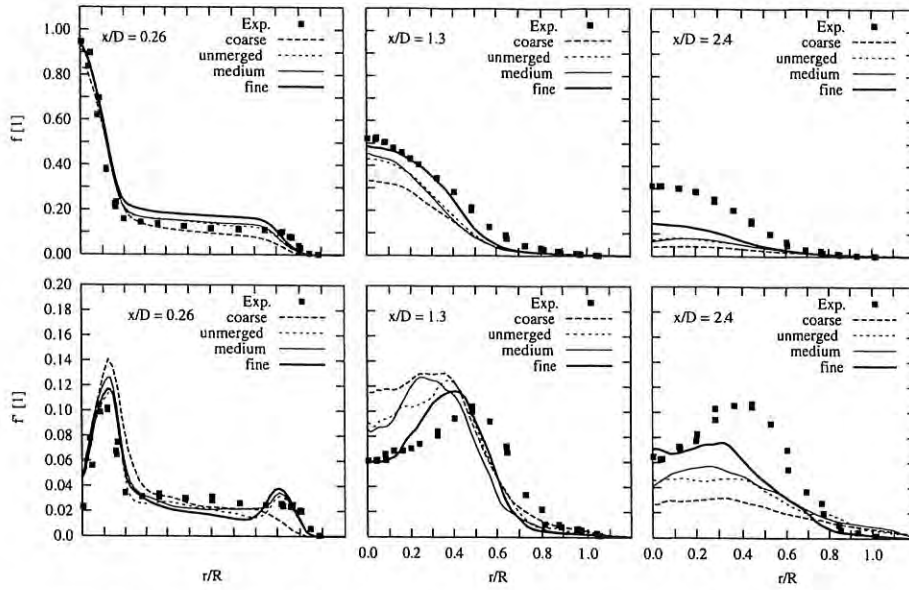
$\overline{z}$

$\overline{z'^2}$

Fig. 11. Comparison of results obtained on different grids for flame HM1e: *coarse* (0.45×10^6 nodes), *medium* (1.8×10^6), *unmerged* (like *medium* but without merging at centerline), and *fine* (3.6×10^6). Mixture-fraction mean (top) and mixture-fraction fluctuation (bottom) are plotted versus the radius r/R ($R = 25$ mm) at various axial positions x/D ($D = 50$ mm).
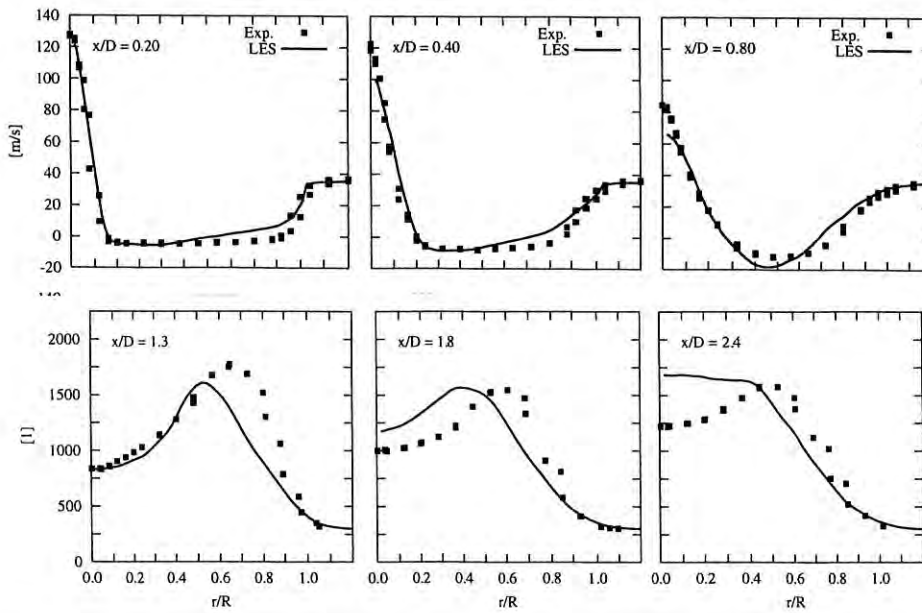
$\overline{u}$

T

Fig. 19. Mean temperature versus the normalized radius r/R ($R = 25$ mm) at different axial positions x/D ($D = 50$ mm) $/D$
e---- IM1 , ... campaigns.
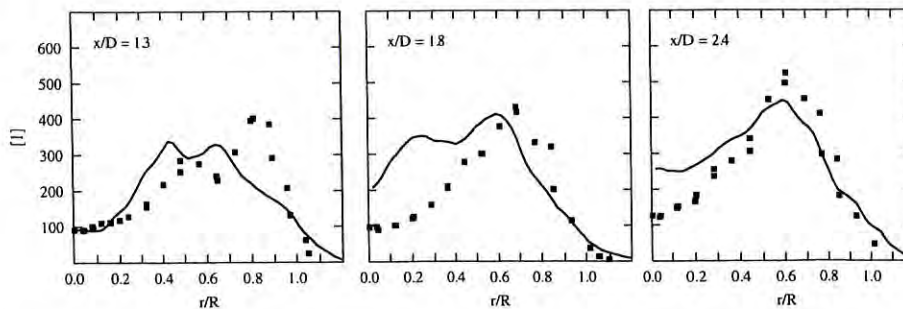
Fig. 20. Fluctuation of the temperature versus the normalized radius r/R ($R = 25$ mm) at different axial positions x/D ($D = 50$ mm) for flame HM1.

4-36

NOₓ post processing in FLUENT

$$O + N_2 \xrightarrow{k_1} NO + N$$

$$N + O_2 \xrightarrow{k_2} NO + O$$
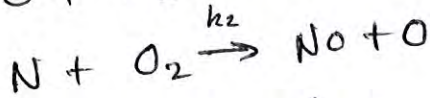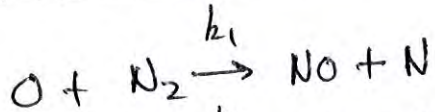
Zeldovich mechanism

$$\frac{d C_{NO}}{dt} = k_1 C_O C_{N_2} + k_2 C_N C_{O_2}$$

$$\frac{d C_N}{dt} = + k_1 C_O C_N - k_2 C_N C_{O_2} = 0 \quad \text{steady state assumption for N}$$

(a) $\dfrac{d C_{NO}}{dt} = 2 k_1 C_O C_{N_2}$

(b) $C_O = C_{O_2}^{1/2} \cdot K_P^{1/2} (R_u T)^{-1/2}$

$$O \rightleftharpoons \tfrac{1}{2} O_2 \quad \text{partial equil.}$$

(e) $W_{NO} = \dfrac{kg \; NO/sec}{vol} = \underbrace{MW_{NO}}_{30} \dfrac{d C_{NO}}{dt}$

(c) $C_{O_2} = X_{O_2} \dfrac{P}{R_u T}$

(d) $C_{N_2} = X_{N_2} \dfrac{P}{R_u T}$

combine a-e: at each point:

$$W_{NO} = \left[MW_{NO} \; 2 k_1 \; K_P^{1/2} (R_u T)^{-1/2} \left(\frac{P}{R_u T}\right)^{3/2} \right] X_{O_2}^{1/2} \; X_{N_2}$$

fcn of T, P

true at each instant of time, at each (x,r) location

we know:
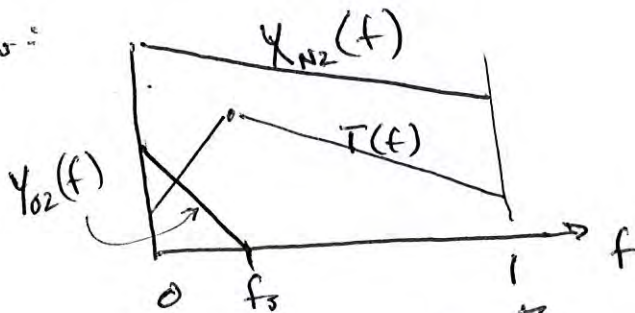
no O_2 for rich conditions

state relation for instantaneous conditions

4-37
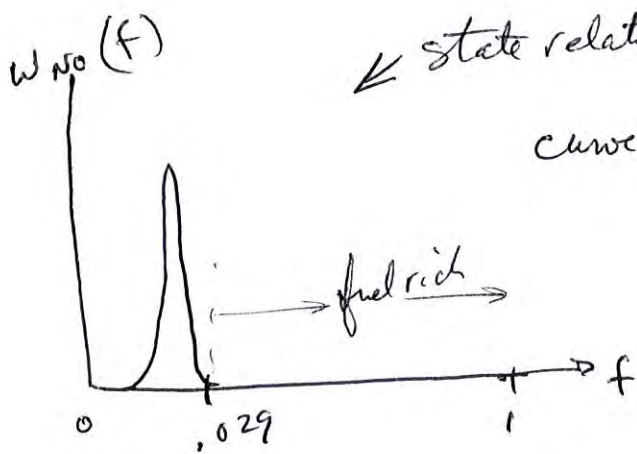
$W_{NO}(f)$

← state relation for $W_{NO}(f)$

curve is zero for $f > f_s$ fuel rich, no O_2

max on lean side of stoich

fuel rich →

0   .029   1   → f

instantaneous state relation

$$\overline{W_{NO}} = \int_0^1 W_{NO}(f) \, P(f) \, df$$

prob. of lean but hot! causes NO to form

pure air

pure fuel

0   stoich   1 f
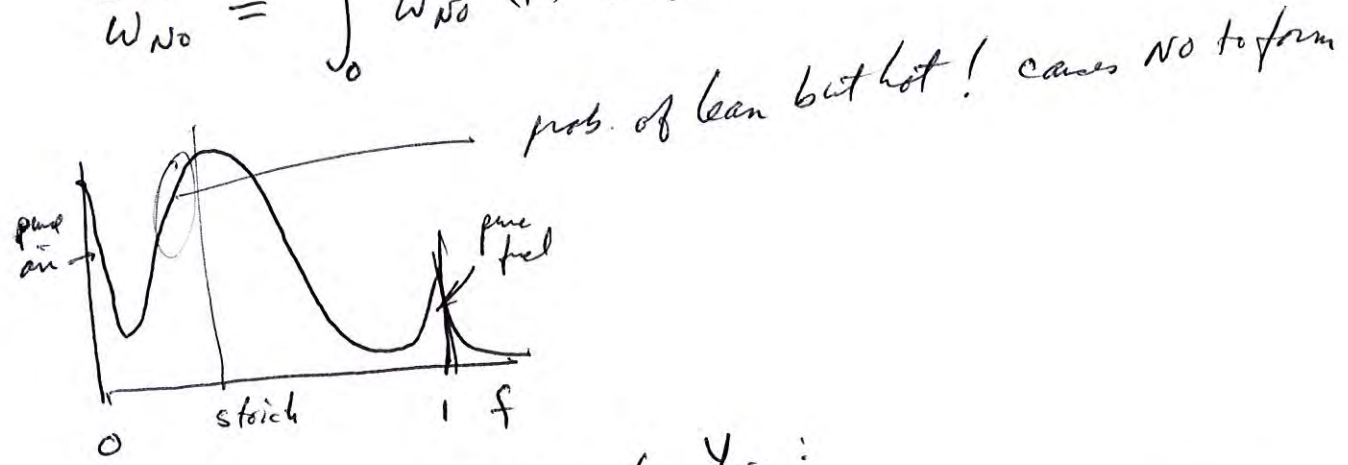
now plug into conservation eqn for Y_{NO}:

$$\overline{\rho} \, \tilde{u}_x \frac{\partial \overline{Y_{NO}}}{\partial x} + \overline{\rho} \, \tilde{u}_r \frac{\partial \overline{Y_{NO}}}{\partial y} = \frac{1}{r} \frac{\partial}{\partial r}\left(\frac{\mu_T}{\sigma_{NO}} r \frac{\partial Y_{NO}}{\partial r}\right) + \overline{\dot{w}_{NO}}$$

$$\mu_T = C_D \, \rho \, k^2/\epsilon \qquad \sigma_{NO} \approx 1$$

NO produced only in high T lean zone $T > 1800K$ $f < f_s$

high T lean zone   high T rich zone

mean stoich. contour — highest T

4-38
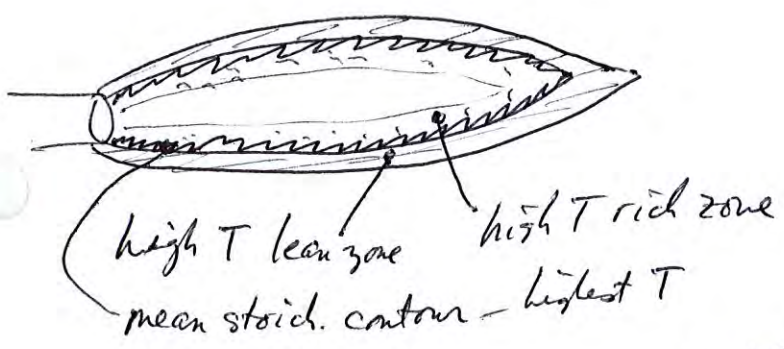
Note PDF method is needed for NO, also CO

fuel rich, on average   A   at this pt fuel-rich on average $\overline{Y}_{O_2} = 0$
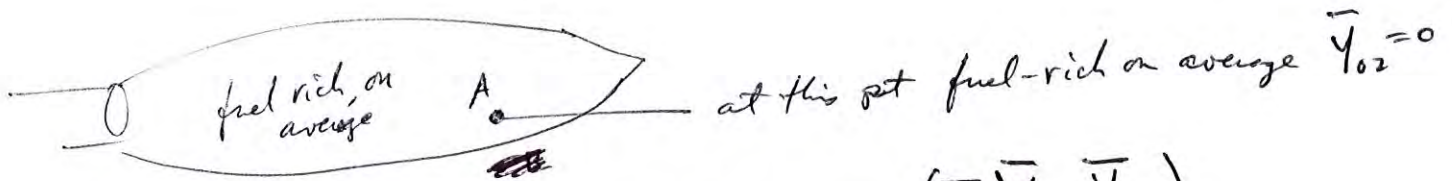
at A: wrong way: $\overline{W}_{NO}(A) = W_{NO}(\overline{T}, \overline{Y}_{O_2}, \overline{Y}_{N_2})$

say $\overline{W}_{NO}(A) = 0$

right way $\overline{W}_{NO} = \int W_{NO}(T, \cancel{Y_{O_2}}, \cancel{Y_{N_2}}) P(f) df$

at A there is some prob. that lean + hot conditions occur — say 20% of time ← maybe larger if highly turbulent

A will contribute to W_{NO}

very small turbulence level ⟹ wrong way almost correct
large turb. level ⟹ wrong way very wrong!

- recirc. zones
- strong shear layers large (Δu)
- supersonic

4-39

but NO is convected downstream
diffuses in both directions ($\pm$ r)
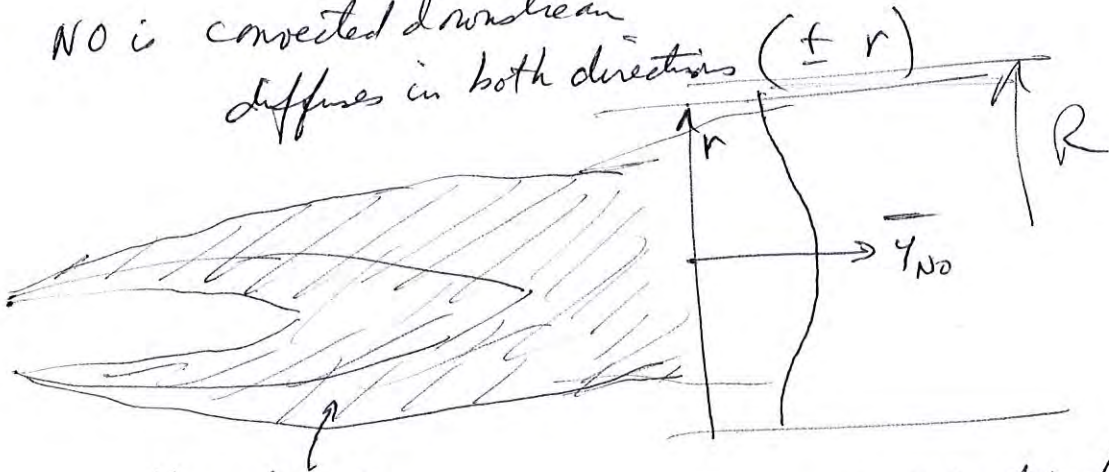
Y_{NO} largest

NO is not destroyed so it diffuses + convects to fill entire tube
downstream!

$EINO = $ NO emission index $= \dfrac{g \ NO \ in \ exhaust/sec}{kg \ fuel \ consumed/sec} \approx 10 \ \dfrac{g \ NO}{kg \ fuel}$

$g \ NO \ in \ exhaust/sec = \left. \displaystyle\int_{r=0}^{R} \rho \cdot U \ \overline{Y}_{NO}(r) \ 2\pi r \, dr \right]_{x=large}$

$\longleftarrow$ compute $\overline{Y}_{NO}(x,r)$ by solving cons. eqn for $\overline{Y}_{NO}$,

$kg \ fuel \ consumed = \rho_F \ U_F \left(\dfrac{\pi d_F^2}{4} \right)$

Summary of FLUENT

solve MIXture fraction f eqn (called $\bar{z}$ n $\bar{z}$) two scalars $(\bar{f}, g, \bar{\chi}_s)$ deleterious

APM = assumed pdf method, scalars $\bar{Y}_{H_2}$ $\bar{Y}_{CO}$ $\bar{Y}_{H_2O}$ etc

lookup tables

nonpremixed, flamelet regime

set of eqns   convection / diffusion / source terms

$\tilde{u}, \tilde{v}, \tilde{w}, \bar{f}, g, k, \epsilon$ ($\overline{u'v'}$, RSM)   gradient diffusion or RSM

for Reynolds stress

Complex chemistry + heat release are in the state relations =

solutions to steady flamelet eqn

many assumptions: $\mu_T = C_\mu \bar{\rho} \, k^2/\epsilon$, $\sigma_{f} = 0$, Beta PDF

due NOx, CO postprocessing — slow distributed reactions

— ignored preferential diffusion   assume all D_i's $\approx$ same

— assumes PDF shape is β-function

— assumes ϵ eqn ok — b.c. on ϵ?

— assumes flamelet regime — analogy

NOx model
added to RANS of a
furnace geometry

Prediction of a Turbulent Non-Premixed Natural Gas Flame in a Semi-Industrial Scale Furnace using a Radiative Flamelet Combustion Model

T. Mahmud · S. K. Sangha

Abstract A mixedness-reactedness flamelet combustion model coupled with a comprehensive radiation heat transfer model based on the discrete transfer method of solution of the radiative transport equation is applied for the simulation of a 3 MW non-swirling turbulent non-premixed natural gas flame in the experimental furnace at the International Flame Research Foundation. In the calculation, turbulence is represented by the standard $k - \varepsilon$ and a differential Reynolds-stress model. Predictions are compared with measurements of mean gas velocity, temperature, major species concentrations and incident radiation wall flux. The radiative mixedness-reactedness flamelet combustion model, irrespective of the model for turbulence, is able to reproduce the basic structure of the experimental flame, which is stabilised downstream of the burner nozzle. In the near burner region, encompassing the non-reacting lift-off zone, good quality predictions are obtained using both the turbulence models, whereas further downstream, within the combusting zone of the jet, the Reynolds-stress turbulence model generates better predictions at and about the furnace axis. The nitric oxide (NO) formation via the thermal- and prompt-NO routes was also calculated and compared with in-flame and flue-gas NO data. The measured NO level at the furnace exit is well reproduced in the calculation, however discrepancies exist near the burner where NO concentrations around the furnace axis are overpredicted.

T. Mahmud (✉) · S. K. Sangha
School of Process, Environmental and Materials Engineering,
The University of Leeds, Leeds LS2 9JT, UK
e-mail: T.Mahmud@leeds.ac.uk

Springer

methane flame considered here are the thermal-NO, which involves the oxidation of atmospheric nitrogen in high temperature regions, and the prompt-NO, which accounts for the reactions between hydrocarbon free radicals such as CH and molecular nitrogen under fuel-rich conditions producing atomic nitrogen, hydrogen cyanide (HCN) and amines (NH), which are subsequently converted to NO. The NO formation is modelled outside the flamelet structures. The formation of thermal-NO is modelled via the well-known Zeldovich mechanism [38] with the inclusion of the reverse reactions. The oxygen atom (O) concentration needed to determine the rate of formation is calculated by assuming partial equilibrium between O and O_2. The rate constants are taken from Baulch et al. [57]. For the prompt mechanism, a global rate expression proposed by De Soete [39] for the combustion of hydrocarbon fuels is used. As an alternative approach, the O concentration needed in the calculation of thermal-NO could have been obtained from the flamelet data instead of assuming partial equilibrium between O and O_2, and the prompt-NO modelled within the flamelet structures using a detailed reaction mechanism. However, previous studies [e.g., 58, 59] using a flamelet based thermal-NO modelling approach have revealed discrepancies between the predicted and experimental NO data even with the inclusion of the radiation and differential diffusion effects. It has been suggested [59] that this discrepancy can be attributed to inadequate treatment of the turbulence–chemistry interaction. The objective here is to examine how the thermal-NO model based on partial equilibrium between O and O_2 and the prompt-NO model with a global rate expression, which are widely used together with equilibrium combustion models for the prediction of NO emissions from practical flames, perform in conjunction with an advanced turbulent combustion model.

A Favre-averaged conservation equation is solved in order to obtain NO concentration, $\tilde{m}_{NO}$, distributions,

$$
\frac{\partial}{\partial x_j}\left(\bar{\rho}\tilde{u}_j\tilde{m}_{NO}\right) = -\frac{\partial}{\partial x_j}\left(\frac{\mu_t}{Sc_t}\frac{\partial\tilde{m}_{NO}}{\partial x_j}\right) + \bar{w}_{NO}
\tag{13}
$$

where the source term, $\bar{w}_{NO}$, represents the mean rate of formation of NO via the thermal and prompt mechanisms. The mean reaction rates are obtained, taking into account the effect of temperature fluctuations, using a beta-function PDF. A post-processing approach has been employed in order to solve (13) using the predicted velocity, temperature and major species concentration fields obtained from the thermo-fluids and combustion models.

2.5 Method of solution

The Favre-averaged conservation equations, written in cylindrical coordinates, were discretised by integrating over control volumes covering one-half plane of the computational domain. The convection terms were approximated by a third-order accurate, non-diffusive, boundedness-preserving discretisation scheme [60], while the diffusion terms were approximated using central differencing. The discretised equations were solved by a variant [60] of the SIMPLE algorithm [61] using the 'penta-diagonal-matrix-algorithm'.

## 3 Application of the Model

3.1 The experimental case

A 3 MW semi-industrial scale natural gas flame in the IFRF furnace no. 1 was simulated in this study. This flame is referred to as Flame-29 of M-2 trials at IFRF [37]. It is worth noting that there is a dearth of comprehensive data sets for large-scale flames in geometries relevant to practical combustors suitable for validation of mathematical models for gaseous fuel combustion. The IFRF experimental case, which includes flow, temperature, species concentrations and radiative heat transfer data, serves this purpose well. Flame-29 is a non-swirling, turbulent non-premixed jet flame produced by a double-concentric cylindrical burner without a bluff body. The fuel was natural gas (81.3% methane, 4.3% higher hydrocarbons and 14.4% nitrogen by volume) and was introduced through the central nozzle and the combustion air together with extra oxygen through the annulus. The operating conditions of the burner are given in Table 1. In the experiment, a long non-luminous jet flame, stabilised at the burner exit, was produced. The combustion air was enriched with oxygen to 25% (by volume) in order to stabilise the flame. The flame did not contain any measurable amount of soot and burned as a blue flame. The combustion chamber of the IFRF furnace no. 1 is square in cross-section and the length and width of the chamber are 6.25 and 2.0 m, respectively. The furnace walls were refractory lined with cooling loops installed for heat extraction. The furnace is illustrated schematically in Fig. 1.

Detailed measurements of velocity, gas temperature, major species and NO concentrations were carried out along the width of the furnace at a number of axial stations and radiative heat fluxes were measured along the furnace wall. The mean axial velocities were measured using a five-hole hemispherical and Prandtl probe with uncooled tips. Details of the probes may be found in [37, 62]. Measurement errors are to be expected for these types of pressure probes due to flow perturbation caused by probe interference, and the high levels of turbulence and strong shear in some regions of the flow. Although it is difficult to quantify such errors, previous analyses [63] indicate that the perturbation in mean velocity is typically less than 10%, the axial velocity can be about 10% high in the region of maximum shear and good measurement accuracy can be achieved even in flows with high turbulence intensities. Mean gas temperatures were measured using a conventional suction pyrometer with a triple refractory shield surrounding a thermocouple. It was reported [37] that the measurement error, other than that due to the thermocouple itself, was less than 8°C. Species concentrations were obtained by collecting gas samples from the furnace with a water-quenched miniature probe and analysing them using a gas chromatograph. The uncertainty in the concentration measurements was not

Table 1 The burner input conditions		
Fuel flow rate		280 kg/h
Fuel inlet velocity		112 m/s
Fuel temperature		283 K
Air flow rate		3,126 kg/h
Excess oxygen flow rate		170 kg/h
Air/oxygen inlet velocity		36 m/s
Air temperature		299 K

4-95

Fig. 8 Comparison between
the predicted and measured
[37] radial profiles
of NO concentration
(△ measurements, *solid line*
RST and RMR flamelet
model)
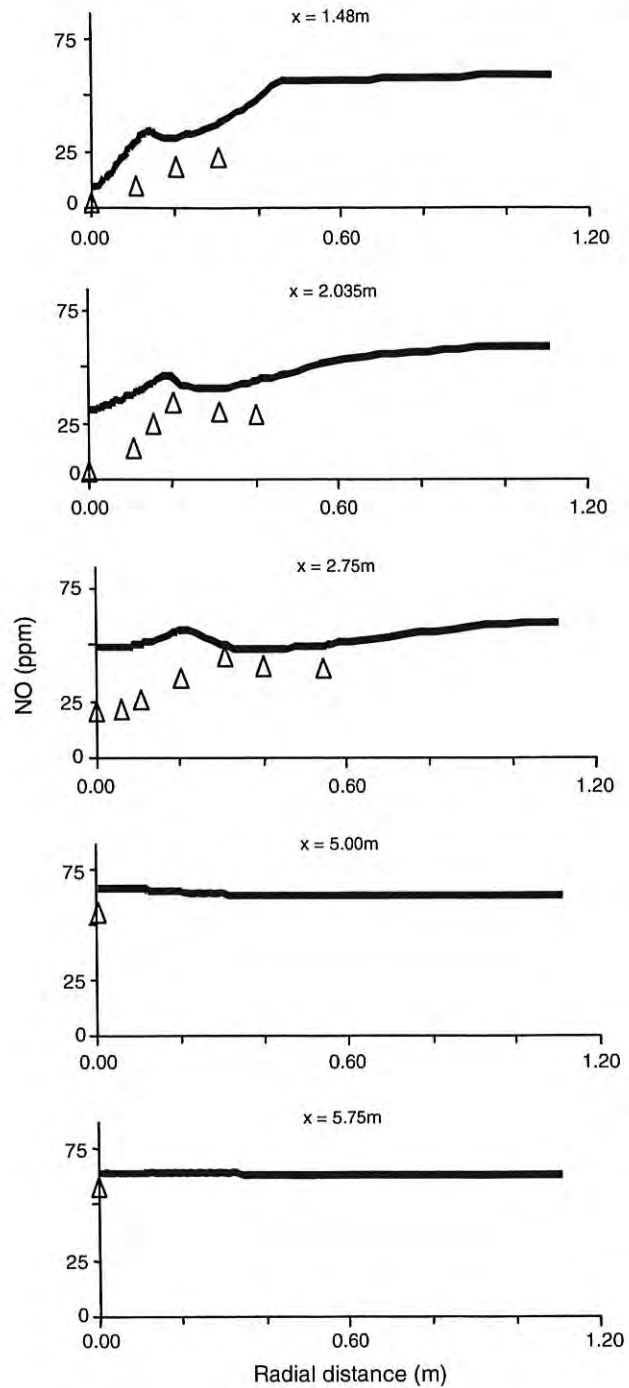
Modeling of radiation and nitric oxide formation in turbulent nonpremixed flames using a flamelet/progress variable formulation

Matthias Ihme[a)] and Heinz Pitsch

Department of Mechanical Engineering, Building 500, Stanford University, Stanford, California 94305, USA

A model for the prediction of the nitric oxide (NO) formation in turbulent nonpremixed flames is proposed. Since the NO formation has a strong temperature sensitivity, the accurate prediction of the flame temperature under the consideration of radiative heat losses is required. The first part of the paper addresses the extension of a flamelet-based combustion model to account for radiative heat loss effects by introducing enthalpy as an additional parameter. A transport equation for enthalpy is solved, and the radiative sink term in this equation is obtained from unsteady flamelet solutions. The model is applied to a large-eddy simulation (LES) of Sandia flame D and the importance of the interaction between turbulence and radiation on temperature and mixture fraction is investigated. Based on the radiative flamelet formulation, a consistent model for the prediction of NO formation is developed in the second part of the paper. In this model, an additional transport equation for the NO mass fraction is solved, and the chemical source term is obtained from a flamelet library. Since the consumption rate is dependent on the NO mass fraction, this term requires modeling, which is discussed in this paper. By employing a scale similarity argument, a closure model for application in LES is presented. After the analysis of the proposed model for the thermal, nitrous oxide, and prompt pathways for NO formation, the NO model is integrated into the extended flamelet/progress variable model and applied in LES of Sandia flame D and a Pratt & Whitney aircraft engine combustor configuration. © *2008 American Institute of Physics.* [DOI: 10.1063/1.2911047]

I. INTRODUCTION

The emission of carbon dioxide (CO_2) and pollutants, such as unburned hydrocarbons (UHCs), carbon monoxide (CO), and oxides of nitrogen (NO_x), from combustion processes has gained increasing attention over the past few decades. While CO_2 is considered to be a major greenhouse gas, NO_x is regarded as precursor of chemical smog and as contributor to stratospheric ozone depletion.[1] Devising technologies which reduce emissions of such critical species into the atmosphere requires the understanding and control of their formation mechanisms.

Nitric oxide (NO) and nitrogen dioxide (NO_2), collectively referred to as NO_x, are typically formed on time scales which are slow compared to fuel oxidation reactions. This slow formation process, together with the short residence times in modern combustion devices, implies that NO_x is usually emitted at concentrations substantially below equilibrium values.[2] The slow formation and its strong dependence on the flame temperature represent major difficulties for the accurate prediction of NO_x. An example of the strong temperature dependence is shown in Fig. 1. The left panel of this figure shows the steady-state NO mole fraction $X_{NO,st}$, as a function of the scalar dissipation rate at stoichiometric mixture fraction $\chi_{Z,st}$ for a methane/air flame at standard condition. $X_{NO,st}$ as a function of the corresponding stoichiometric temperature Θ_{st} is shown in the right panel of Fig. 1. This

figure illustrates the temperature sensitivity of NO, suggesting that the accurate modeling of the temperature by accounting for radiation and wall heat losses is of paramount importance for its prediction.

Several models have been proposed for the prediction of nonpremixed turbulent combustion processes in both Reynolds-averaged Navier–Stokes (RANS) simulations and large-eddy simulations (LESs). Among these are the flamelet models,[3,4] the transported probability density function (TPDF) method,[5,6] the conditional moment closure (CMC) method,[7] and the linear eddy model.[8] In many applications of combustion LES, steady laminar flamelet models (SLFMs) have been applied not only in simulations of jet flames[9-11] but also to more complex flows such as gas turbine combustors.[12-14]

The SLFM can be derived from the unsteady flamelet equations, which are obtained through a coordinate transformation of the transport equations for species and temperature by introducing the mixture fraction Z as an independent coordinate.[15] The unsteady flamelet equations can be written as

$$\partial_t \phi - \frac{\chi_Z}{2} \partial_Z^2 \phi = \dot{\omega}, \tag{1}$$

where $\boldsymbol{\omega}$ is the source term of all species and temperature, denoted by $\boldsymbol{\phi}$, and $\chi_Z = 2\alpha|\nabla Z|^2$ is the scalar dissipation rate with α denoting the molecular diffusivity. Note that the source term in the temperature equation also contains terms describing the enthalpy flux by mass diffusion and, possibly, also a radiative source term.

[a)]Present address: Department of Aerospace Engineering, University of Michigan, Ann Arbor, MI 48109. Author to whom correspondence should be addressed. Electronic mail: mihme@umich.edu.
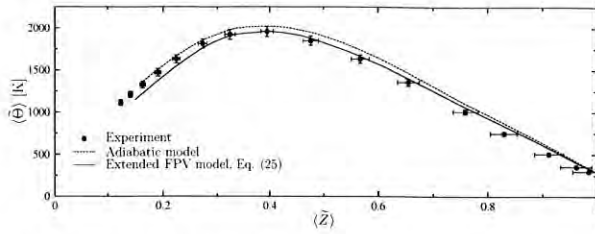
     20, 055110-1

4-47

FIG. 8. Comparison of the predicted mean temperature as a function of $\langle \tilde{Z} \rangle$ along the centerline with experimental data.

mixture fraction in the adiabatic simulation becomes apparent. From this, the pronounced temperature sensitivity on the fuel-lean side is evident, which is approximately a factor of 2 higher than that on the fuel-rich side of the flame.

Figure 8 shows that the mixture fraction-conditioned temperature profile obtained from the radiative simulation is in better agreement with experimental data compared to the adiabatic simulation. It can be seen that radiation is also effective in the fuel-rich part of the flame, which is in agreement with the expectation following the time scale analysis. The temperature on the fuel-lean side is underpredicted. It is important to understand that this region corresponds to the flame location above L_{st} and large residence time. The underprediction of the temperature can be attributed to the known fact that the optically thin radiation model typically overestimates the fraction of radiative heat loss, which has also been observed in calculations using the TPDF method and the CMC model.[29,30,32,33]

III. MODEL FOR THE PREDICTION OF NITRIC OXIDE FORMATION

In this section, a model for the prediction of the nitric oxide formation is developed. The strong temperature sensitivity of the NO formation requires the accurate description of the instantaneous temperature field in a flame under the consideration of radiative heat loss effects, which was addressed in Sec. II B.

In the first part of this section, a model for the NO formation is presented. The performance of the model is then scrutinized in a model analysis for the three relevant NO formation mechanisms, namely, thermal, nitrous oxide, and prompt mechanisms. The individual assumptions of the model are assessed against results obtained from an unsteady flamelet model. Following this model analysis, a closure model for application in LES is developed. This model is then applied in LES of Sandia flame D and a Pratt & Whitney aircraft engine combustor configuration.

A. Model formulation

Similar to the radiation process, NO formation, particularly via the thermal mechanism, occurs on a relatively long time scale τ_{NO} compared to the flamelet lifetime. As an example, the timescale ratio $\mathcal{D}_{NO} = \tau_u / \tau_{NO}$, obtained from a numerical simulation of Sandia flame D, is shown in Fig. 3. A comparison of the chemical time scales of the major species formation to the NO formation indicates that τ_{NO} is typically

more than an order of magnitude larger than τ_C. This observation suggests that NO is not in steady state, and a steady-state assumption will consequently result in considerable overpredictions of NO.

The slow spatial and temporal formation and consumption of NO are described in the present model by the separate solution of a transport equation for the NO mass fraction Y_{NO}. Under the assumption of equal species diffusivities, this equation can be written as

$$\rho \mathcal{D}_t Y_{NO} = \nabla \cdot (\rho \alpha \nabla Y_{NO}) + \rho \dot{\omega}_{NO}. \tag{27}$$

In the following, we will extract the chemical production rate of NO from the extended FPV model, i.e., $\dot{\omega}_{NO} = \mathcal{G}^c_{\dot{\omega}_{NO}}(Z, C, H)$. This, however, requires special attention and is explained by considering the following elementary model reaction:

$$A + B \underset{k_b}{\overset{k_f}{\rightleftharpoons}} NO + D,$$
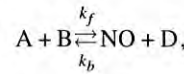
in which species A and B react to form products NO and D. Here, k_f and k_b denote the rate coefficients of the forward and backward reactions, respectively. For this reaction, the chemical reaction rate of NO can be written as

$$\dot{\omega}_{NO} = \dot{\omega}^+_{NO} + \dot{\omega}^-_{NO}, \tag{28}$$

with the production and consumption rates of the forms

$$\dot{\omega}^+_{NO} = \frac{W_{NO}}{\rho^{FPV}} k_f^{FPV} \left(\frac{\rho^{FPV} Y_A^{FPV}}{W_A} \right) \left(\frac{\rho^{FPV} Y_B^{FPV}}{W_B} \right), \tag{29a}$$

$$\dot{\omega}^-_{NO} = - Y_{NO}^{FPV} k_b^{FPV} \left(\frac{\rho^{FPV} Y_D^{FPV}}{W_D} \right). \tag{29b}$$

Since reaction rates will be taken from the flamelet library, all species in Eqs. (29a) and (29b) correspond to the conditions of the flamelet library and are explicitly denoted by the superscript FPV.

In the following, it is assumed that all species except NO are formed on relatively short time scales, and can therefore be represented by the FPV library. Since $\dot{\omega}^-_{NO}$ is a function of Y_{NO}^{FPV}, the consumption rate is adjusted by using the computed NO mass fraction from Eq. (27). Thus, the modeled NO production rate can be written as

$$\dot{\omega}_{NO} = \dot{\omega}^+_{NO} + Y_{NO} \frac{\dot{\omega}^-_{NO}}{Y_{NO}^{FPV}}. \tag{30}$$

It is interesting to note that this model converges to that of the unsteady flamelet model, since in this case, $Y_{NO} = Y_{NO}^{FPV}$, ensuring model consistency.

Although the model given by Eqs. (29a) and (29b) was written here for a simple one-step NO formation reaction, it can be used for general detailed reaction schemes by expressing $\dot{\omega}^+_{NO}$ and $\dot{\omega}^-_{NO}$ in terms of the total NO production and consumption rates, respectively. Note also that the model for the NO consumption rate as given above considers only reactions which are first order in NO. This model, however, can be extended by expanding $\dot{\omega}^-_{NO}$ in terms of its corresponding reaction order.
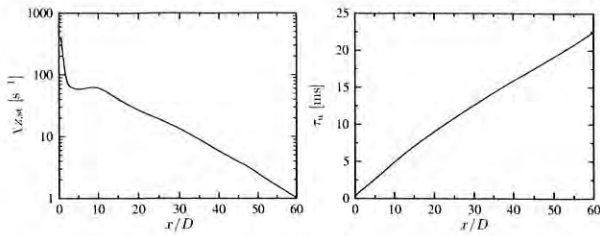
4-48

FIG. 9. Axial evolution of stoichiometric scalar dissipation rate (left) and flamelet lifetime (right) obtained from LES.
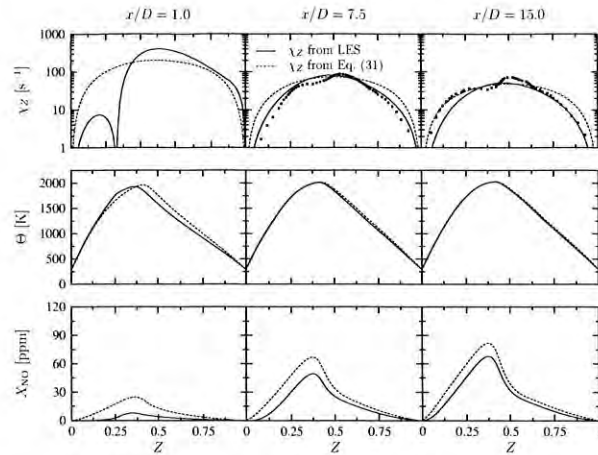

FIG. 10. Comparison of the flamelet structure for temperature and NO mole fraction at three different locations in the jet obtained from an unsteady flamelet simulation for two different profiles of the scalar dissipation rate. For reference, measurements of the scalar dissipation rate for locations $x/D=7.5$ and 15 are shown by symbols (Ref. 47).

B. Model analysis

1. Formulation of the model problem

The model for the prediction of the NO mass fraction, consisting of Eqs. (27) and (30), is investigated in a model analysis. In particular, the three dominant NO formation mechanisms, namely, the thermal, N_2O, and prompt mechanisms, are separately analyzed here.

Because of lack of detailed experimental data that distinguish the individual NO formation pathways, results obtained from an unsteady flamelet simulation are used as a reference. This is mainly motivated by the fact that the unsteady model yields accurate predictions for NO and other species.[34,35] The solution obtained from the unsteady flamelet model can also be seen as the target for the present model, since it was shown in the previous section that the results should be the same under the assumption that all species are in steady state except for NO.

A simplified but realistic model case has been devised for the model analysis. This test case is based on the Sandia flame D configuration. However, in order to separately assess the proposed model and the underlying model assumptions, effects of turbulence are not yet considered. The test case is described in the following.

In the first step, a representative unsteady flamelet is solved subject to a prescribed scalar dissipation rate $\chi_{Z,st}(\tau_u)$. The convective time scale $\tau_u(x)$ and stoichiometric scalar dissipation rate $\chi_{Z,st}(\tau_u)$, shown in Fig. 9, are computed from the LES, which was described in Secs. II D 2 and II D 3. The functional form of the scalar dissipation rate is then obtained from the following analytical expression:[3]

$$\chi_Z(Z) = \chi_{Z,st} \exp\{2([\operatorname{erfc}^{-1}(2Z_{st})]^2 - [\operatorname{erfc}^{-1}(2Z)]^2)\}. \quad (31)$$

Since no further modeling is involved in this equation, its solution is referred to as the reference solution and is denoted in the following by USFM.

In this context, it is important to point out that a pilot is used to stabilize the flame. The pilot not only provides a constant source of heat and radicals but also reduces the scalar dissipation rate on the fuel-lean side of the flame. The effect of the differences in the dissipation rate profiles on the temperature and NO mole fraction are shown in Fig. 10. From this figure, minor differences in the temperature profile at the first measurement station can be seen; however, the peak NO mole fraction is approximately 10 ppm higher in the simulation that employs the analytical expression for χ_Z.

In the following step, we solve the **flamelet equation for NO, to create a state relation for Y_{NO}** let space, viz.,

$$\partial_t Y_{NO} - \frac{1}{2}\chi_Z(\tau_u)\partial_Z^2 Y_{NO} = \dot{\omega}_{NO}. \quad (32)$$

with $\dot{\omega}_{NO}$ from Eq. (30) and $\dot{\omega}_{NO}^-$, $\dot{\omega}_{NO}^+$, and Y_{NO}^{FPV} are obtained from the extended FPV library $\mathcal{G}^e$. The mixture fraction, progress variable, and enthalpy which are input parameters to this library are taken from the unsteady flamelet simulation. For comparison, profiles of Y_{NO}^{FPV} from the flamelet library are also presented in the following.

The chemistry is described by the GRI 2.11 mechanism.[36] From this, three separate mechanism files are compiled by eliminating reactions that are not part of the individual NO formation mechanisms.

In the derivation of the model, essentially four assumptions have implicitly been invoked. These assumptions are summarized here:

(1) A particular flamelet is uniquely identified by Z, C, and H. This essentially reflects the FPV assumption.
(2) In Eq. (30), it is assumed that all species, except NO, are formed on a sufficiently short time scale and can therefore be represented by the species distribution in the flamelet table.
(3) The unsteady flamelets solved for the compilation of the flamelet library evolve along a different trajectory than the representative unsteady flamelet parametrized by $\tau_u(x)$ and $\chi_{Z,st}(\tau_u(x))$. This implicitly assumes that the particular flamelet history is of less importance.
(4) The model for the NO consumption rate in Eq. (30) only considers first-order NO consumption reactions. This, however, can be remedied in a straightforward way but was not further investigated here.

Despite the fact that these assumptions are not separately addressed here, their integral effect on the NO formation is analyzed in the following.
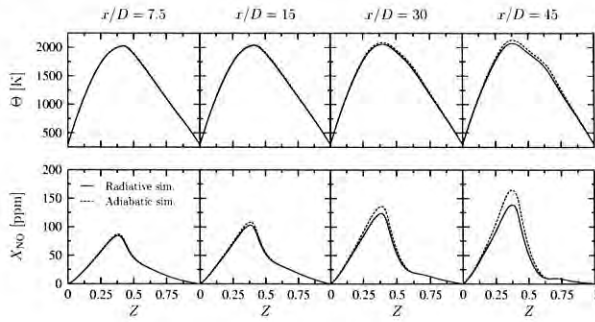
4-49

FIG. 11. Effects of radiation on flamelet temperature and NO mole fraction.

FIG. 12. Comparison of the model results for the Zeldovich mechanism at four different axial locations.

2. Effect of radiation

The effect of radiation on the flame temperature and NO mole fraction is shown in Fig. 11. Two representative flamelets are solved subject to the transient scalar dissipation rate from the LES. The dashed line represents the adiabatic solution, and the profiles shown by the solid lines account for radiation. Radiation in the optically thin limit leads to a decrease in the peak temperature by 70 K at $x/D=45$ and a reduction in NO by 20% to 140 ppm.

3. Zeldovich mechanism

The main source of NO in the combustion of nitrogen-free fuel and air is considered to be the Zeldovich mechanism[37] if the temperature is sufficiently high. The principal reactions are given in the Appendix, Sec. 1, and a corresponding reaction flux diagram is shown in Fig. 23. This mechanism is usually unimportant at temperatures below 1800 K, which is due to the fact that the rate-limiting reaction (A1) has a large activation energy.

The GRI 2.11 mechanism is reduced so that all nitrogen-related reactions, except reactions (A1)–(A3), are deleted. By using this simplified mechanism, flamelets are generated and compiled into a flamelet library. This library, parametrized by Z, C, and H, is then used in the NO model.

Results obtained from the NO model are compared to data from the representative unsteady flamelet model in Fig. 12. Profiles for the NO mole fraction and the contributions to the reaction rate due to production and consumption are shown at four different axial locations. The NO mole fraction is shown in the top row. Compared to the unsteady results, X_{NO}^{FPV} from the extended flamelet library is overpredicted by a factor of 2 for all measurement locations. This can be attributed to the slow NO consumption rate and is discussed in more detail in Sec. III B 5. The slow increase in NO with increasing downstream distance is a manifestation of the large formation time of the thermal mechanism. Except for the last location, the model results can be considered to be in excellent agreement with the reference solution. The reason for the small overprediction at $x/D=45$ can be attributed to the difference of the formation rates $\dot{\omega}_{NO}^{+}$ between both models. A comparison of the flame structure between both models showed differences in the O and N radical profiles. Particularly, the larger concentration of N in the extended FPV model on the fuel-rich side results in a larger production rate
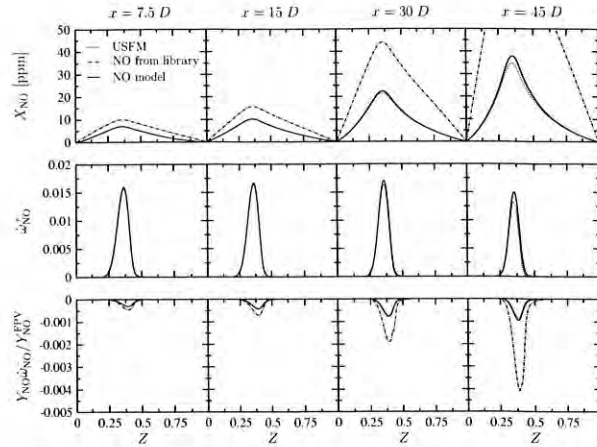
via reaction (A3). On the other hand, the peak O mass fraction in the FPV model is approximately 10% lower than in the representative unsteady flamelet model, resulting in a lower NO production rate from reaction (A1). However, since reactions (A1) and (A3) contribute in equal parts to the overall NO production, both effects nearly cancel.

The last row in Fig. 12 also shows a comparison between the modeled consumption rate and the consumption rate taken from the flamelet library. This shows that a rescaling of the NO consumption rate is a valid and necessary model component.

The effects of the formation rate and rescaled consumption rate on NO formation can be individually analyzed by writing the following zero-dimensional NO evolution equation:

$$d_t Y_{NO}(t) = \dot{\omega}_{NO}^{+} + Y_{NO}(t)\frac{\dot{\omega}_{NO}^{-}}{Y_{NO}^{FPV}} \quad \text{with } Y_{NO}(t=0) = Y_{NO}^{0}. \quad (33)$$

Here, it is assumed that $\dot{\omega}_{NO}^{+}$ and $\dot{\omega}_{NO}^{-}/Y_{NO}^{FPV}$ are independent of time, which is a reasonable assumption for the Zeldovich mechanism (see Fig. 12). The solution of this equation is

$$Y_{NO}(t) = -\frac{\dot{\omega}_{NO}^{+}}{\dot{\omega}_{NO}^{-}}Y_{NO}^{FPV}\left(1 - \exp\left\{\frac{\dot{\omega}_{NO}^{-}}{Y_{NO}^{FPV}}t\right\}\right)$$
$$+ Y_{NO}^{0}\exp\left\{\frac{\dot{\omega}_{NO}^{-}}{Y_{NO}^{FPV}}t\right\}, \quad (34)$$

with the equilibrium NO mass fraction:

$$\lim_{t\to\infty} Y_{NO}(t) = -\frac{\dot{\omega}_{NO}^{+}}{\dot{\omega}_{NO}^{-}}Y_{NO}^{FPV} \quad (35)$$

and the mean lifetime:

$$\tau = -\frac{Y_{NO}^{FPV}}{\dot{\omega}_{NO}^{-}}. \quad (36)$$

From Eqs. (35) and (36), the influence of the consumption rate on the temporal evolution of the NO mass fraction becomes apparent: The typically small consumption rate in the

$$\dot{\omega}_{NO}^{+} = [N][OH]k_{f}^{A3} + [H][HCNO]k_{b}^{A31}. \qquad (37)$$

The overprediction of NO as seen in Fig. 14 can be attributed to the difference in the N profiles between the representative unsteady flamelet model and the NO model. The nitrogen radical profile is 50% larger in the extended FPV model compared to that of the representative unsteady flamelet model. The other minor species OH, H, and HCNO agree well between both models.

In the present case, the most important NO consumption step in the prompt NO mechanism is reaction (A36) with the consumption rate:

$$\dot{\omega}_{NO}^{-} = -[NO][HCCO]k_{f}^{A36}, \qquad (38)$$

and the discrepancy of the consumption rate is attributed to differences in the HCCO profiles and also effects of rescaling.

IV. LES APPLICATION

In a LES application, a transport equation for the Favre-filtered NO mass fraction $\widetilde{Y}_{NO}$ is solved. After multiplying Eq. (27) with the LES filter kernel G and spatial integration, this equation can be written as

$$\bar{\rho}\widetilde{D}_{t}\widetilde{Y}_{NO} = \nabla \cdot (\bar{\rho}\widetilde{\alpha} \nabla \widetilde{Y}_{NO}) + \nabla \cdot \bar{\tau}_{NO}^{res} + \bar{\rho}\widetilde{\omega}_{NO}, \qquad (39)$$

and with the definition

$$\dot{\varpi}_{NO} \equiv \frac{\dot{\omega}_{NO}^{-}}{Y_{NO}^{FPV}}, \qquad (40)$$

the filtered production rate is modeled as

$$\widetilde{\omega}_{NO} = \widetilde{\omega}_{NO}^{+} + \widetilde{Y}_{NO}\widetilde{\varpi}_{NO} + \widetilde{Y_{NO}''\varpi_{NO}''}, \qquad (41)$$

where cross terms are neglected. The last term on the right hand side accounts for residual scale correlations between the computed NO mass fraction and consumption rate. This term cannot directly be obtained from the flamelet library and requires modeling. In this work, closure is obtained by assuming scale similarity between Y_{NO} and Y_{NO}^{FPV}, which can be written as

$$\frac{\widetilde{Y}_{NO}}{\widetilde{Y}_{NO}^{FPV}} = \frac{Y_{NO}''}{Y_{NO}^{FPV''}}. \qquad (42)$$

With this, Eq. (41) reduces to

$$\widetilde{\omega}_{NO} = \widetilde{\omega}_{NO}^{+} + \widetilde{Y}_{NO}\frac{\widetilde{\omega}_{NO}^{-}}{\widetilde{Y}_{NO}^{FPV}}. \qquad (43)$$

The filtered source term contributions $\widetilde{\omega}_{NO}^{+}$, $\widetilde{\omega}_{NO}^{-}$, and $\widetilde{Y}_{NO}^{FPV}$ are precomputed by using the presumed PDF of Eq. (23) and are stored in a flamelet library $\widetilde{\mathcal{G}}_{\psi}^{e}$, which is parametrized in terms of $\widetilde{Z}$, $\widetilde{Z''^{2}}$, $\widetilde{C}$, and $\widetilde{H}$. In the following, transport equations are solved for these three mean quantities, and the residual scalar variance of the mixture fraction is obtained from an algebraic model.[31]
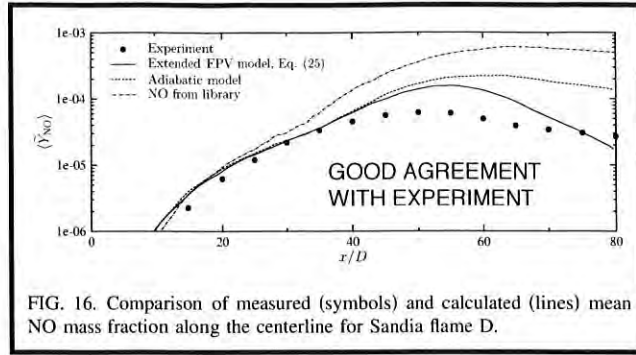

FIG. 16. Comparison of measured (symbols) and calculated (lines) mean NO mass fraction along the centerline for Sandia flame D.

A. Sandia flame D

The transport equation for the Favre-filtered NO mass fraction with the modeled source term, shown in Eq. (43), is solved in addition to the filtered scalar equations describing the evolution of mixture fraction, progress variable, and enthalpy, constituting the extended radiative FPV model. This model is applied in LES of Sandia flame D, and results for the NO formation are presented in the following. The effect of radiation on the NO formation for methane/air chemistry has been investigated in the context of the model analysis in Sec. III B. In that study, the effect of turbulence on the chemistry and radiation was not considered, and it was shown that the consideration of radiative heat losses reduced the NO formation by approximately 20%. In the present section, the effect of the interaction between turbulence, chemistry, and radiation is fully considered, and its dependence on the NO formation is quantified.

In Fig. 16, centerline profiles of the NO mass fraction from the simulations are compared to ensemble-averaged measurements. Additionally, results from the adiabatic simulation and $\widetilde{Y}_{NO}^{FPV}$ from the extended FPV library are shown. It can be seen that the predicted NO mass fraction from the adiabatic and radiative simulations are identical up to $x/D \approx 40$. This result is to be expected, since it was shown in Fig. 7 that both models predict a nearly identical temperature evolution in this region. The location of the peak NO formation is correctly predicted by the model; however, the peak NO value is overpredicted. It is interesting to point out that the adiabatic calculation considerably underpredicts the NO decrease in the fuel-lean part of the flame.

Mixture fraction-conditioned results at different axial locations in the jet flame are compared to experimental data in Fig. 17. It can be seen that the consideration of radiative heat losses results in a NO reduction by approximately 25–30%. The predictions from the radiative NO model are in good agreement with the unsteady flamelet model for the first three measurement stations. In conclusion, it is shown that the consideration of radiative effects is essential for the prediction of NO formation. It is demonstrated that the developed NO model yields considerably improved results compared to the steady flamelet model. NO predictions comparable with the unsteady flamelet model are obtained in the application of the model in the simulation of Sandia flame D. According to the results of the analysis presented in Sec. III B, NO predictions are expected to considerably improve for cases where thermal NO is dominant.
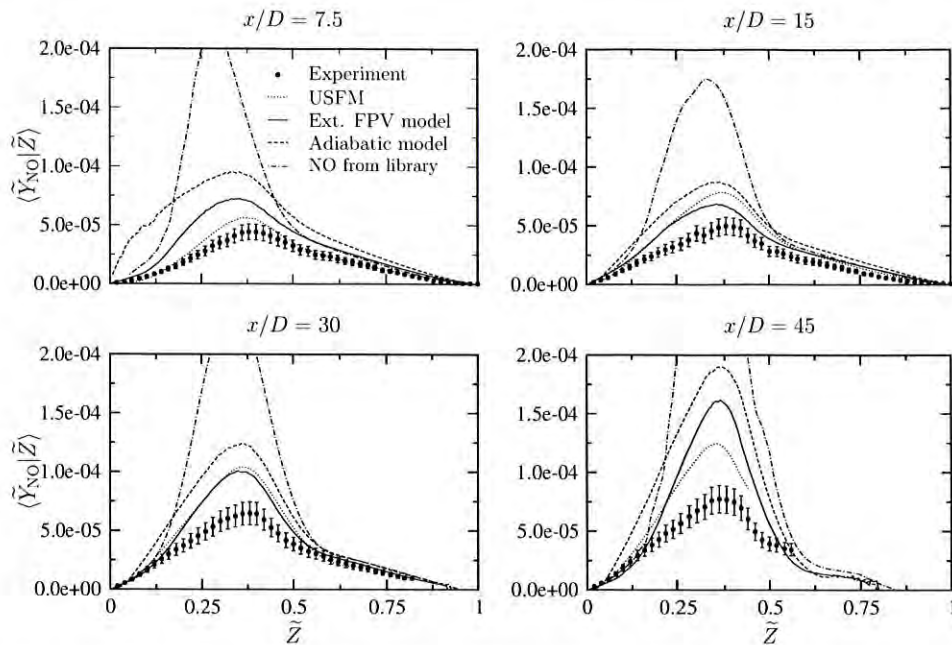
4-51

FIG. 17. Comparison of measured (symbols) and calculated (lines) conditional NO mass fractions at different streamwise locations in the flame. Experimental data are plotted with estimated uncertainties.

B. Pratt & Whitney combustor simulation

The model for the prediction of NO formation was applied in LES of the Sandia flame D experiment in the previous section. The experimental configuration of this flame consists of a central fuel nozzle, a pilot stream for flame stabilization, and a surrounding coflow. Despite the relatively simple geometrical setup, the turbulence/chemistry interaction in this configuration is sufficiently complex to serve as a validation case in the TNF workshop.[24] Results obtained for this free shear-flow configuration showed considerable improvements over previous model results for mean temperature and also mean NO mass fraction.

The successful validation against the Sandia flame experiment encouraged the application of the model to the Pratt & Whitney PW 6000 combustor configuration. The flow field inside the combustor is highly turbulent, swirling, and separated. The liquid fuel atomizes when entering the combustion chamber through the injector. In the combustion chamber, the droplets of fuel interact further by collision or coalescence until they eventually evaporate. The spray flame is stabilized by a recirculation zone, which is created by a swirling flow. Furthermore, air is injected into the combustion chamber through multiple jets, resulting in complex mixing patterns.

Compared with RANS-based models, LES has the potential to predict these unsteady, three-dimensional, geometry-dependent, coherent flow features, and their sensitivity to changes in the combustor design.[40,41] Therefore, numerical simulations of the combustor configuration are performed by using the unstructured, finite-volume LES solver CDP.[42,43] The code includes models for the droplet motion and the breakup and evaporation of the spray, and the gas phase chemistry is described by using the FPV model. The different models for the liquid phase are summarized in the following for completeness. Further details can be found in Ref. 44 and references therein.

The droplet motion is modeled by using the Basset–Boussinesq–Oseen equations in the large density ratio limit between the droplet and gas phase. Under this assumption, the Basset force and the added mass term are small and are therefore neglected. The drag force on the droplet is modeled based on a solid particle with corrections accounting for particle deformation and internal circulation. The direct effect of the residual velocity on the droplet motion is neglected in the present model implementation. Moin and Apte,[44] however, pointed out that the particle motion is indirectly affected by the residual scales through the residual scale model that affects the resolved velocity field.

The atomization process is modeled by a residual secondary breakup model, which is based on a point particle approximation. The liquid fuel sheet, exiting the injector, is approximated by large drops with size equal to the size of the annulus. In the stochastic spray breakup model, it is assumed that the diameter of the droplet is a time-dependent stochastic variable with a given initial size distribution. The secondary breakup follows the temporal and spatial evolution of the distribution function obeying the Fokker–Planck equation. The breakup frequency and critical particle radius appearing in this equation are obtained from the balance between aerodynamic and surface tension forces.

The boundary layer surrounding the droplets are numerically not resolved, which would be necessary for the computation of the evaporation rates. Instead, the droplet evaporation rates are estimated from a uniform state model, and Lagrangian equations for the particle mass and heat transfer are solved. The individual source terms in these equations

4-52

TABLE I. Conditions for the Pratt & Whitney combustor configuration.

Parameter	Value
Stoichiometric condition (−)	$Z_{st}=0.0635$
Fuel stream (−, K)	$Y_{C_{10}H_{22}}=0.8256, Y_{C_9H_{12}}=0.1744, \Theta=171.4$
Oxidizer stream (−, K)	$Y_{O_2}=0.233, Y_{N_2}=0.767, \Theta=812$
Pressure (bar)	20.0

are modeled by using Spalding mass and heat transfer numbers and the Clausius–Clapeyron equilibrium vapor-pressure relationship.

The cooling effect of the gas phase due to the droplet evaporation is accounted for by computing an effective gaseous fuel temperature.[44] Therefore, the gaseous fuel temperature, which is used as a boundary condition in the solution of the flamelet equations, is reduced by the ratio of latent heat of evaporation divided by the specific heat capacity of the liquid fuel.

The combustor simulations are performed for take-off condition. The pressure in the combustion chamber at this operating condition is 20 bars. A surrogate fuel, consisting of 82.6% n-decane ($C_{10}H_{22}$) and 17.4% trimethylbenzene (C_9H_{12}) by mass is used as fuel. The chemical mechanism considers 113 species among 491 chemical reactions.[45] By using this mechanism with the boundary conditions given in Table I, flamelets are computed and compiled into a flamelet library. The simulations are performed for a 20° sector of the full combustor, which consists of a total of 18 injectors. The computational grid consists of 3.64×10^6 control volumes with a finer resolution in the region of the injector and the dilution holes. The Reynolds number, which is based on the nozzle diameter, air inlet velocity, and kinematic viscosity of air at inlet conditions, is approximately 725 000.

The Pratt & Whitney combustor is designed as a rich-quench-lean (RQL) combustor system, incorporating separate zones of combustion to maintain stability while reducing emissions. Combustion is initiated in the fuel-rich zone, in which all fuel is injected. The fuel partially reacts in an oxygen-lean environment and completes approximately 50% of the overall energy release. The combustion products in the fuel-rich zone consist mainly of CO and UHC and essentially no NO_x is formed.[46] The remaining air is rapidly injected in the quenching zone in order to reduce the combustion residence time near the stoichiometric condition. Past the quenching region, the reaction is then completed in the lean zone. In order to minimize NO_x emissions, it is essential to facilitate a rapid transition between the fuel-rich and fuel-lean zones to avoid long residence times around the stoichiometric condition.

In the following, the numerical results are discussed. Therefore, statistical data were collected over 250 nondimensional time units, corresponding to 50 ms real time or roughly 35 flow-through times, at which a flow-through time is defined from the length of the combustor and the characteristic inlet velocity. Note that the dilution holes are not shown in the figures, and all results are normalized.

Figure 18 shows instantaneous and averaged profiles of temperature and NO mole fraction along the axial plane through the combustor. The instantaneous droplet distribution is also shown in Fig. 18(a). The turbulent and complex flame structure and flow pattern can be observed in Figs. 18(a) and 18(b).

The instantaneous NO mole fraction is shown in Fig. 18(b). It can be seen that the NO formation in the primary zone is aligned with the surface of the stoichiometric mixture (shown by the solid line), which is determined by the spray angle. Some NO formation on the fuel-rich side of the flame

(a) Instantaneous Favre-filtered temperature (normalized)

(b) Instantaneous Favre-filtered NO mole fraction (normalized)

(c) Averaged temperature (normalized)

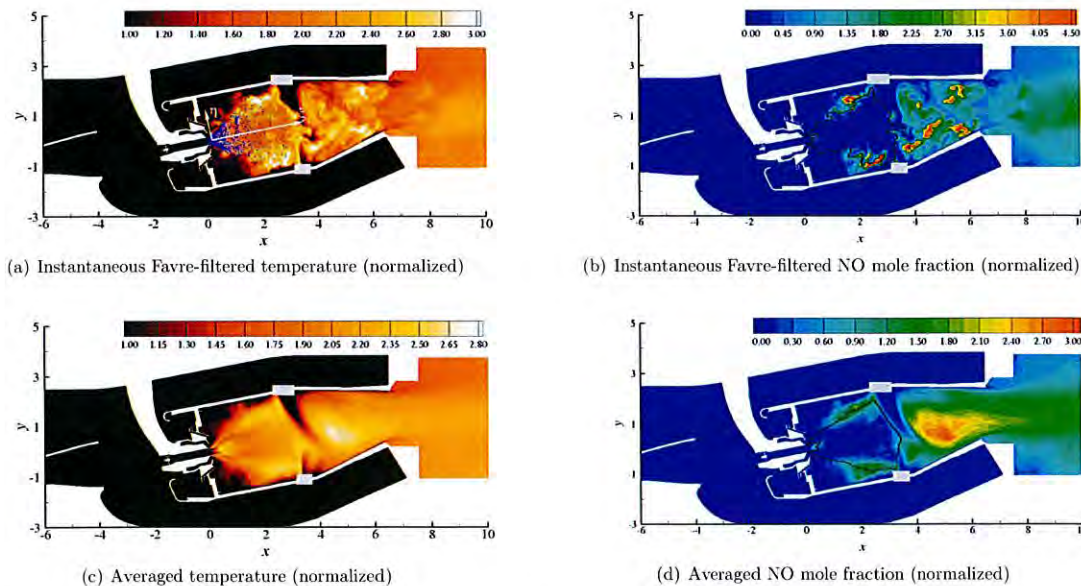(d) Averaged NO mole fraction (normalized)

FIG. 18. (Color) Contours of the instantaneous and mean temperatures and NO mole fractions along an axial cross section in a Pratt & Whitney aircraft engine combustor at take-off condition. The solid lines show the location of the stoichiometric mixture ($Z_{st}=0.0635$).

4-53

LES/PDF based modeling of soot–turbulence interactions in turbulent flames

Pratik Donde [a,*], Venkat Raman [a], Michael E. Mueller [b], Heinz Pitsch [c]

[a] *Department of Aerospace Engineering and Engineering Mechanics, The University of Texas at Austin, Austin, TX 78712, USA*
[b] *Department of Mechanical Engineering, Stanford University, CA 94305, USA*
[c] *Institute for Combustion Technology, RWTH Aachen University, Aachen, Germany*

Available online 4 August 2012

Abstract

A large eddy simulation (LES)/probability density function (PDF) approach is used to describe the small-scale soot–turbulence–chemistry interactions. The PDF approach directly evolves the joint statistics of the gas-phase scalars and a set of moments of the soot number density function. This LES/PDF approach is then used to simulate a turbulent natural gas jet diffusion flame. Since the PDF equation is high dimensional, a Lagrangian method formulated in cylindrical coordinates is coupled to the Eulerian solution technique for the LES flow equations. The LES/PDF simulations show that soot formation is highly intermittent and is always restricted to the fuel-rich region of the flow. The PDF of soot moments has a wide spread leading to a large subfilter variance. Further, the conditional statistics of soot moments conditioned on mixture fraction and reaction progress variable show strong correlation between the gas phase composition and soot moments.
© 2012 The Combustion Institute. Published by Elsevier Inc. All rights reserved.

Keywords: Probability density function; Large eddy simulation; Soot; Non-premixed turbulent flames; Soot–turbulence–chemistry interactions

1. Introduction

Soot formation inside turbulent aircraft combustors is a highly intermittent and unsteady process. In practical combustor designs such as the rich-quench-lean (RQL) operating mode, soot is generated in fuel-rich high temperature regions and is subsequently oxidized after dilution with air. Typically, the amount of soot emitted is the result of the differences between these generation and oxidation processes. More importantly, the generation and oxidation processes are not continuous and occur with very high intermittency, indicating that the temporal history of soot precursors, turbulence-related strain, and combustion processes are critical in determining emission levels. Since all of these processes are highly complex and interact nonlinearly, the development of predictive soot models poses a tremendous modeling challenge.

The use of large eddy simulation (LES) is emerging as a standard practice for turbulent combustion in practical devices [1]. Since LES resolves only large-scale features of the flow, combustion, and soot formation which occur exclusively at the small scales must be modeled.

* Corresponding author. Fax: +1 512 471 3788.
 E-mail address: pratik.donde@gmail.com (P. Donde).

In particular, the highly non-linear small-scale correlations between gas-phase scalars and soot precursor evolution need to be described. Typically, the soot population is described using a set of moments of the underlying number density function. In this context, small-scale correlations are best represented by a one-point one-time joint probability density function (PDF) of the gas-phase scalars and soot moments.

Due to the inherent challenges in describing soot precursor chemistry, turbulence, and combustion processes, not much attention has been given to the modeling of this joint-PDF. In LES, the subfilter correlations between soot and the gas-phase composition are often neglected. In this case, the PDF is written as the product of the marginal PDFs of gas phase scalars and soot moments. However, given the high sensitivity of soot to the flame characteristics, this approximation could potentially introduce large errors. Recently, Mueller and Pitsch [2] have developed a presumed PDF approach, in which the independence of these variables is assumed, but the marginal PDFs of the soot moments are modeled using an intermittency related term. In the Reynolds-averaged Navier–Stokes (RANS) formulation, Lindstedt and Louloudi [3] have directly solved the joint-PDF using a high-dimensional transport equation. It was found that accounting for the composition-soot correlations resulted in significant changes in the soot profiles. Chandy et al. [4] have used the PDF approach in the context of LES, but with a simplified model for the soot chemistry.

The focus of this work is to combine the PDF approach with a detailed description of unsteady soot precursor chemistry, particulate dynamics, and gas-phase radiation. Detailed chemistry for soot precursor evolution and the gas-phase turbulent combustion process is described using a modified flamelet/progress variable approach. To account for radiation effects, an additional state space parameter in the form of the radiation heat loss parameter is used. The soot population is described using a bivariate volume/surface area formulation that allows for surface processes to be modeled more accurately. Finally, the joint-PDF of the soot moments and the gas-phase scalars is solved using a Lagrangian Monte Carlo technique. This methodology is then used for studying small scale composition-soot correlations in an experimental piloted natural gas flame [5–7].

2. LES/PDF approach for sooting flames

In this section, the governing equations for the models (Sections 2.1 and 2.2) and the joint-PDF formulation (Section 2.4) are discussed. The component models include the description of the

soot population evolution and the gas-phase turbulent combustion model. LES will be used to describe the turbulent flow, and the correlations in the filtered composition and soot equations will be closed using the joint-PDF formulation.

2.1. Volume/surface area based soot model

The evolution of the soot population is described using a population balance equation (PBE) for the number density function $N(\zeta; \mathbf{x}, t)$, where ζ is a vector of internal coordinates. In order to account for fractal aggregates, two internal coordinates are used to describe the number density function: volume V and surface area S [8]. Since a direct solution to the PBE is intractable, the soot population is represented by moments of the NDF:

$$M_{x,y} = \int V^x S^y N \, d\zeta, \tag{1}$$

where x, y are the orders of the moment in volume and surface area, respectively. The transport equation for the moments obtained from the PBE using the above definition of moments (Eq. (1)) can be written as:

$$\frac{\partial M_{x,y}}{\partial t} + \frac{\partial u_j M_{x,y}}{\partial x_j} = S_{x,y}^M(\zeta, \xi), \tag{2}$$

where $S_{x,y}^M$ represents the moment source terms accounting for nucleation, growth, and oxidation of soot particles, and ξ is a vector of thermochemical composition variables. A nucleation model based on dimerization of polycyclic aromatic hydrocarbons (PAH) [9] is used in this study, and growth is modeled using the H-abstraction–C_2H_2-addition (HACA) mechanism [10]. Reaction rates proposed by Mueller et al. [11] are used for oxidation. Since only a finite number of moments are solved for, the moment source terms are unclosed. Closure is obtained with the hybrid method of moments (HMOM) [12]. The model is designed to capture the bimodality of the NDF while retaining numerical efficiency and robustness.

In HMOM, the contribution of the smaller particles to the moments is represented with a delta function, and the contribution of the large particles is represented with polynomial interpolation. Any moment of the soot NDF can then be written as

$$M_{x,y} = N_0 V_0^x S_0^y + M_{x,y}^R, \tag{3}$$

where N_0, V_0, and S_0 are the weight and internal coordinates of the delta function. V_0 and S_0 are prescribed *a priori*, and a transport equation is solved for N_0. $M_{x,y}^R$ is polynomial interpolation of order R [13]. In this work, first-order interpolation is considered, and three moments, the soot number density $M_{0,0}$, volume $M_{1,0}$, and surface

area $M_{0,1}$, are needed to determine the interpolation coefficients. The reader is referred to [12] for further details related to HMOM.

2.2. Gas-phase chemistry

Soot inception depends on accurate modeling of not only the fuel oxidation but also the formation of soot precursors such as PAH. Therefore, a combustion model is needed that can account for this detailed chemistry. In this work, the radiation flamelet/progress variable (RFPV) model for sooting flames developed by Mueller and Pitsch [14] is used. This model accounts for gas-phase radiation using an optically thin assumption. The thermochemical composition vector ξ is parameterized using three variables, namely, mixture fraction (Z), a reaction progress variable (C), and a radiation heat loss parameter (H). In addition, the unsteady evolution of PAH is modeled by solving a transport equation for the total PAH mass fraction Y_{PAH}. Transport equations for the variables representing the thermochemical composition vector are written as follows:

$$\frac{\partial \rho \kappa}{\partial t} + \frac{\partial \rho u_j \kappa}{\partial x_j} = \frac{\partial}{\partial x_j}\left(\rho D \frac{\partial \kappa}{\partial x_j}\right) + \rho S(\kappa), \quad (4)$$

where $\kappa = [Z, C, H, Y_{PAH}]$, and $S(\kappa) = [S_Z, S_C, S_H, S_{PAH}]$ represents appropriate source terms. PAH removal due to soot formation results in source terms in the continuity equation. As a result of this, a conserved scalar formulation cannot be used for mixture fraction, leading to the source term S_Z. In Eq. (4), $\rho S_H = \dot{\rho}H + \dot{q}_{RAD}$, where $\dot{q}_{RAD}$ is the radiation source term. For the flame studied in Section 4, the effect of soot oxidation on gas-phase composition is expected to be minimal, and is neglected here. The flamelet equations [15] are solved and the solutions are stored in a table for subsequent look-up of the source terms. In addition to the steady flamelet solutions, the RFPV approach includes unsteady flamelet solutions for parameterizing with respect to H. Further details of the RFPV approach can obtained from Mueller and Pitsch [14].

2.3. LES flow equations and source term closure

In LES, the continuity, momentum, and the scalar transport equations described above are filtered using a low-pass filter. For instance, any field Q could be filtered using a Favre-weighting approach as follows:

$$\widetilde{Q}(\mathbf{x}) = \frac{1}{\bar{\rho}} \int \rho Q G(\mathbf{x} - \mathbf{y}) d\mathbf{y}, \quad (5)$$

where $\bar{\rho}$ is the filtered density, $\widetilde{Q}$ is the Favre-filtered field, and G is the filter kernel. If the parameters required to describe the thermochemical composition variables and the soot population are taken as a scalar set (i.e., $\psi = [Z, C, H, Y_{PAH}, M_{x,y}, N_0]$), the filtered scalar transport equation could be written as

$$\frac{\partial \bar{\rho}\tilde{\psi}}{\partial t} + \frac{\partial \bar{\rho}\tilde{u}_j\tilde{\psi}}{\partial x_j} = \frac{\partial}{\partial x_j}\left(\bar{\rho}(D + D_t)\frac{\partial \tilde{\psi}}{\partial x_j}\right)$$
$$+ \bar{\rho}\widetilde{S(\psi)}, \quad (6)$$

where D_T is a turbulent diffusivity that is used to model the subfilter turbulent flux using the gradient diffusion hypothesis.

The main modeling issue arises from the filtered source terms $\widetilde{S(\psi)}$ which are highly nonlinear and strongly coupled. For instance, soot growth and oxidation rates are highly dependent on the gas-phase composition and temperature. At the same time, coagulation of soot particles depends on interactions between soot particles of different sizes. Hence, the subfilter correlations of these quantities need to be explicitly modeled. The most comprehensive description of these correlations is in terms of the subfilter one-time one-point PDF P of ψ. Filtered source terms are defined as

$$\widetilde{S(\psi)} = \frac{1}{\bar{\rho}} \int \rho S(\phi) P(\phi) d\phi, \quad (7)$$

where ϕ represents the ψ vector in sample space. This joint-PDF is required at every point in the flow. The solution of the transport equation for this PDF is discussed next.

2.4. Transported PDF approach

In the transported PDF approach, a partial differential equation describing the evolution of the PDF in physical and compositional spaces is directly solved. The focus of this study is the simulation of a turbulent jet flame in cylindrical coordinates. For this purpose, the transport equation is written in cylindrical coordinates as follows [16]:

$$\frac{\partial G_L}{\partial t} + \frac{\partial}{\partial r}\left[\left(A_r + \frac{B}{r}\right)G_L\right] + \frac{\partial}{\partial \theta}\left(\frac{A_\theta}{r}G_L\right)$$
$$+ \frac{\partial}{\partial x}(A_x G_L) + \frac{\partial^2}{\partial r^2}(BG_L) + \frac{\partial^2}{\partial \theta^2}\left(\frac{B}{r^2}G_L\right)$$
$$+ \frac{\partial^2}{\partial x^2}(BG_L) = -\frac{\partial}{\partial \phi_x}\left[\left(\widetilde{\mathscr{M}_x|\psi} + S_x(\phi)\right)\frac{G_L}{r}\right], \quad (8)$$

where $G_l = rP$, $B = D_T$, and $\mathbf{A} = [A_r, A_\theta, A_x] = \tilde{\mathbf{u}} + 1/\bar{\rho}\nabla \cdot (\bar{\rho}B)$. The terms on the RHS of the PDF transport equation (Eq. (8)) represent transport in composition space and consist of molecular mixing and chemical reactions, respectively. The primary advantage of the PDF approach is that the chemical source term appears closed and does not require modeling. However, modeling is required for describing the conditional diffusion term, $\widetilde{\mathscr{M}_x|\psi}$:

4-56

$$\widetilde{\mathcal{U}_\alpha | \psi} = \frac{1}{\bar{\rho}} \overline{\nabla \cdot \rho D \nabla \phi_\alpha | \psi}. \tag{9}$$

This term is closed using the interaction by exchange with the mean (IEM) model [17–19]:

$$\frac{\partial}{\partial \phi_\alpha}(F_L \widetilde{\mathcal{U}_\alpha | \psi}) = \nabla \cdot \bar{\rho} \widetilde{D} \nabla F_L / \rho$$

$$+ \frac{\partial}{\partial \phi_\alpha}\left[\frac{1}{\tau}(\phi_\alpha - \widetilde{\psi}_\alpha) F_L \right]. \tag{10}$$

Here τ is a mixing time-scale that needs to be specified, and $\widetilde{D}$ is a common diffusivity that is used for all the scalars in ψ. In this work, this is taken to be equal to the diffusivity of mixture fraction. Note that the differential diffusion between soot moments and the gas-phase scalars could be important [20], potentially influencing transport of soot in mixture fraction space [21]. As a first step, this effect has been neglected here, but differential diffusion effects could be considered using formulations proposed elsewhere [22,23]. For the flame considered in Section 4, thermophoresis of soot particles was found to be negligible in a preliminary coarse LES, and, therefore, is not included here.

3. Numerical implementation

The PDF approach is integrated with a low Mach number LES solver. The LES governing equations are solved in cylindrical coordinates using a fractional time stepping procedure [24,25]. A conservative finite difference approach is used for discretizing the nonlinear and viscous terms [26]. A Poisson equation system is used to enforce the continuity equation. Further details of the LES solver can be found in [26].

The transported PDF approach requires solution of the high-dimensional PDF transport equation (Eq. (8)), which spans 11 dimensions for the state vector used in this work. Conventional finite difference or finite volume methods are not tractable, and a Lagrangian Monte-Carlo method is used here [17,18,27,19,28]. In the Lagrangian approach, the computational domain is seeded with a large number of notional particles that evolve in physical and compositional spaces using a set of stochastic differential equations. Each of these particles carries a property vector that consists of the particle location vector, a characteristic weight, and the ψ vector. The evolution of the particles in physical space is governed by the following equations:

$$dr^n = \left(A_r^n + \frac{B_1^n}{r^n} \right) dt + \sqrt{2dt B_1^n} dW_r, \tag{11}$$

$$d\theta^n = \frac{A_\theta^n}{r^n} dt + \sqrt{2dt \frac{B_1^n}{(r^n)^2}} dW_\theta, \tag{12}$$

$$dx^n = A_x^n dt + \sqrt{2dt B_1^n} dW_x, \tag{13}$$

where the superscript n denotes the particle index, and dW_i is a Weiner diffusion process with zero mean and variance of 1, and $B_1 = D + D_T$. The velocity and diffusivity fields used in this equation are interpolated onto the particle locations using trilinear interpolation. The transport in composition space consists of mixing and chemical reactions. The particle equation corresponding to the IEM mixing model is given by

$$d\phi^n = \frac{1}{\tau}(\tilde{\psi} - \phi^n), \tag{14}$$

where $\tilde{\psi}$ is the filtered composition vector in a given filter volume, ϕ^n is the particle composition vector, and τ is a mixing time scale. In this work, the mixing time scale is determined using the local effective diffusivity and the filter scale.

$$\tau = c_\phi \frac{\Delta^2}{D + D_T}, \tag{15}$$

where c_ϕ is a model coefficient. The dynamic procedure proposed by Raman and Pitsch [28] is used for evaluating c_ϕ. The particle equations thus reduce to solving a vector of ordinary differential equations.

$$d\phi^n = \mathbf{S}(\phi^n) dt, \tag{16}$$

where $\mathbf{S}$ is the vector of source terms defined in Eq. (6), and is obtained from precomputed flamelet libraries and local values of Y_{PAH}, $M_{x,y}$, and N_0.

The particle weights are proportional to the mass of the fluid they represent. It should be noted that the PDF transport equation is formulated for rF_L instead of F_L. This modified formulation ensures that the weights have no evolution equation. In other words, the particle weights are initialized at the inlet but do not change with time. To ensure consistency, the particle weights are set proportional to $\bar{\rho}^n r_0^n$ at the inlet, where $\bar{\rho}^n$ is the Eulerian density interpolated to the particle location, and r_0^n is the radial location of the particle.

4. Delft flame: simulation details

Delft flame III [5] is a piloted turbulent jet diffusion flame fueled by commercial natural gas. The use of natural gas results in a non-sooting region near the burner and a downstream moderately sooting region. The burner consists of a central fuel jet with a diameter of 6 mm surrounded by an annulus of air with an inner diameter of 15 mm and an outer diameter of 45 mm [6]. The fuel velocity is 21.9 m/s, and the air velocity is 4.4 m/s. Twelve circular pilot flames with diameters of 0.5 mm are situated on a ring between the fuel jet and the air annulus with a diameter of 7 mm. In the simulation, the pilot is modeled

as an annulus with a width equal to the diameter of the individual pilots in the actual burner. The burner assembly is surrounded by a slow co-flow of air with a velocity of 0.3 m/s.

Three sets of experimental measurements have been made with the burner. In the near-burner region where soot is not present, velocity measurements were made by Stroomer [29], and temperature and species mass fractions were measured by Nooren et al. [6]. More recently, soot volume fraction was measured in the downstream region by Qamar et al. [7].

A $384 \times 192 \times 64$ grid clustered near the jet shear layers, and spanning $150d \times 43d$ in the axial and radial directions is used, where d is the jet diameter. Transient inflow velocity profiles for the central jets (fuel and air) are obtained from separate simulations of the burner geometry. The co-flow is prescribed as a bulk flow. For chemical kinetics, a detailed 158 species mechanism developed by Narayanaswamy et al. [30] has been used with modifications from Mueller and Pitsch [14]. The flamelet lookup library is constructed using Flamemaster [31], and is stored in a lookup table spanning $100 \times 50 \times 35$ points in Z, C, and H directions, respectively. This study was conducted using 256 CPU cores for roughly 400 h, during which statistics were collected over approximately 100 ms.

5. Results and discussion

5.1. Instantaneous fields

Figure 1 shows the instantaneous fields of temperature, PAH mass fraction, soot volume fraction, and soot number density. As expected, soot formation is predominant in the fuel-rich region inside the stoichiometric surface where moderately high temperatures aid the formation of PAH molecules. While PAH formation is initiated far upstream ($x/d > 20$), significant soot volume fraction is observed only after $x/d = 60$. The lag between PAH growth and soot formation shows the time scale differences between the two processes. Similar to the experiment, soot formation is found to be highly intermittent with sporadic bursts of high soot volume fraction regions followed by extended periods of low soot volume fraction. Prior studies have demonstrated that soot precursor growth, especially the evolution of naphthalene, is highly sensitive to the strain rates in the flow. Consequently, the turbulent features that a fluid packet experiences strongly dictates soot nucleation [32]. Figure 1 also shows that the soot number density starts to increase far upstream due to nucleations up to $x/d = 20$. Further downstream, the number density remains essentially constant, while soot volume fraction increases drastically, indicating significant particle

growth assisted primarily by coagulation and PAH condensation. Finally, at $x/d > 80$, oxidation dominates and quickly eliminates soot

5.2. Soot and gas-phase statistics

Figure 2 shows the time-averaged mixture fraction and temperature statistics for the flame, measured far upstream of the region of high soot volume fraction. Results indicate that the LES/PDF predicts the flame statistics reasonably accurately, including the RMS statistics of the flow. In the transported PDF approach, the subfilter mixing model (Eq. (14)) is a source of spatial numerical diffusion since it mixes particles that are spatially distributed within a single control volume. As the dissipation rate increases, the higher mixing rates lead to increased numerical diffusion that will manifest as reduced temporal fluctuations. The accuracy of the RMS statistics provides confidence that the PDF numerics have not unduly affected the flame computation.

Figure 3 shows the soot volume fraction obtained from the LES/PDF approach and the experiments. The simulation results overpredict the soot volume fraction substantially, and also show an earlier inception and growth compared to the experiments. Mueller and Pitsch [14] reported that the magnitude of soot profiles displayed large sensitivity to the dissipation rate models used. Here, a dynamic procedure is used to evaluate the dissipation rate [28]. While this approach was shown to correctly predict extinction levels in partially-premixed flames, LES models that depend on scalar gradients are susceptible to high numerical errors [33,34], which would partially explain the over prediction here. The location of inception, however, is not affected by dissipation rate but is more sensitive to the chemistry model [14].

Although the scalar comparisons upstream (Fig. 2) are reasonably good, it is not known if the minor errors seen upstream will propagate and amplify further downstream. For instance, the mixture fraction plots show an over-prediction of roughly 15% near the centerline, while the temperature itself is nearly the same as experiments. This mismatch could lead to fuel-rich high temperature regions downstream that will promote the formation of soot particles. Without further information on the scalar profiles downstream, it is not possible to deduce the role of these errors in prediction errors.

5.3. Subfilter soot and scalar statistics

From the particle information, subfilter statistics and PDFs can be computed to better understand soot evolution. Figure 4 shows the instantaneous contours of subfilter standard deviation of mixture fraction, temperature, soot
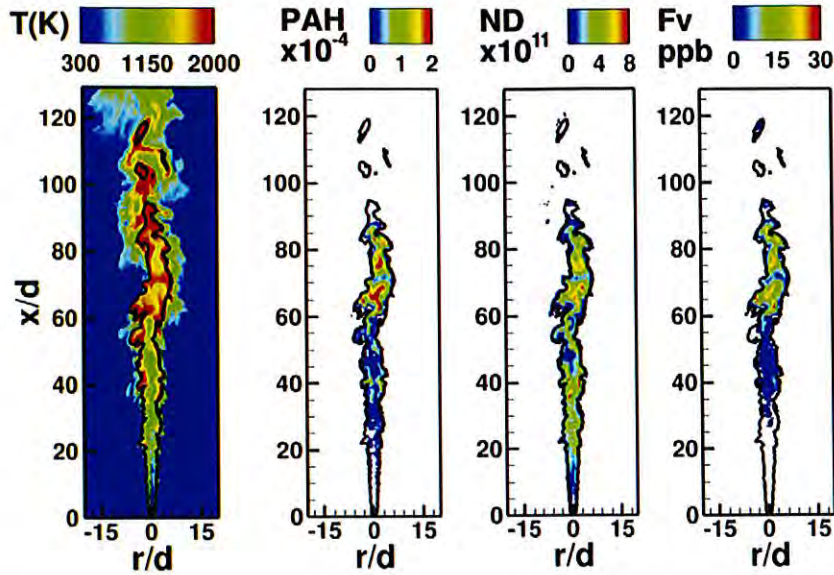
Fig. 1. Instantaneous contours of temperature, PAH mass fraction, soot volume fraction, and soot number density. Iso-value of stoichiometric mixture fraction is indicated by a solid black line. (For interpretation of the references to color in this figure legend, the reader is referred to the web version of this article.)
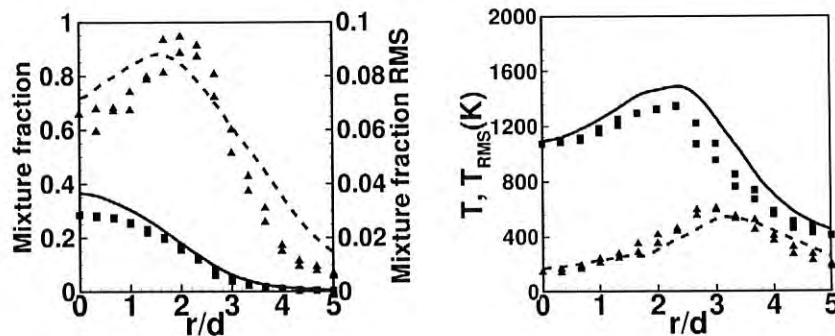

Fig. 2. Comparison of time averaged mean and RMS of mixture fraction and temperature with the experiment of Nooren et al. [6] at $x/d = 41.7$. Simulation: mean (▬), RMS (▪▪▪▪). Experiment: mean (■), RMS (▲).
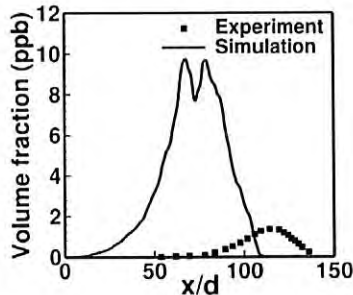
Fig. 3. Comparison of soot volume fraction from the simulation with the experiment of Qamar et al. [7]. The data is plotted along the centerline.

volume fraction, and number density. It is seen that the subfilter fluctuations of mixture fraction are confined to the near-stoichiometric region, with the variations essentially reduced to zero outside of this region. While temperature fluctuations follow a similar pattern, the high standard deviation regions are seen on the lean-side of the flame, outside the closed surface formed by the stoichiometric contour. Due to the large gradient of temperature in mixture fraction space, small fluctuations in mixture fraction lead to large changes in temperature in lean mixtures. The sub-filter fluctuations of soot moments are also large, reaching as high as 40% of the mean values. Similar to the filtered moments, the peaks in these quantities are located in the relatively high-temperature fuel-rich regions inside the stoichiometric surface.

Figure 5 shows the time-averaged PDF of scalars computed at different axial locations, slightly off the centerline. Here, data sets at several
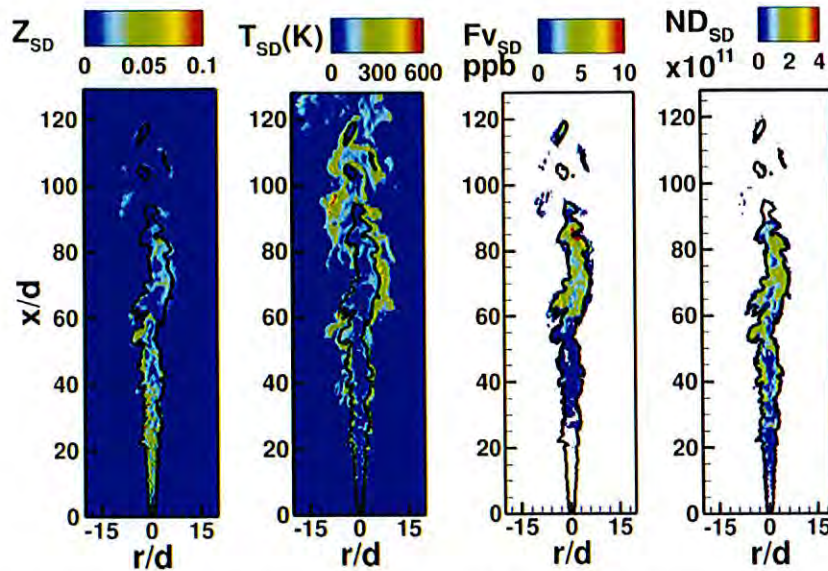
Fig. 4. Instantaneous contours of subfilter standard deviation of mixture fraction, temperature, soot volume fraction, and soot number density. Iso-value of stoichiometric mixture fraction is indicated by a solid black line. (For interpretation of the references to color in this figure legend, the reader is referred to the web version of this article.)

instances, spanning more than 70 ms, have been used to obtains time-averaged distribution functions. In this sense, the PDF is not a true sub-filter quantity, which would require conditioning on the filtered field [1,35]. Note that $x/d = 70$ represents the axial plane with highest soot volume fraction in the simulation (see Fig. 3). The progress variable is skewed towards the values greater than 0.8, indicating a fully burning mixture. The mixture fraction PDF (not shown here) shows a broader spread, with significant probability of having fuel-rich pockets. The PAH PDF shows a bi-modal behavior with a large fraction of the particles having near-zero PAH concentrations and another group of particles with higher PAH values. These two groups of particles come from the fuel-lean and fuel-rich sides, respectively, corresponding to the broad mixture fraction PDF observed. The PDF of soot moments exhibits a broad and nearly uniform PDF, with a bias towards zero moment corresponding to the fuel-lean mixture fraction values.

5.4. Conditional statistics

The evolution of the soot particles in mixture fraction and reaction progress variable coordinates is illustrative of the evolution process. Figure 6 shows time averaged plots of PAH mass fraction, soot volume fraction and soot number density, conditioned on mixture fraction, at $x/d = 70$. All three quantities show a peak in values near a mixture fraction of 0.165, which seems to be the most likely fuel composition to

contain soot. It is also seen that there is a near linear increase in the quantities in the region of $0.075 < Z < 0.16$, but the profiles have a non-linear shape in richer mixtures. To further understand these conditional statistics, Fig. 7 shows the instantaneous conditional scatter plot at two different locations (at the same instance as that in Figs. 1 and 4). It is seen that when the filtered soot volume fraction is lower (<20 ppb), the conditional plots show a wider spread with richer regions containing significant soot volume fractions. Here, the mixture fraction PDF itself is broader, with a wider range of values present. However, when the filtered soot volume fraction is higher ($x/d = 90$), the mixture fraction distribution appears narrower, and the conditional scatter plot exhibits a linear profile. These two modes result in the behavior seen in Fig. 6.

Figure 8 shows the two-dimensional scatter plots of PAH mass fraction and soot volume fraction in $\{Z, C\}$ space. The plots show that PAH is significantly higher in a small region with very high progress variable in the fuel-rich region. Soot volume fraction, on the other hand, has a wider spread with large soot volume fractions seen in regions of lower progress variable (and lower temperature) inside the fuel-rich region. This indicates that the soot particles travel away from the region of high PAH concentration. Some of this soot formation could be due to surface growth, which is independent of PAH concentration. It is also important to note that these conditional statistics are sensitive to the subfilter mixing model used. Since soot particles do not diffuse, the assumption
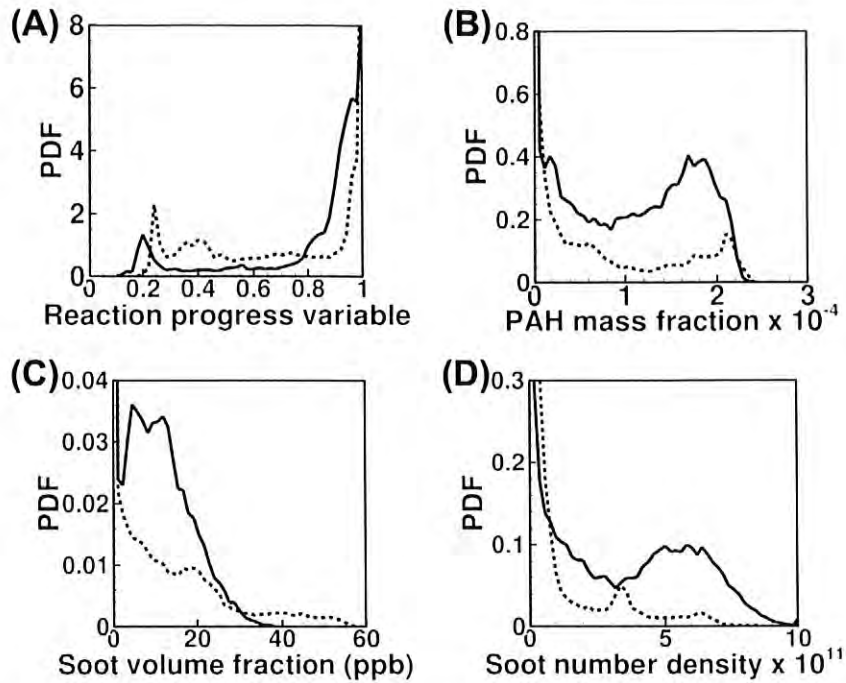
Fig. 5. Time averaged marginal PDFs of (A) reaction progress variable, (B) PAH mass fraction, (C) soot volume fraction, and (D) soot number density plotted at $r/d = 1.5$. $x/d = 70$ (——), $x/d = 90$ (▪▪▪▪). For averaging, data from multiple instantaneous fields was used.
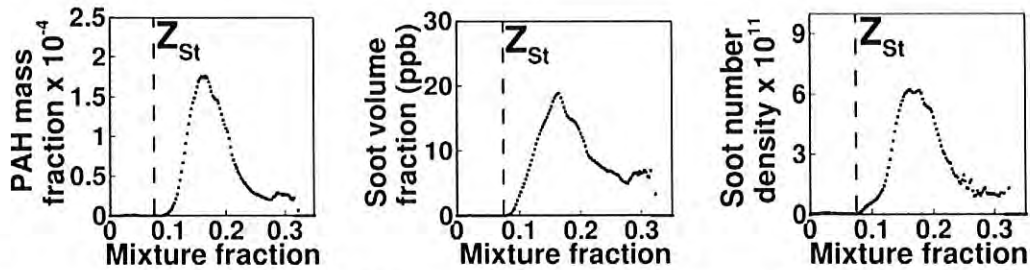
Fig. 6. Time averaged conditional plots of PAH mass fraction, soot volume fraction, and soot number density plotted at $x/d = 70$. Z_{St} indicates stoichiometric mixture fraction. For averaging, data from multiple instantaneous fields was used.
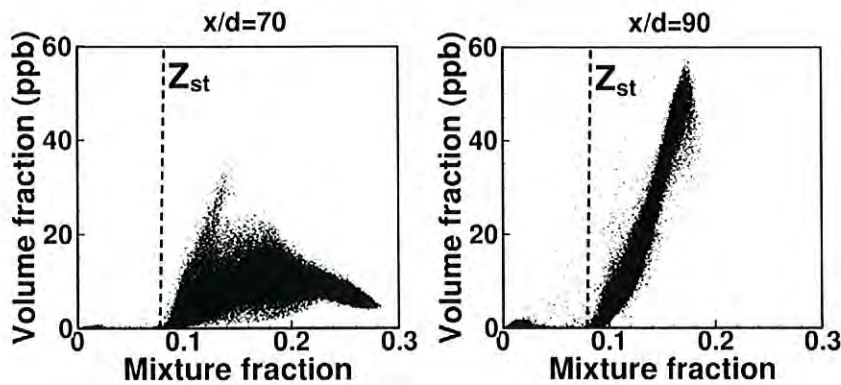
Fig. 7. Instantaneous scatter plot of soot volume fraction versus mixture fraction plotted at $x/d = 70$ (left) and $x/d = 90$ (right).

4-61
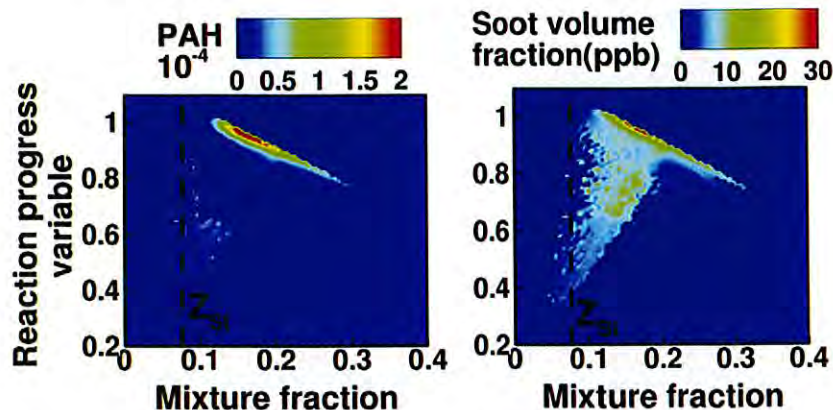
Fig. 8. Time averaged contours of PAH mass fraction and soot volume fraction conditioned on mixture fraction and reaction progress variable plotted at $x/d = 70$. Z_{St} indicates stoichiometric mixture fraction. For averaging, data from multiple instantaneous fields was used.

of equal diffusivities will have some impact on the results obtained here. In particular, soot oxidation in the near-stoichiometric region should be higher than that seen in this simulation. Since the IEM model allows the notional particles to mix without reacting thereby allowing traversal in composition space across flame fronts, the effect of oxidation is under-predicted. The influence of differential diffusion on soot evolution needs further consideration.

6. Conclusions

The LES/PDF approach was used to simulate turbulent sooting flames. Detailed gas-phase precursor kinetics were included using an extended flamelet/progress variable approach that accounts for radiation effects as well as unsteady PAH formation. While the LES computations over-predicted soot volume fraction compared to experiments, it qualitatively reproduced the soot profiles by recreating the gradual increase in soot volume fraction through inception and growth, followed by a quick decrease due to oxidation. The quantitative error in predictions can be attributed to errors in modeling sub-filter dissipation in the PDF approach, the flamelet-based gas-phase chemistry approximation, and uncertainties in reaction rates for dimer and PAH formation. The subfilter standard deviation of soot moments is comparable to the filtered values. The subfilter PDF of soot moments shows a broad spread with a bias towards zero soot content, consistent with the highly intermittent soot formation observed in these flames. Further, conditional statistics show significant scatter of soot moments with respect to mixture fraction. In general, the peak in soot volume fraction occurs close to a mixture fraction value of 0.165, whereas the stoichiometric mixture fraction is only 0.075. In the flow configuration considered, modeled

soot is formed far downstream where turbulent fluctuations are weaker compared to the near-nozzle locations. The conditional statistics from the model show that PAH is confined to a narrow region in mixture fraction/progress variable space, while the soot moments show broader spread.

Acknowledgements

References

[1] H. Pitsch, *Ann. Rev. Fluid Mech.* 38 (2006) 453–482.
[2] M.E. Mueller, H. Pitsch, *Phys. Fluids* 23 (2011) 115104.
[3] R. Lindstedt, S. Louloudi, *Proc. Combust. Inst.* 30 (2005) 775–783.
[4] A.J. Chandy, D.J. Glaze, S.H. Frankel, *J. Heat Transfer Trans. ASME* 131 (2009).
[5] T. Peeters, P. Stroomer, J. de Vries, D. Roekaerts, C. Hoogendoorn, *Symp. (Int.) Combust.* 25 (1994) 1241–1248.
[6] P. Nooren, M. Versluis, T. van der Meer, R. Barlow, J. Frank, *Appl. Phys. B* 71 (2000) 95–111.
[7] N.H. Qamar, Z.T. Alwahabi, Q.N. Chan, G.J. Nathan, D. Roekaerts, K.D. King, *Combust. Flame* 156 (2009) 1339–1347.
[8] M.E. Mueller, G. Blanquart, H. Pitsch, *Proc. Combust. Inst.* 32 (2009) 785–792.
[9] G. Blanquart, H. Pitsch, in: *Combustion Generated Fine Carbonaceous Particles*, Karlsruhe University Press, 2009, pp. 437–463.
[10] H. Wang, M. Frenklach, *Combust. Flame* 110 (1997) 173–221.
[11] M. Mueller, G. Blanquart, H. Pitsch, *Proc. Combust. Inst.* 33 (2011) 667–674.

4-62

Future challenges - for Kilohertz laser diagnostics, LES and DNS

Highly unsteady combustion physics   combustion instability ("growl")
                                                        structure of turbulent flames
                                        how to apply Law's theory of flame stretch to
                                        highly turbulent flames ? Extinction, acceleration ?
                                        does Landau instability dominate turbulent wrinkling ?
                                            base of lifted jet flame – explain liftoff, blowout

Use kilohertz wisely, use LES wisely - look at the dynamics, don't just generate data !

Add heavy hydrocarbon chemistry to turbulent flame studies

DNS: Blanquart (Cal Tech), Poludnenko (NRL), Bell (LBL), Jackie Chen (Sandia)

Experiments: Ju (Princeton), Egolfopolous (USC)

Your airplane flight here was not powered by methane - but by Jet-A !

11

Best models of non-premixed turbulent flames

1.   SSLF = steady strained laminar flamelet - Z & dissip rate (Peters, Pitsch)

2.   FPV = flamelet progress variable – Z, c variables,
                                                        no dissip rate (Moin)

3.   PDF = method of Pope – parcels mix, mixing time eqn, Langevin eqn

4.   CMC = Conditional Moment Closure – Bilger

5.   LEM = Linear Eddy Model – Kerstein, Menon

12

Simplest model of a turbulent non-premixed jet flame

Kuo, K. Principles of Combustion

1. Solve the laminar jet flame equations
2. **Replace molecular diffusivity D with turbulent diffusivity D_T**
3. Show that in a jet D_T is constant everywhere

$$Z(x,r) = \frac{u(x,r)}{U_F} = \frac{3}{32} \frac{d_F}{x} \left(\frac{U_F \, d_F}{D_T}\right) \left(1 + \frac{\xi^2}{4}\right)^{-2}$$

$$\xi = \left(\frac{r}{x}\right) \left(\frac{U_F \, d_F}{D_T}\right) \frac{\sqrt{3}}{8}$$

$$D_T \sim u'_{CL} \, L \sim U_{CL} \, L \sim \frac{U_F}{x/d_F} \, x \sim U_F \, d_F$$

$$Z_{CL} = \frac{3}{32} \frac{d_F}{x} \left(\frac{U_F \, d_F}{D_T}\right)$$
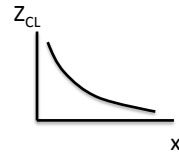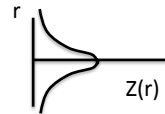
13

Mean radial velocity (v) - in simple jet model

$$v = U_F \left(\frac{x}{d_F}\right)^{-1} \left(\xi - \frac{\xi^3}{4}\right) \left(1 - \frac{\xi^2}{4}\right)^{-2}$$

radially inward

radially outward

v = mean radial velocity

Flame location
Set $Z = Z_{st} = 0.55$
Plot eqn on previous slide
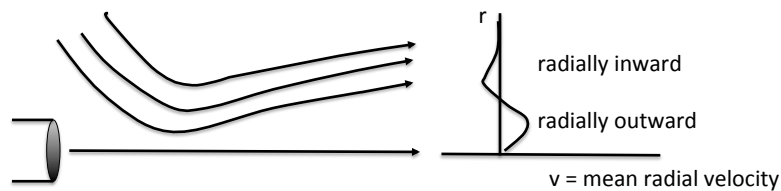
Flame length = flame location at r = 0, $L_f = d_F$ [constant/Z_{st}]

14

Next level of modeling non-premixed turbulent Jet Flame

– Unstrained flamelets   Lockwood and Naguib, Comb. Flame 24, 109

he defines mixture fraction
as f ; it is the same as Z

$$\rho\, u\, \frac{\partial u}{\partial x} + \rho\, v\, \frac{\partial u}{\partial r} = \frac{1}{r}\, \frac{\partial}{\partial r}\, (r\mu_t\, \frac{\partial u}{\partial r})$$ X - momentum

8 unknowns, 8 equations

$\tilde{u}$ $from\ x - mom\ eqn$
$\tilde{v}$ $from\ continuity\ eqn$
$\bar{Z} = \bar{f}$ $from\ \bar{f}\ eqn = \bar{Z}\ eqn$
$\tilde{g} = \widetilde{f'^2} = variance\ of\ f$
k $from\ k - eqn$
ε $from\ epsilon\ eqn$
$\bar{\rho}$ $from\ state\ relation$
$p = constant, assumed$

$$\rho u\, \frac{\partial \bar{f}}{\partial x} + \rho v\, \frac{\partial \bar{f}}{\partial r} = \frac{1}{r}\, \frac{\partial}{\partial r}(r\, \frac{\mu_t}{\sigma_f}\, \frac{\partial \bar{f}}{\partial r})$$ f - eqn

$$\rho u\, \frac{\partial k}{\partial x} + \rho v\, \frac{\partial k}{\partial r} = \frac{1}{r}\, \frac{\partial}{\partial r}\left(r\, \frac{\mu_t}{\sigma_k}\, \frac{\partial k}{\partial r}\right) + \mu_t\left(\frac{\partial u}{\partial y}\right)^2$$

$$-C_D\, \frac{\rho^2 k^2}{\mu_t} + g\, C_\rho\, \frac{\mu_t}{\sigma_\rho}\, \frac{\partial \rho}{\partial x}$$ k equation

15

$$\rho u\, \frac{\partial \epsilon}{\partial x} + \rho v\, \frac{\partial \epsilon}{\partial y} = \frac{1}{r}\, \frac{\partial}{\partial r}\, r\, \frac{\mu_t}{\sigma_\epsilon}\, \frac{\partial \epsilon}{\partial r}$$ epsilon equation

$$+ C_{\epsilon_1}\, C_D\, \rho k\left(\frac{\partial u}{\partial y}\right)^2 - \frac{C_{\epsilon_2}}{C_D}\, \rho\, \frac{\epsilon^2}{k}$$

$$\rho u\, \frac{\partial g}{\partial x} + \rho v\, \frac{\partial g}{\partial r} = \frac{1}{r}\, \frac{\partial}{\partial r}\left(\frac{r\mu_t}{\sigma_g}\, \frac{\partial g}{\partial r}\right)$$ g – equation

$$+ C_{g_1}\, \mu_t\, (\frac{\partial \bar{f}}{\partial y})^2 - \frac{C_{g_2}}{C_D}\, \rho\epsilon g$$

$$\mu_t = C_D\, \rho\, \frac{k^2}{\epsilon}$$ Turbulent viscosity

Lockwood assumes unstrained
Laminar flamelets

16

Closure = only need to solve eqn for mean mixture fraction Z, use lookup tables
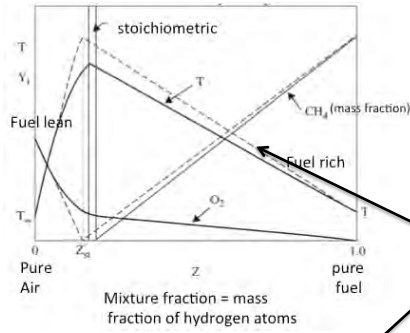
Dotted lines = State relation from CHEMKIN for laminar unstrained (very low strain rate) flame

T(Z) = dotted line

$$\overline{T} = \left(\bar{Z}, \overline{Z'^2}\right) = \int_0^1 T(Z) \; P\left(Z, \bar{Z}, \overline{Z'^2}\right) dZ$$

Note: no scalar dissipation rate appears for unstrained flamelets

17

RANS solutions – Lockwood and Naguib, Comb Flame 24, 109

Mean Velocity On jet centerline

Mixture fraction On jet centerline

Mean gas temperature On jet centerline

k/U^2
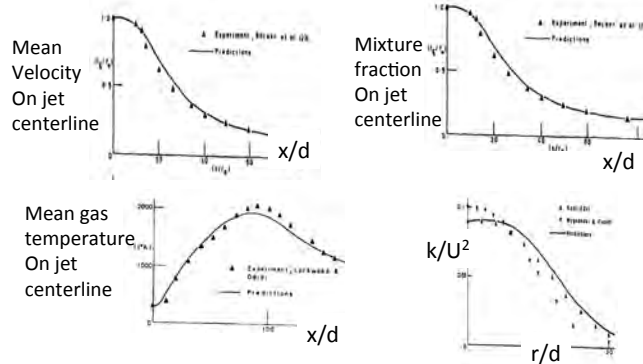
Problem – need to add **strained** flamelets = scalar dissipation rate To correctly predict temperature, NOx, CO

18

9

Non-premixed flames - add strained flamelets - Peters

Flamelet lookup tables –
solve strained
counterflow flame

Scalar
Dissipation
rate

$$\chi = 2\,D\,\left[\overline{\left(\frac{\partial Z}{\partial x}\right)^2} + \overline{\left(\frac{\partial Z}{\partial y}\right)^2} + \overline{\left(\frac{\partial Z}{\partial z}\right)^2}\right]$$
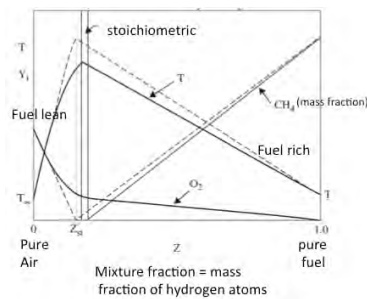
Solid lines = state relations = CHEMKIN
solutions to the **strained** flamelet
equations with complex chemistry

Two variables are mixture fraction and
scalar dissipation rate

stoichiometric

T

Y$_i$

T

Fuel lean

CH$_4$ (mass fraction)

Fuel rich

T$_\infty$

O$_2$

T

0   Z$_{st}$ Z   1.0

Pure
Air

pure
fuel

Mixture fraction = mass
fraction of hydrogen atoms

19

Counter flow non-premixed flame (Peters)

Air

flame

x

Fuel
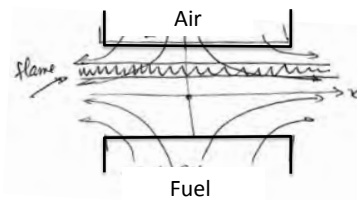
Assume:

Laminar flow, fast chemistry
For simplicity, assume constant density
Velocity not disturbed by heat release
All species diffuse at same diffusivity D
Lewis number = 1, D = constant
Scalars only vary in the y (vertical) direction

$$\frac{\partial u}{\partial x} + \frac{\partial v}{\partial y} = 0 \quad \text{So: } u = \varepsilon\,x \ ; \ v = -\varepsilon\,y$$

$$\rho\,u\,\frac{dZ}{dx} + \rho\,v\,\frac{dZ}{dy} = \rho\,D\,\frac{d^2 Z}{dy^2} \quad \text{so}$$

$$(\varepsilon\,x)\,[0] + (-\varepsilon\,y)\,\frac{dZ}{dy} = D\,\frac{d^2 Z}{dy^2}$$

$$so: \quad (-\varepsilon\,y)\,\frac{dZ}{dy} = D\,\frac{d^2 Z}{dy^2}$$

b.c.: y = oo, Z = 0, y = -oo, Z = 1

20

10

Solution to this equation is:

$$Z(y) = \frac{1}{2} - \frac{1}{2}\, \text{erf}\left(\frac{y}{\sqrt{2D/\epsilon}}\right)$$

Scalar dissipation rate:

$$\chi = 2D\left[\overline{\left(\frac{\partial Z}{\partial x}\right)^2} + \overline{\left(\frac{\partial Z}{\partial y}\right)^2} + \overline{\left(\frac{\partial Z}{\partial z}\right)^2}\right]$$

y — Flame is at Z = Zs = 0.06 — Z(y)

y — Flame is at Z =Zs = 0.06 — Z(y)

y — at Flame $\chi = \chi_s$ — χ (y)
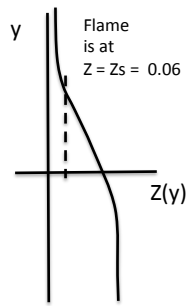
For low strain rate ε
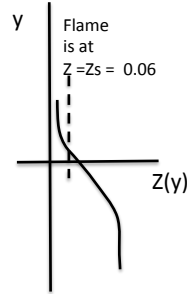
For high strain rate ε
Larger gradient
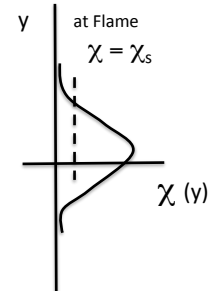
χ_s = constant · ε

21

What is flame location $(y = y_f)$?   In solution for Z, set Z = Z_s and solve for y

$$y_f = \sqrt{\frac{2D}{\varepsilon}}\; \text{erf}^{-1}\,(1 - 2Z_s)$$ Flame location

Flame location:

Increasing D   → y_f increases

Increasing ε or f_s → y_f decreases

22

11

Strength of a strained non-premixed counterflow flame

Strength of a non-premixed flame = mass flux of fuel at flame boundary

$\qquad$ = J_F = mass of fuel consumed /sec per unit flame area

$$J_F = -\rho_F\, D\, \frac{\partial Y_F}{\partial y} \qquad Ficke's\ Law$$

Use our state relation that says that Y_F is proportional to Z on the fuel side of flame

Take the derivative of the erf function formula for Z(y)

Plug in our formula for y = y_f at the flame front to get:

$$J_F = \rho_F\, D^{1/2}\, \varepsilon^{1/2} \cdot constant$$

Stronger flame if strain rate ε is made larger and ε is Proportional to χ_{st}

23

How is scalar dissipation rate χ_s related to strain rate ε ?

Define scalar dissipation rate for this counter flow geometry

$$\chi = 2\,D\left[\overline{\left(\frac{\partial Z}{\partial y}\right)^2}\right]$$

Take the derivative of our erf function for Z(y) and

Plug into this formula, and plug in y = our formula for y_f at flame surface, to get:

$$\chi_s = \varepsilon\, A \qquad where: \quad A = 4\,Z_s^2\,[erfc^{-1}(2\,Z_s)]^2$$

So the scalar gradient is related to velocity gradient

24

What is the thickness (δ_f) of a strained non-premixed flame ?

Define the thickness of a non-premixed flame to be:

$$\delta_f = \left(\frac{\partial Z}{\partial y}\right)^{-1}_{y=yf}$$
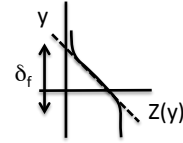
Take the derivative of our erf function for Z(y) and plug in our formula for y_f to get:

$$\delta_f = \sqrt{\frac{2D}{\chi_s}}$$

Flame gets thinner as you apply more strain

Example: if D = 1.0 cm^2/s = gas diffusivity near flame

if dissipation rate χ_s = 100 s^{-1}

Then flame thickness: δ_f = 1.4 mm

25

Flamelet assumption - of Peters adds **strain** to allow deviations from equilibrium chemistry
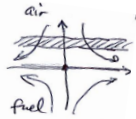
instantaneous T, Y_i are related to mixture fraction and dissipation rate in a turbulent flame in the same way they are related in a laminar counterflow flame with full chemistry

Steady non-premixed strained flamelet equation:

$$\rho \frac{\partial Y_i}{\partial t} = \frac{1}{2} \rho \chi \frac{\partial^2 Y_i}{\partial f^2} + \dot{\omega}_i \qquad \bar{\chi}_s = C_x \left(\frac{\epsilon g}{k}\right)$$

Solution yields state relations for all mass fractions, temperature, density as functions of Mixture fraction and Scalar dissipation rate

Now plug state relations into this to get mean values of temperature, density, mass fractions

$$\bar{Y}_{CO}\left(\bar{Z}, \overline{Z'^2}, \bar{\chi}, \overline{\chi'^2}\right) = \int_0^1 Y_{CO}(Z,\chi) \ P_1\left(Z, \bar{Z}, \overline{Z'^2}\right) P_2\left(\chi, \bar{\chi}, \overline{\chi'^2}\right) d\chi \ dZ$$

26

State relations - for a **strained** non-premixed counter flow laminar flamelet

temperature

Dissipation rate χ_s = 25 s^{-1}, 50 s^{-1}, 100 s^{-1}

Mixture fraction Z

Y_{CO}

Dissipation rate χ_s = 25 s^{-1}, 50 s^{-1}, 100 s^{-1}

Mixture fraction Z
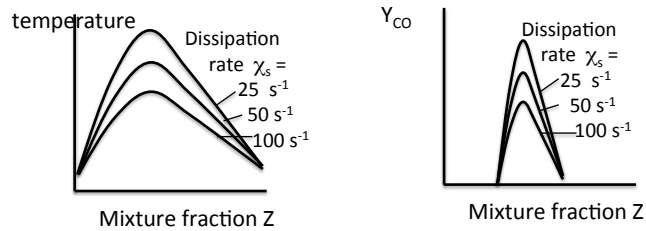
Generate plots above using CHEMKIN counter flow non-premixed flame solver

Larger velocity gradient (strain rate) = larger scalar gradient (scalar dissipation rate)

Larger dissipation rate → lowers the peak temperature,
alters the mass fractions of the species
reduces the chemical reaction rate until extinction occurs
improves prediction of CO, temperature, etc.

27

SSLF = Steady strained laminar flamelet LES model
of Sandia Flame D by Janicka

Investigation of length scales, scalar dissipation, and flame orientation in a piloted diffusion flame by LES, A. Kempf J. Janicka PROCI 30 557

Mixture fraction (Z) conservation eqn

$$\bar{\rho}\,\tilde{u}\,\frac{d\bar{Z}}{dx} + \bar{\rho}\,\tilde{v}\,\frac{d\bar{Z}}{dy} = \bar{\rho}\,D\,\frac{d^2\bar{Z}}{dy^2}$$

State relations from solutions to steady counter flow flamlet eqn
Mean mix fraction in subgrid = prop. to resolved scale gradients of Z
Variance of subgrid dissip. rate = prop. to resolved scale gradients
Assume a Beta function for P(Z), log-normal for P(χ). Mean quantities from:

LES of Sandia flame D

$$\bar{Y}_{CO}\left(\bar{Z},\overline{Z'^2},\bar{\chi},\overline{\chi'^2}\right) = \int_0^1 Y_{CO}(Z,\chi)\ P_1(Z,\bar{Z},\overline{Z'^2})\,P_2(\chi,\bar{\chi},\overline{\chi'^2})\,d\chi\,dZ$$

state relation   PDF

28

Janicka closure - for strained laminar flamelets

PDF of mixture fraction = Beta function, has mean and variance at each point
PDF of scalar dissipation rate = log normal shape, has mean and variance
At each (x,y,z) location we must compute the mean and variance of Z and χ

Mean mixture fraction - from Z conservation equation
Variance of mixture fraction - from "g" equation for scalar fluctuations

Mean scalar dissipation rate – assumed to be proportional to epsilon (dissipation rate
of turbulent kinetic energy), multiplied by the variance of mixture fraction

$$\bar{\chi}_{st} = \sigma_x \quad \varepsilon \quad \overline{Z'^2} / k$$

σ_x is a constant, k and ε come from the k and ε equations,

Variance of dissipation rate - assumed to be zero in FLUENT, others use an assumed
algebraic equation

29

Janicka - SLF steady laminar flamelet model of Sandia Jet Flame D, PROCI 30 557

30

15

Janicka   SLF LES, continued

PDF of scalar dissipation rate
Computed = bars
Measured = dots
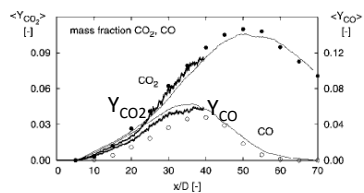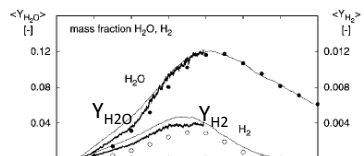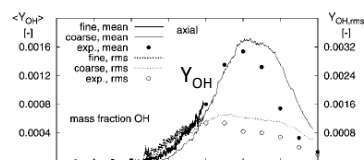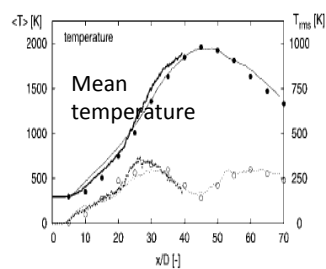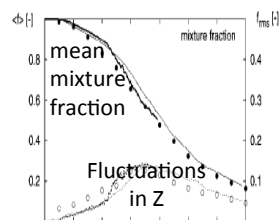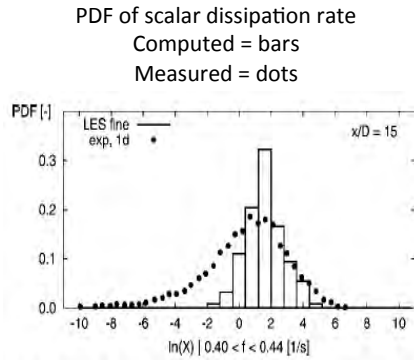
Conclude: the steady laminar
flamelet LES adequately simulates

the non-premixed combustion
 in Sandia jet flame D

except for H2 and CO on the fuel
rich side – it is a little off

PDF [·]

LES fine —
exp, 1d •

x/D = 15

0.3

0.2

0.1

0.0

-10 -8 -6 -4 -2 0 2 4 6 8 10

ln(X) | 0.40 < f < 0.44 [1/s]

Fig. 9. The PDF of the resolved scalar dissipation rate.
This quantity is expected to be log-normally distributed.
Comparison of LES-data (1d) to experimental 1d-data.

31

Flamelet progress variable (FPV-LES) model   – compared to Barlow's
measurements in a non-premixed jet flame

C. Hasse,   "LES flamelet-progress variable modeling and measurements
of a turbulent partially-premixed dimethyl ether jet flame" Comb Flame 162, 3016

$$\frac{\partial}{\partial t}(\bar{\rho}\,\tilde{Z}) + \nabla \cdot (\bar{\rho}\,\tilde{\mathbf{u}}\,\tilde{Z}) = \nabla \cdot \left[\left(\bar{\rho}\,D_Z + \frac{\mu_t}{Sc_t} \right) \nabla \tilde{Z} \right]$$

$$\widetilde{Z''^2} = C_{\widetilde{Z''^2}}\,\Delta^2\,|\nabla\tilde{Z}|^2$$

**Replace scalar dissipation rate with a
new progress variable Y_c**

Progress variable: $Y_c = Y_{H2} + Y_{H2O} + Y_{CO} + Y_{CO2}$

$$\frac{\partial}{\partial t}(\bar{\rho}\,\tilde{Y}_C) + \nabla \cdot (\bar{\rho}\,\tilde{\mathbf{u}}\,\tilde{Y}_C) = \nabla \cdot \left[\left(\bar{\rho}\,D_{Y_C} + \frac{\mu_t}{Sc_t} \right) \nabla \tilde{Y}_C \right] + \overline{\dot{\omega}}_{Y_C}$$

A presumed β-shaped filtered density function (FDF) is used to
integrate the mixture fraction, and a δ-FDF is applied for the nor-
malized progress variable to account for non-resolved fluctuations.
Using a δ-FDF means that no subgrid closure is employed for the
normalized progress variable. For the integration process, the nor-

OH
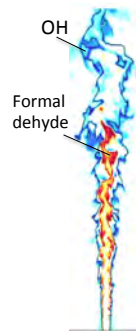
Formal
dehyde

LES of
Hasse

Experiment
Sandia flame D

32

16

Slide 33

LES – FPV model of Hasse (Frieberg) agrees with Sandia measurements

mean Temperature   temp fluctuations

mean CO   mean CO_2

Expt = dotted
Model = solid
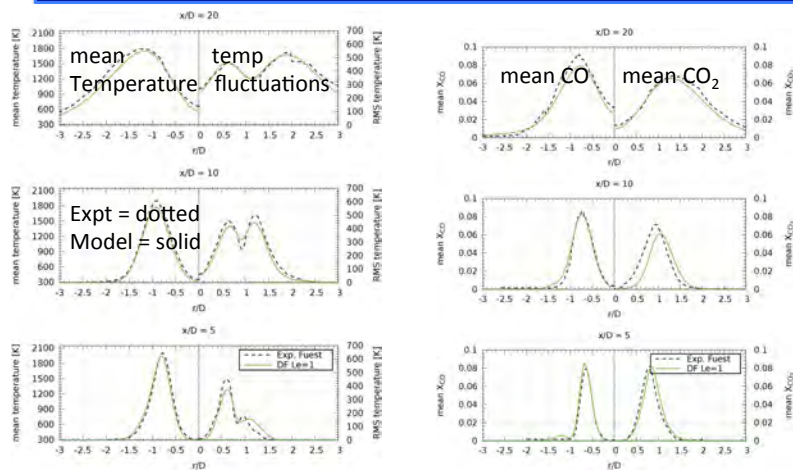
Conclude: the Flamelet Progress Variable (FPV)model gives good agreement with measurements for major species and CO. NO was not attempted

33

Slide 34

Good Measurements –
           of non-premixed turbulent combustion

See TNF website http://www.sandia.gov/TNF/

Single point Raman/Rayleigh/LIF data for f, T, N2, O2, CH4, CO2, H2O, H2, CO, OH, NO and velocity

Barlow, R. S., Frank, J. H., A. N. Karpetis, and Chen, J.-Y.,
 "Piloted Methane/Air Jet Flames: Scalar Structure and
Transport Effects," Combust. Flame 143:433-449 (2005).

Masri, A., Dibble, R.,Barlow, R., Structure of Turbulent
 Nonpremixed Flames Revealed by Raman-Rayleigh-LIF
 Measurements', Prog. Energy Combust. Sci., 22:307-362 (1997).

34

Barlow: Non-premixed piloted jet flame
in Comb Flame 143, 433 and

TNF website http://www.sandia.gov/TNF/
"Piloted methane/air jet flames: Transport effects and aspects of scalar structure"

Single point   Raman/Rayleigh/LIF measurements of
f, T, N2, O2, CH4, CO2, H2O, H2, CO, OH, NO, velocity,
line Raman for scalar dissipation rate:

$$\chi = 2D\left[\overline{\left(\frac{\partial Z}{\partial x}\right)^2} + \overline{\left(\frac{\partial Z}{\partial y}\right)^2} + \overline{\left(\frac{\partial Z}{\partial z}\right)^2}\right]$$

Lasers for Raman, Rayleigh: Nd:YAG at 532 nm
Lasers for LIF = Nd:YAG + dye: 282 nm for OH, 226 nm
For NO, 230 nm for CO (two photon)

Spatial resolution = 0.75 mm
Fluorescence signals were corrected for Boltzmann
fraction and collisional quenching rate

Sandia flame D
Jet diam. = 7.2 mm
Pilot dia = 18.2 mm
Jet U = 50 m/s
Coflow U = 0.9 m/s

35

Barlow: Non-premixed jet flame

in Comb Flame 143, 433

Fig. 1. Measured conditional means of species mass fractions (symbols) compared with laminar opposed-flow flame calculations including full molecular transport (dashed lines) or equal diffusivities (solid lines). Measurements are shown for (a) flame B at $x/d = 15$ and (b) flame E at $x/d = 45$.

Data points = turbulent jet flame,

Agree w steady laminar counterflow
CHEMKIN = state relations computed
for strain parameter $2 U_{oo}/R = 50$ s^{-1}

Conclude: steady flamelet state relations
- Adequate for CO & major species
- Not adequate for H$_2$ or NO
- Differential diffusion is negligible
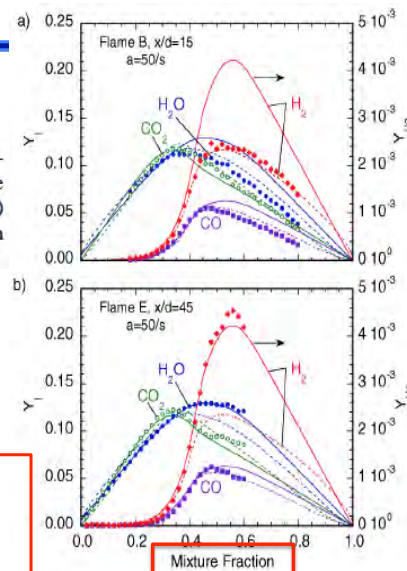
36

More Barlow measurements in turbulent non-premixed jet flames

PDF of mixture fraction
is a Beta function

Max NO
is near
stochiometric

Scalar
Diss rate

Mixture Fraction
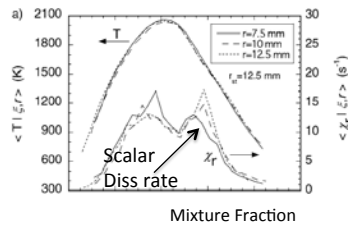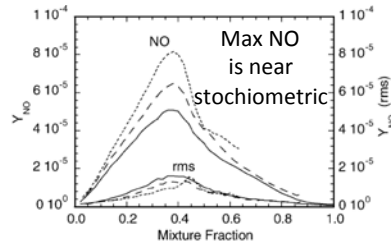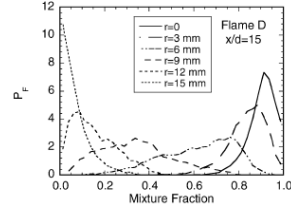
Barlow concludes: all important single point properties were measured in 5 piloted jet non-premixed flames, to be used to assess models

37

Nitric Oxide - predicted by FPV model compared to non-premixed jet experiment of Barlow

Ihme and Pitsch use FPV to predict NOx in jet flame and in a Pratt gas turbine

FPV model
experiment
(other models)
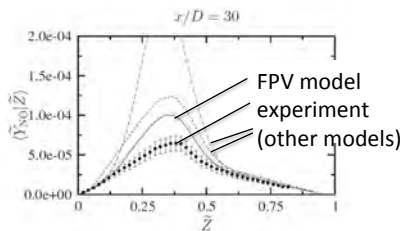
Flamelet progress variable LES overpredicts NO by 40% in a simple jet flame. Not too bad They included radiative heat loss.

Ihme and Pitsch, Modeling of radiation and nitric oxide formation in turbulent non-pre
Mixed flames using a flamelet/progress variable formulation, Phys Fluids 20, 055110

38

19

NO can be predicted with post-processing (easy)

(c) Averaged temperature (normalized)

(d) Averaged NO mole fraction (normalized)
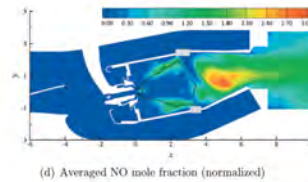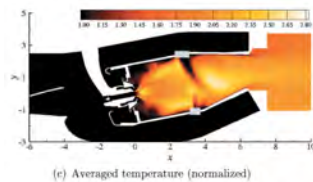
LES to compute temperature, Y_{N2} and Y_{O2} fields (means and variances)

NO is formed on long time scale so

$$\rho \mathcal{D}_t Y_{NO} = \nabla \cdot (\rho \alpha \nabla Y_{NO}) + \rho \dot{\omega}_{NO}.$$

$O + N_2 \leftrightarrow NO + N$ etc.
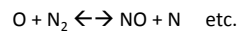
State relation for ω_{NO} obtained from laminar flamelet eqn

$$\bar{\rho} \widetilde{\mathcal{D}}_t \widetilde{Y}_{NO} = \nabla \cdot (\bar{\rho} \widetilde{\alpha} \nabla \widetilde{Y}_{NO}) + \nabla \cdot \overline{\tau}^{res}_{NO} + \bar{\rho} \widetilde{\dot{\omega}}_{NO},$$

We already know T, Y_O, Y_{N2} from resolved scale LES

Ihme and Pitsch, Modeling of radiation and nitric oxide formation in turbulent non-pre Mixed flames using a flamelet/progress variable formulation, Phys Fluids 20, 055110

39

A more complex problem: gas turbine-like swirl flame undergoing unsteady oscillations

Steinberg, A, , Meier, W. et al., Effects of Flow Structure Dynamics on Thermoacoustic Instabilities in Swirl-Stabilized Combustion, AIAA J. 50, p. 952.
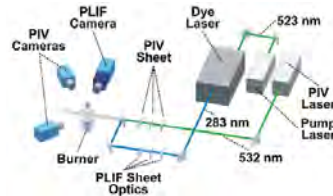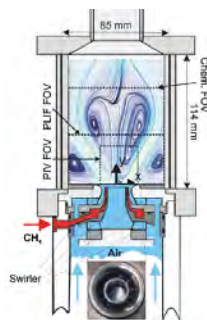
5 kHz PLIF/PIV system

40
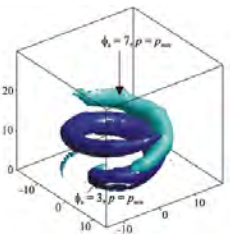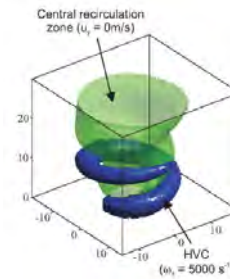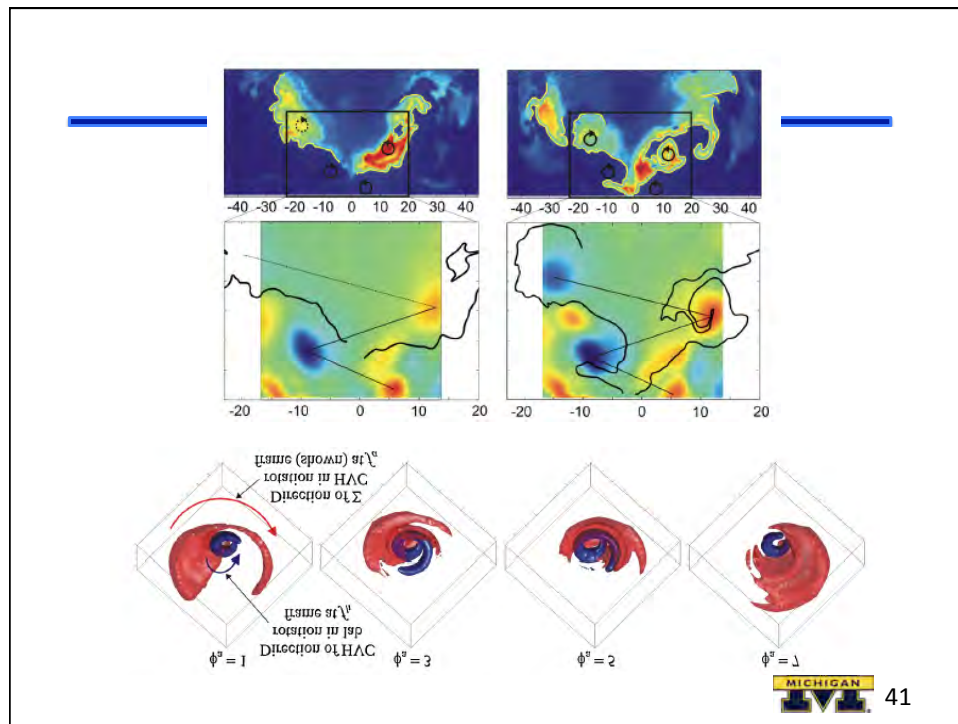
What is the goal of comparing model results to experiments ?

Many models with very different assumptions all "agree" with measurements

Is there any point in comparing output of models without assessing the basic assumptions in the model; i.e., do thin strained flamelets occur in the expt ?

If models agree to within 5%, is there any point to work for better agreement ?

Do we need to include heat losses, complex chemistry, acoustics, pressure ?

Are computations really independent of b.c.s, initial condition, grid size ?

Is the goal to identify the "best" model, or can we live with 20 models ?

How useful are models that do not solve the Navier Stokes eqns ? Some replace NS with Langevin eqn, ad-hoc mixing models, etc. ?

42

How are we doing ?   How well are we making measurements
and how well do models compare ?

Review of some good papers - in turbulent combustion

Barlow, R. S., Frank, J. H., A. N. Karpetis, and Chen, J.-Y., "Piloted Methane/Air Jet
Flames: Scalar Structure and Transport Effects," Combust. Flame 143:433-449 (2005)

C. Hasse,   "LES flamelet-progress variable modeling and measurements
of a turbulent partially-premixed dimethyl ether jet flame" Comb Flame 162, 3016

Steinberg, A, , Meier, W. et al., Effects of Flow Structure Dynamics on Thermoacoustic
Instabilities in Swirl-Stabilized Combustion, AIAA J. 50, p. 952.

43

How well can we model premixed turbulent flames ?

Bray / FSD model

Assume thin or thickened
wrinkled flamelets

fully premixed or
stratified premixed,
FSD model is being modified
to handle
partially-premixed

considers
corregated (pockets)
flamelet merging
stretch rate increases area

Gas temperature

Mean temperature

Σ = FSD
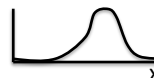
Masuya, Bray, Comb Sci Tech 25, 127

44

Laminar Premixed Flame Theory

first we review laminar theory and see how it can be modified to include turbulence

$T(x) \sim c(x)$

reaction

preheat

x

$x = x_i$

$\dot{x} = -\infty$
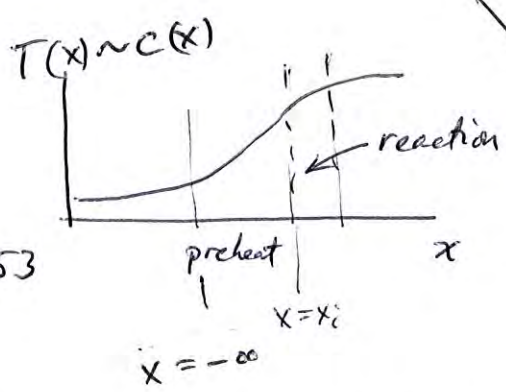
Kuo 2nd Eq. Eq^n 5-21, p. 453

$$\rho u \frac{d\theta}{dx} = \rho \alpha \frac{d^2\theta}{dx^2} + \dot{w} \qquad (Kuo\ 5\text{-}21)$$

where $\theta \equiv \dfrac{T-T_R}{(Q/c_p)}$; if we define reactedness $c \equiv \dfrac{T-T_R}{T_P - T_R}$

but $T_P - T_R = Q/c_p$

so $\theta = c$

$$\boxed{\rho u \frac{dc}{dx} = \rho \alpha \frac{d^2 c}{dx^2} + \dot{w}}$$ reactedness ODE for laminar flame

$\underbrace{\dfrac{\text{Convection of heat}}{c_p (T_P - T_R)}}$ = $\underbrace{\dfrac{\text{diffusion of heat}}{c_p (T_P - T_R)}}$ + $\underbrace{\dfrac{\text{heat liberated}}{c_p (T_P - T_R)}} \leftarrow (Q/c_p)$

integrate this eqn over the preheat zone $x = \infty$ to $x = x_i$

$\rho u = \rho_R S_L$ (cons. mass) $\rho \alpha = \rho \frac{\lambda}{\rho c_p}$

get $(\rho u) \displaystyle\int_{-\infty}^{x_i} \frac{dc}{dx} dx = \rho \alpha \int_{-\infty}^{x_i} \frac{d}{dx}\left(\frac{dc}{dx}\right) dx + \int_{-\infty}^{x_i} \dot{w}\, dx$

no reactions in preheat zone!

$(\rho_R S_L)(c_i - c_{-\infty}) = \dfrac{\lambda}{c_p}\left(\dfrac{dc}{dx}\Big|_{x_i} - \dfrac{dc}{dx}\Big|_{-\infty}\right) + 0$

$\rho_R S_L \left(\dfrac{T_i - T_R}{T_P - T_R} - 0\right) = \dfrac{\lambda}{c_p}\left(\left(\dfrac{T_F - T_i}{T_P - T_i}\right)\dfrac{1}{\delta_R} - 0\right) + 0$

$\therefore \boxed{\rho_R S_L (T_i - T_R)\cdot c_p = \lambda (T_F - T_i)/\delta_R}$

theory of Mallard + Le Chatlier (Kuo 5-8)

3-21

2.1 Thermal Theory: Mallard and LeChatelier's Development[2] (1883)

The objective of laminar-flame theory is to find the laminar-flame speed S_L. The temperature variation across the flame can be plotted as shown in Fig. 5.7. Mallard and LeChatelier divided the flame into two zones. Zone I is the preheat zone, in which the gases are heated by conduction and reach ignition at the
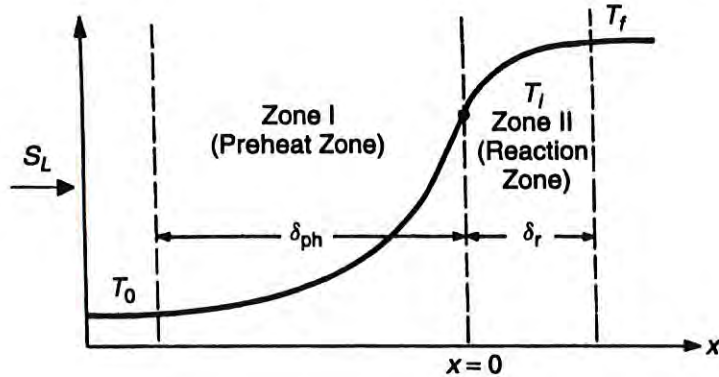

Figure 5.7 Schematic diagram of the temperature variation across a typical laminar flame.

ignition boundary. Zone II is the chemical reaction zone, in which chemical enthalpy is converted into sensible enthalpy.

The energy balance of zone I gives

preheat zone *(RR=0)*

$$\dot{S_L}\rho C_p(T_i - T_0) = \lambda \frac{T_f - T_i}{\delta_r} \qquad \text{or} \qquad S_L = \frac{\lambda}{\rho C_p}\frac{T_f - T_i}{T_i - T_0}\frac{1}{\delta_r} \qquad (5\text{-}8)$$

convection diffusion

where the left-hand side of the equation represents the amount of energy absorbed as the unburned mixture flows into the entrance of the preheat zone at T_0 and is heated to T_i at the exit of the preheat zone, and the right-hand side is the heat flux to the interface. The value of S_L can be determined from Eq. (5-8), if the reaction zone thickness δ_r is known. Let's define τ_r to be the reaction time; then

NO use

$$\delta_r = S_L \tau_r = S_L \frac{1}{d\varepsilon/dt} \qquad \text{or} \qquad \delta_r \propto S_L \frac{1}{RR} \qquad (5\text{-}9)$$

where ε is the reaction-progress variable discussed in Chapter 1 and $d\varepsilon/dt$ is the rate of reaction (RR). Substituting Eq. (5-9) into Eq. (5-8), we get

$$S_L = \sqrt{\left(\frac{\lambda}{\rho C_p}\right)\frac{T_f - T_i}{T_i - T_0}\left(\frac{d\varepsilon}{dt}\right)} \propto \sqrt{\alpha \cdot RR} \qquad (5\text{-}10)$$

but don't know what T to use for RR!

where T_i represents the ignition temperature. Mallard and LeChatelier did not specify the specific temperature at which the reaction rate RR should be determined. However, their analysis suggests that the flame speed is proportional to the square root of the product of thermal diffusivity and reaction rate. This result is one of the most important relationships in laminar-flame theories.

For the pressure dependence, we have

$$S_L \propto \sqrt{\frac{1}{\rho} p^{n-1}} \propto \sqrt{p^{n-2}} \tag{5-12}$$

This equation implies that for second-order chemical reactions, the laminar-flame speed should be independent of pressure. Based on Eq. (5-10) and the Arrhenius law for RR, the temperature dependence can be expressed:

$$S_L \propto \sqrt{e^{-E_a/R_u T}} = e^{-E_a/2R_u T} \tag{5-13}$$

As we shall see later, in order to obtain realistic values of S_L, one needs to replace the temperature T in Eq. (5-13) by T_f, since most chemical reaction takes place around T_f.

2.2 Comprehensive Theory: The Theory of Zel'dovich, Frank-Kamenetsky, and Semenov

These investigators have adopted Mallard and LeChatelier's idea[2,3] of dividing the flame into two zones (preheat and reaction zones). However, instead of considering the energy equation alone, they have used the species-conservation equation together with the energy equation. They propose that the ignition temperature is very close to the adiabatic flame temperature and consequently replace T_i with T_f in their estimation of reaction rates. Their basic assumptions are as follows:

(a) The pressure is constant.
(b) The number of moles does not vary during the reaction. This restriction is later removed to allow the number to change in the mole ratio

$$\frac{n_r}{n_p} \equiv \frac{\text{moles of reactant}}{\text{moles of product}}$$

according to the stoichiometric reaction.
(c) C_p and λ are constant.
(d) $\lambda/C_p = \mathcal{D}\rho$. This implies that Le $= 1$, and has the effect of reducing the number of differential equations from two to one by replacing one of the differential equations with an algebraic equation. Later this restriction is modified to allow Le $=$ constant.
(e) The flame is one-dimensional and steady-state.

The equations of species continuity and energy conservation are first written in their most general forms and then simplified according to the above assumptions:

452   PREMIXED LAMINAR FLAMES

The general species conservation equation derived in Chapter 3 can be written as

$$\frac{\partial \rho_r}{\partial t} + \nabla \cdot \rho_r \mathbf{v} = \nabla \cdot (\rho \mathcal{D} \nabla Y_r) - \dot{\omega}_r \qquad (5\text{-}14)$$

$\dot{\omega}_r$ is positive for rate of destruction of reactants, and $\dot{\omega}_r$ has the dimension of $M t^{-1} L^{-3}$. Under assumption (e), Eq. (5-14) becomes

$$\frac{d}{dx}\left(\frac{\rho_r}{\rho}\cdot \rho u\right) = \frac{d}{dx}\left[\rho \mathcal{D}\frac{d}{dx}\left(\frac{\rho_r}{\rho}\right)\right] - \dot{\omega}_r$$

or

$$\frac{\rho_r}{\rho}\frac{d(\rho u)}{dx} + \rho u \frac{d(\rho_r/\rho)}{dx} = \rho \mathcal{D}\frac{d^2}{dx^2}\left(\frac{\rho_r}{\rho}\right) - \dot{\omega}_r \qquad (5\text{-}14a)$$

From continuity equation $d(\rho u)/dx = 0$, Eq. (5-14a) becomes

$$\rho u \frac{d(\rho_r/\rho)}{dx} = \rho \mathcal{D}\frac{d^2}{dx^2}\left(\frac{\rho_r}{\rho}\right) - \dot{\omega}_r \qquad (5\text{-}14b)$$

ρ_r can be written in terms of the number density a of reactant molecules (molecules/m^3) as

$$\rho_r = \frac{a}{N_A}\cdot Mw_r \qquad (5\text{-}15)$$

where N_A is Avogadro's number, and Mw_r is the reactant molecular weight (g/mole or kg/kmol). Equation (5-14b) then becomes

$$\rho u \frac{d(aMw_r/\rho N_A)}{dx} = \rho \mathcal{D}\frac{d^2}{dx^2}(aMw_r/\rho N_A) - \dot{\omega}_r \qquad (5\text{-}14c)$$

Multiplying through by N_A/Mw_r and rearranging the terms, we have

$$\rho \mathcal{D}\frac{d^2(a/\rho)}{dx^2} - \rho u \frac{d(a/\rho)}{dx} - \dot{\omega} = 0 \qquad (5\text{-}16)$$

The inhomogeneous term in Eq. (5-16) is denoted by $\dot{\omega} \equiv N_A \cdot \dot{\omega}_r/Mw_r$, which represents the rate of change of the number of molecules of reactant per unit volume by chemical reaction. The first term of the species equation represents the rate of mass diffusion of reactant species and the second term the rate of mass convection of reactant species.

From Chapter 3 we have learned that the general form of the energy equation in terms of enthalpy is

$$\rho \frac{Dh}{Dt} - \frac{Dp}{Dt} = -\nabla \cdot \mathbf{q} + \Phi + \dot{Q} + \rho \sum_{K=1}^{N} Y_K \mathbf{f}_K \cdot \mathbf{v}_K \qquad (3\text{-}78)$$

$\dot{\omega} = \dfrac{\text{molecules reactant/sec}}{\text{vol}} = \text{positive}$

Neglecting

we have th

or

where $\dot{Q} =$
of reactant)

where the
Followi
ables θ and

where the
tuting Eqs

These two
The bo
$x = -\infty$

For $x = +$

Neglecting dissipation, body-force work, and unsteady terms, and also using

$$q = -\lambda \frac{dT}{dx}, \qquad h = C_p T$$

we have the following energy equation in one-dimensional form:

$$\rho C_p u \frac{dT}{dx} = \lambda \frac{d^2 T}{dx^2} + \dot{Q}$$

or

$$\frac{\lambda}{\rho C_p} \frac{d^2 T}{dx^2} = u \frac{dT}{dx} - \frac{\dot{Q}}{\rho C_p} \tag{5-17}$$

where $\dot{Q} = -\sum_{i=1}^{N} \dot{\omega}_i \Delta h^o_{f,i} = \dot{\omega} Q$ (Q represents the heat of reaction per molecule of reactant). Equation (5-17) can be written as

$$\frac{\lambda}{C_p} \frac{d^2 T}{dx^2} - \rho u \frac{dT}{dx} + \frac{\dot{\omega} Q}{C_p} = 0 \tag{5-18}$$

where the product ρu is the eigenvalue of the problem.

Following the Shvab–Zel'dovich formulation (see Chapter 3), two new variables θ and α are defined as

$$\theta \equiv C_p \frac{T - T_0}{Q} \quad \rightarrow dimensional \quad molecules/kg \tag{5-19}$$

$$\alpha \equiv \frac{a_0}{\rho_0} - \frac{a}{\rho} \tag{5-20}$$

where the subscript 0 designates initial values at an undisturbed station. Substituting Eqs. (5-19) and (5-20) into Eqs. (5-18) and (5-16), we have

nondimensional temperature rises across flame

$$\boxed{\frac{\lambda}{C_p} \frac{d^2\theta}{dx^2} - \rho u \frac{d\theta}{dx} + \dot{\omega} = 0} \tag{5-21}$$

$$\rho \mathcal{D} \frac{d^2\alpha}{dx^2} - \rho u \frac{d\alpha}{dx} + \dot{\omega} = 0 \tag{5-22}$$

These two equations are identical if Le $= 1$.

The boundary conditions for (5-21) and (5-22) are prescribed as follows: For $x = -\infty$ (cold boundary),

$$\alpha = 0, \qquad \theta = 0$$

For $x = +\infty$ (hot boundary),

$$\alpha = \frac{a_0}{\rho_0}, \qquad \theta = C_p \frac{T_f - T_0}{Q}$$

3-25
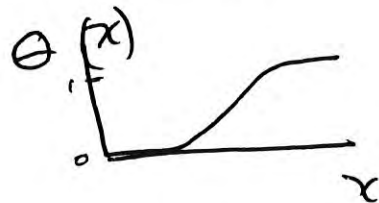
Theory of Stretched Laminar Premixed Flames
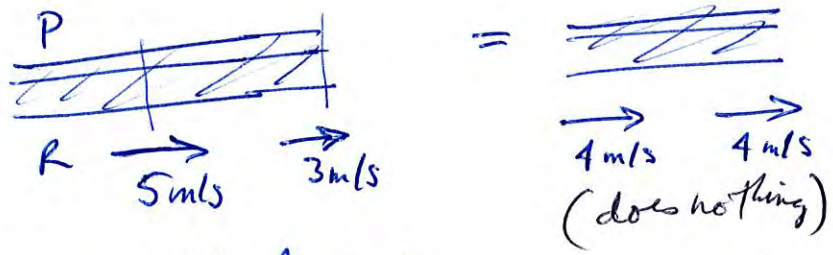
read Cpt 1 in CTOOLS

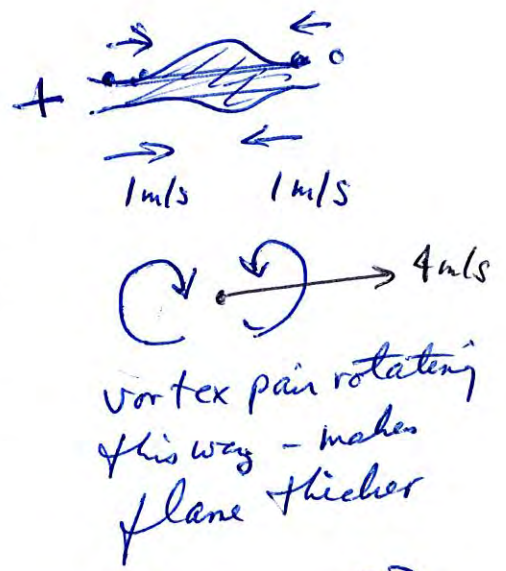- laminar flame <u>not</u> affected by a superimposed <u>constant</u> tangential velocity
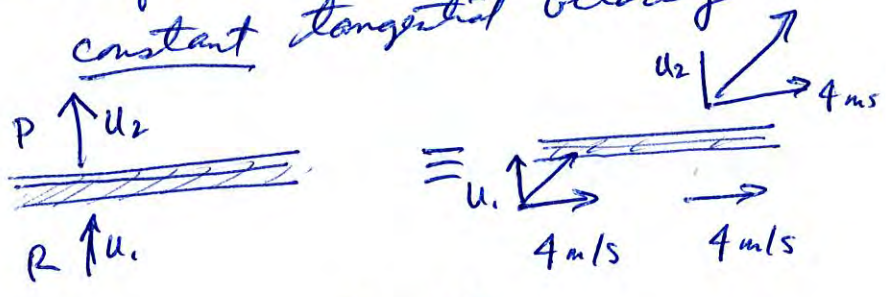
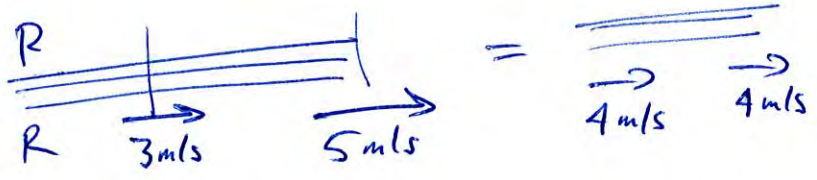- is affected by a <u>tangential velocity gradient</u>

a)

tang. velocity decreases in direction of tang. velocity
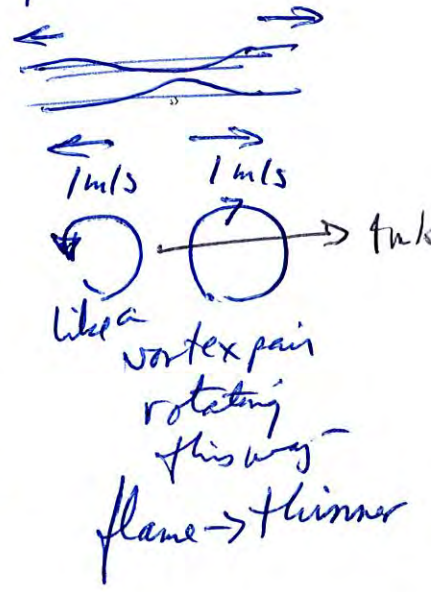
= compressive strain -

vortex pair rotating this way - makes flame thicker

b)

tang. velocity increases in direction of tang. velocity.

= extensive strain - elongates + thins flame

like a vortex pair rotating this way - flame → thinner

1-11

Strain rate (on flame ~~example~~)

$$K_S \equiv \begin{array}{c} \text{strain} \\ \text{rate on} \\ \text{flame} \end{array} = \bar{\nabla}\cdot\bar{V} - \bar{n}\cdot(\bar{n}\cdot\bar{\nabla})\bar{V} \qquad \bigg]_{\substack{\text{at} \\ \text{upstream boundary} \\ \text{of flame, in} \\ \text{reactants}}}$$

ex. counterflow premixed flame

- assume reactants = constant density = ρ_R
  products = " " = ρ_P

←FLAME
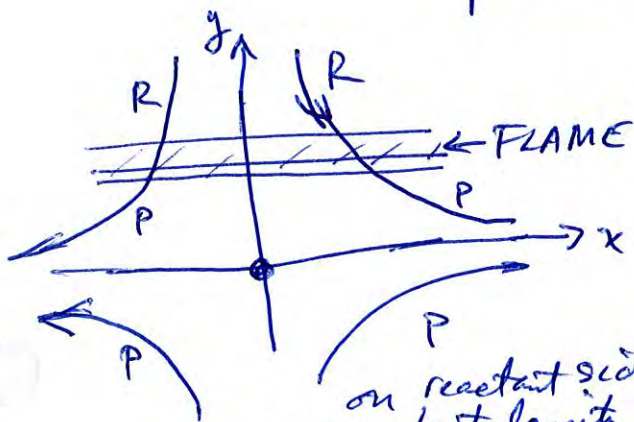
in reactants, assume:

$$\bar{V} = (\epsilon x)\,\bar{\imath} - (\epsilon y)\,\bar{\jmath}$$

$\underbrace{}_{u} \qquad \underbrace{}_{v}$

$\epsilon = \begin{array}{c}\text{aerodynamic} \\ \text{strain rate} \\ \text{in reactants}\end{array} = $ constant

note:

on reactant side:
constant density,
mass is conserved

flow is irrotational

streamlines are hyperbolas
on reactant side

$$\frac{\partial u}{\partial x} + \frac{\partial v}{\partial y} = 0 \qquad \Rightarrow \epsilon + (-\epsilon) = 0$$

$$\frac{\partial v}{\partial x} - \frac{\partial u}{\partial y} = 0 \qquad \qquad 0 + 0 = 0$$

$$\bar{n} = \bar{\jmath}$$

$$K_S = ? \quad = \bar{\nabla}\cdot\bar{V} - \bar{n}\cdot(\bar{n}\cdot\bar{\nabla})\bar{V}$$

$$= \underbrace{\left(\frac{\partial u}{\partial x} + \frac{\partial v}{\partial y}\right)}_{0} - \bar{\jmath}\cdot\left(\frac{\partial}{\partial y}\right)\left(\underbrace{u\bar{\imath}}_{\bar{\jmath}\cdot\bar{\imath}=0} + v\,\bar{\jmath}\right)$$

$\overset{(\epsilon x)}{} \quad \overset{(\epsilon y)}{}$

$$\boxed{K_S = -\frac{\partial v}{\partial y}}$$

$$\therefore \boxed{K_S = \epsilon}$$

strain rate is a velocity
gradient, since
$$v = -\epsilon y \quad \text{then}$$

1-12

$$\boxed{\text{flame curvature} = (\bar{\nabla} \cdot \bar{n}) = 1/R_c}$$

$\bar{n}$ = normal to flame pointing toward reactants

cyl. flame $\quad \bar{n} = \bar{e}_r$

$$\bar{\nabla} \cdot \bar{n} = \frac{\partial}{\partial r}(\bar{e}_r)$$

R_c = radius of curvature $\Rightarrow$ for cylinder of radius R $\quad R_c = R$

for a sphere of radius R $\quad R_c = \frac{R}{2}$

— sphere has twice the curvature of cylinder of same radius

curvature, $R_c = +$ if flame is convex toward reactants:

outward prop.

" $\quad - \quad$ " " concave "

Stretch rate of flame surface (K)

$$K = \frac{1}{A}\frac{dA}{dt} \qquad A = \text{flame area}$$

Candel* uses geometry to show

$$\boxed{K = K_s + K_c}$$

$$\boxed{\begin{aligned} K_s &= \frac{\text{strain}}{\text{rate}} = \bar{\nabla} \cdot \bar{v} - \bar{n} \cdot (\bar{n} \cdot \bar{\nabla}\bar{v}) \\ K_c &= \begin{array}{l}\text{curvature} \\ \text{component} \\ \text{to stretch}\end{array} = \frac{S_L}{R_c} \end{aligned}}$$

(CST 70, 1, 1990)

1-13

_ex._ outward propagating flame of radius R_F

$$A = 4\pi R_F^2$$

$$K = \frac{1}{A}\frac{dA}{dt} = \frac{1}{4\pi R_F^2}(4\pi)\left(2R_F\frac{dR_F}{dt}\right)$$

$$K = \frac{2}{R_F}\frac{dR_F}{dt} = +$$

this flame has positive stretch rate K
since its area is increasing in time

— Homework: compute K_s and K_c and see that
they add up to the above value of K

_ex._ for HW show

curvature $\nabla \cdot \bar{n} = R_F^{-1}$ for cylindrical flame of rad. R_F

$\qquad\qquad = 2R_F^{-1}$ for spherical flame of rad R_F

1—17

Observation

propagation speed of laminar flames increases or decreases depending on stretch rate, type of fuel

S_L = stretched laminar burning velocity

S_{L0} = unstretched laminar burning velocity

observed that

$$\boxed{\dfrac{S_L}{S_{L0}} = 1 - Ka\, Ma}$$

for small values of Ka

Ka = Karlovitz No. = $\dfrac{\text{non dim.}}{\text{stretch rate}}$ = $\dfrac{K \nwarrow^{K_s + K_e}}{(S_{L0}^2 / \alpha_o)}$

α_o = thermal diffusivity of reactants

Ma = Markstein number measured to be
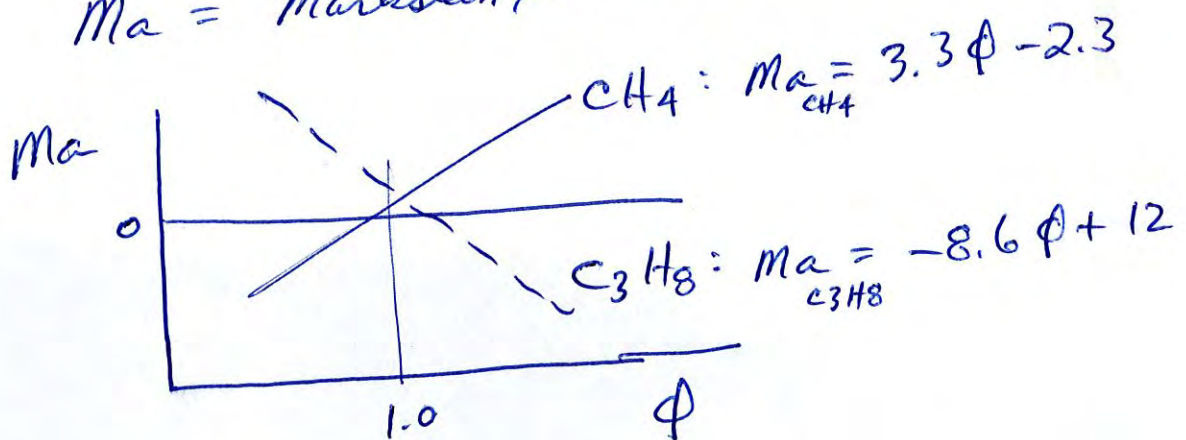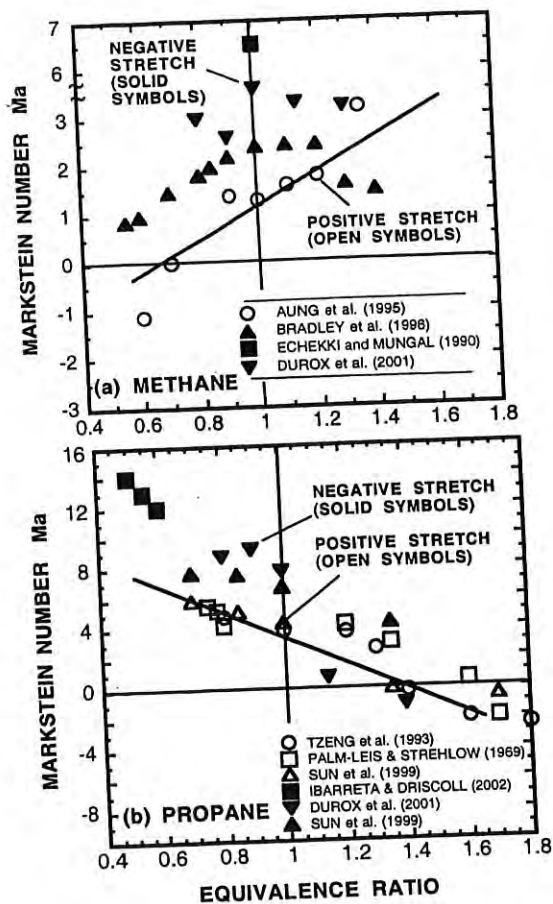
$CH_4 : Ma_{CH4} = 3.3\phi - 2.3$

$C_3H_8 : Ma_{C3H8} = -8.6\phi + 12$

Fig. 1. Markstein numbers measured and computed by previous investigators, showing that larger values of Ma occur for cases of negative stretch. a) methane-air; b) propane-air; reactants at 300 K, 1 atm.

Propagation speeds and stretch rates measured along wrinkled flames to assess the theory of flame stretch

Jose O. Sinibaldi[a], James F. Driscoll[a,*], Charles J. Mueller[b], Jeffrey M. Donbar[c], Campbell D. Carter[c]

[a]Department of Aerospace Engineering, University of Michigan, Ann Arbor, MI 48109, USA
[b]Combustion Research, Sandia National Labs, Livermore CA USA
[c]AFRL/PRAS, Wright-Patterson Air Force Base, OH 45433 USA

1-16

Lewis number   (Do for HW)

Some authors use Lewis number instead of Markstein number

$$Ma = \frac{1 - Le^{-1}}{(+ \; constant)} \leftarrow \text{from expt}$$

$$Le \equiv \frac{\alpha_R}{D_{DR}} = \frac{\text{thermal diff. of reactant mixture}}{\text{mass diffusivity of the deficient reactant}}$$

$\phi < 1$ fuel lean   — defic. reactant is fuel

$\phi > 1$ fuel rich — def. reactant is air

ex. lean Methane - air

$$\alpha_R \simeq \alpha_{AIR}$$

$$D_{DR} = D_{CH4} > D_{air} > \alpha_{AR}$$

so $Le \not< 1$

$$Ma \sim 1 - Le^{-1} < 0$$

negative

thermodiffusively

$Ma = 0$	$Le = 1$	neutral
$Ma = +$	$Le > 1$	stable
$Ma = -$	$Le < 1$	unstable

(lean H_2 = wrinkled)

1-17

	lean CH4 $(Ma = neg)$	rich CH4 $Ma = pos$
Stretch rate, Ka are $+$	$S_L > S_{LO}$ (accelerated)	$S_L < S_{LO}$ (slowed)
stretch rate, Ka are $-$	$S_L < S_{LO}$ (slowed)	$S_L > S_{LO}$ (accelerated)

for propane - trends are opposite those of methane

propane diffusivity $<$ air

methane " $>$ air

observe: tip of bunsen burner can be open (small S_L)

or closed (large S_L)

P

R

closed,
bright
tip

rich methane or
lean propane

open, extinguished
tip

lean methane or
rich propane
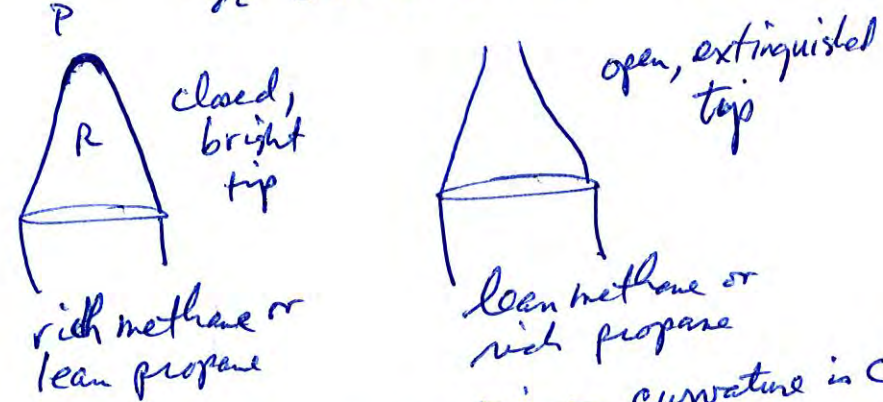
bunsen tip $Ka = $ negative $\Rightarrow$ curvature is concave
toward reactants

if rich methane $Ma = +$

$$(S_L / S_{LO}) = 1 - \underset{-}{Ka} \cdot \underset{+}{Ma} = >1 \ !$$

bright
tip !

1-16

Hypothesis (theory of flame stretch)

— all laminar + turbulent premixed flame segments obey "in flamelet regime"

$$\boxed{S_L / S_{L0} = 1 - Ka \cdot Ma}$$

— not valid if turbulence so intense — not in flamelet regime
— not valid if turbulence begins to extinguish flame
— is a good "theoretical" concept

Valid for

a) laminar bunsen flame tip (open or closed) K_c curvature = −
K_s strain ≈ 0

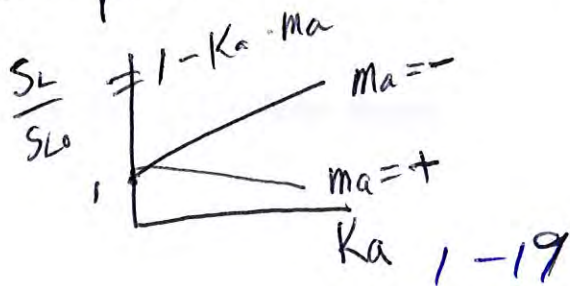b) laminar counterflow flames (premixed) K_c curvature = 0
K_s strain = +
twin flame expt:
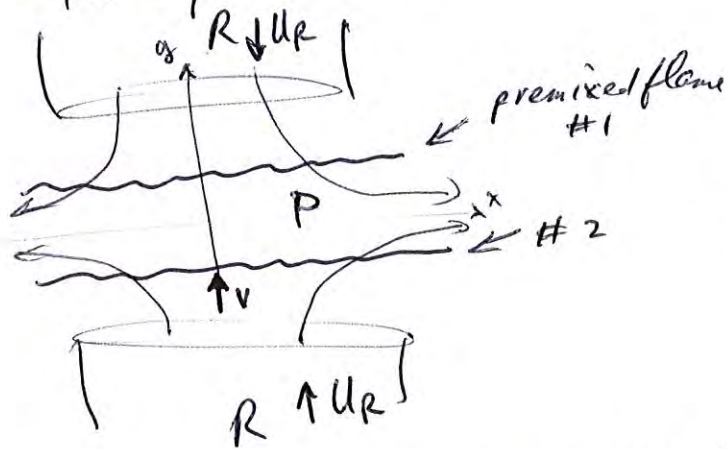
$K = K_s + K_c$
(stretch rate)

← premixed flame #1
← #2

could replace x axis with wall, but have heat transfer issues

since flame #2 is steady, measure v velocity just ahead of it = S

$$\frac{S_L}{S_{L0}} \neq 1 - Ka \cdot Ma$$

$Ka \sim U_R$

$ma = -$
$ma = +$

Ka

1 −19

Theory of Flame Stretch — Chung & Law CNF 72, 325, 1988.

Consider counterflow premixed flame; and a planar unstretched flame:

unstretched planar case: heat diffuses upstream, fuel diffuses downstream nothing leaves along sides of CV

stretched case: heat diffuses upstream in middle to the preheat zone but some heat diffuses out curved sides of CV

✗ assume fuel = deficient reactant = fuel-lean $\phi < 1$

some fuel will diffuse downstream into CV across curved sides

if 1 kg/sec fuel diffuses in → $44,000 \frac{kJ}{sec}$ extra heat liberated

heat diffusing out of CV — tends to reduce S_L

deficient reactant diffusing into CV — tends to increase S_L

why — reaction zone sees mixture that is closer to stoichiometric

1—20

Physical idea

— Stretch (= velocity gradients and/or curvature)
curves the streamlines w.r.t the flame surface

— causes "leakage" of heat — so of heat
generated by reaction zone does not make it
into the preheat zone — leakage + or neg. dep. on curvature
(deficient reactant, fuel if fuel lean)

— leakage ~~of fuel~~ also possible — counteracts
leakage of heat

α = thermal diff. of mixture

$D_{deficient} = D_F$ = mass diffus. of deficient reactant

$$\boxed{Le \equiv \frac{\alpha}{D_{deficient}}}$$ Lewis No.

T_{AD} = ad. flame temp. of unstretched flame

T_b = burned temp of stretched flame chemical

If $Le = 1$, heat lost thru side walls $\approx$ heat gained from fuel enthalpy

if $Le > 1$ $\alpha > D_F$ more heat lost than gained, fuel enthalpy $T_b < T_{AD}$ for stretch rate $(K) > 0$

$Le < 1$ $\alpha < D_F$ less heat lost then gained $T_b > T_{AD}$
                              — for $K > 0$ positive stretch

Theory of Flame Stretch — premixed flames

read on Canvas   Kuo — flame stretch
                   Law — flame stretch

define $K = $ stretch rate $= \dfrac{1}{A_f} \dfrac{dA_f}{dt}$ $A_f = $ flame area

$$\boxed{K = K_s + K_c}$$

$K_s = $ strain rate component of stretch rate

$K_c = $ curvature component of stretch rate

$$\boxed{\begin{aligned} K_s &= \left[\nabla \cdot \bar{v} - \bar{n} \cdot (\bar{n} \cdot \bar{\nabla})\bar{v}\right]_{LE} \\ K_c &= S_L (\bar{\nabla} \cdot \bar{n}) = S_L / R_c \end{aligned}}$$

(Cardel, Comb. SciTech. 70, 1, 1990)

$\bar{n} = $ normal to flame surface pointing to reactants

$\bar{v} = $ velocity of gas

$S_L = $ laminar burning velocity

$R_c = $ radius of curvature of flame surface

$LE = $ leading edge

ex   reactants / products

spherical outward propagating laminar premixed flame

$A_f = 4\pi R_f^2$ $R_f(t) = $ flame radius

stretch rate $K = \dfrac{1}{A_f} \dfrac{dA_f}{dt} = \dfrac{1}{4\pi R_f^2} \, 4\pi \, 2 R_f \dfrac{dR_f}{dt} = \dfrac{2}{R_f}\dfrac{dR_f}{dt}$

stretch rate is <u>positive</u> for this flame

note: $\bar{\nabla} \cdot \bar{n} = R_f^{-1}$ for cylindrical flame, $= 2R_f^{-1}$ for spherical flame

6-1

ex. steady counter flow laminar premixed flame
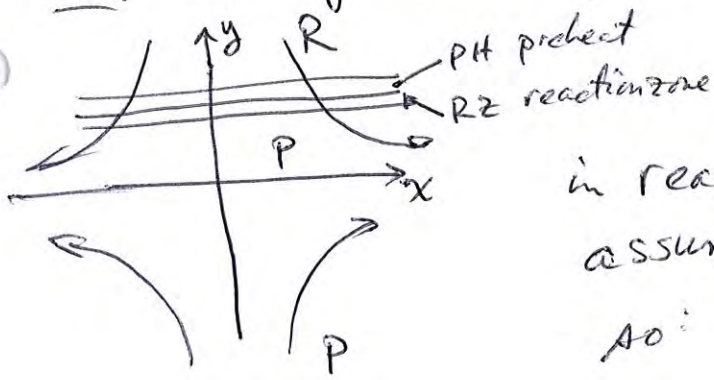
in reactants, at leading edge (LE)
assume incompressible cold reactants

so: $\bar{\nabla} \cdot \bar{V} \big|_{LE} = 0$

$\bar{V} = \underbrace{(\epsilon x)}_{u} \bar{\imath} + \underbrace{(-\epsilon y)}_{\upsilon} \bar{\jmath}$, $\bar{n} = \bar{\jmath}$

(note: $\frac{\partial u}{\partial x} + \frac{\partial \upsilon}{\partial y} = 0$)
streamlines are
hyperbolas

$\epsilon =$ aerodynamic strain rate (s^{-1})

$K_s = \bar{\nabla} \cdot \bar{V} - \bar{n} \cdot (\bar{n} \cdot \bar{\nabla}) \bar{V} \big|_{LE}$

$= \underbrace{\left(\frac{\partial u}{\partial x} + \frac{\partial \upsilon}{\partial y} \right)}_{\epsilon \quad -\epsilon}^{>0} - \bar{\jmath} \cdot \left(\bar{\jmath} \cdot \bar{\jmath} \frac{\partial}{\partial y} \right) \left(\epsilon x \bar{\imath} - \epsilon y \bar{\jmath} \right)$

$\boxed{K_s = \epsilon} = \boxed{- \frac{\partial \upsilon}{\partial y} \Big|_{LE}} = \boxed{+ \frac{\partial u}{\partial x} \Big|_{LE}}$

u increases in X = strain is positive
rate

$K_c = S_L \bar{\nabla} \cdot \bar{n} = S_L / R_c = 0$
no flame
curvature component
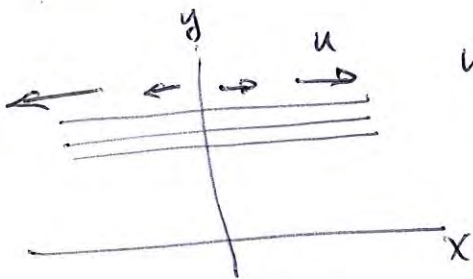
so $\boxed{K = K_s = \epsilon}$

turbulent flame hypothesis

each segment of a turbulent flame has a value of K stretch rate, where

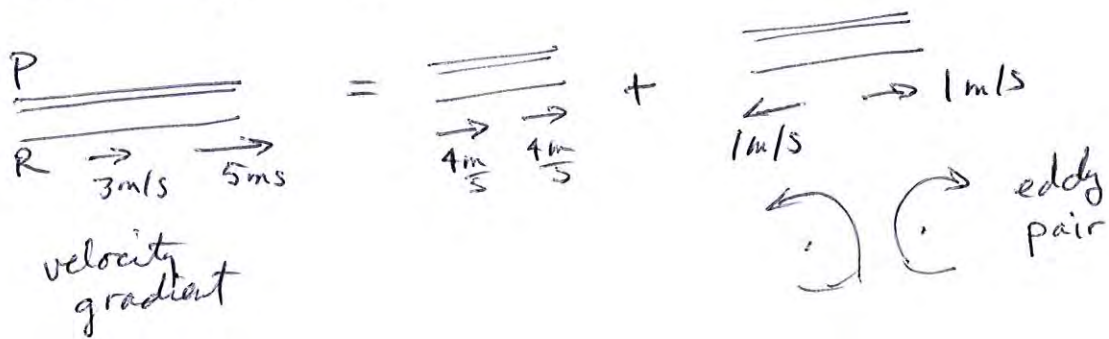$$K = K_s + K_c \qquad \text{strain, curvature components}$$

Hypothesis #1: flame speed (S_L) and internal structure of two laminar flames are identical if they have the same stretch rate K

(and same fuel type, equivalence ratio, T_R, P) even if one flame has only strain (i.e. counter flow, $K_c = 0$) and the other has only curvature $K_s = 0$)

Hypothesis #2: a segment of a turbulent flame, shown above) has the same flame speed and internal structure as a laminar flame of the same stretch rate (K) (for same fuel, oxidizer, ER, T_R, P).

Conclude: do experiments to measure S_L, structure of counter flow premixed steady laminar flames

eddies exert strain:

$$\underset{\substack{R \; \underset{3m/s}{\rightarrow} \quad \underset{5ms}{\rightarrow}}}{\overset{P}{=\!=\!=\!=\!=}} = \underset{\underset{4\frac{m}{s}}{\rightarrow} \; \underset{4\frac{m}{s}}{\rightarrow}}{=\!=\!=} + \underset{\substack{\underset{1m/s}{\leftarrow} \quad \underset{}{\rightarrow} 1m/s}}{=\!=\!=}$$

velocity gradient

eddy pair

6 – 3

Karlovitz number $\boxed{Ka = K/(S_{LO}^2/\alpha)}$

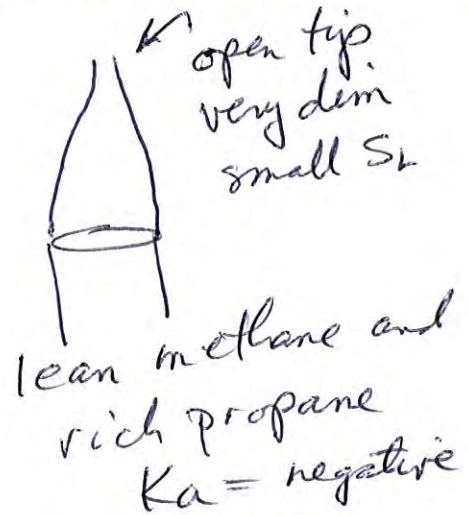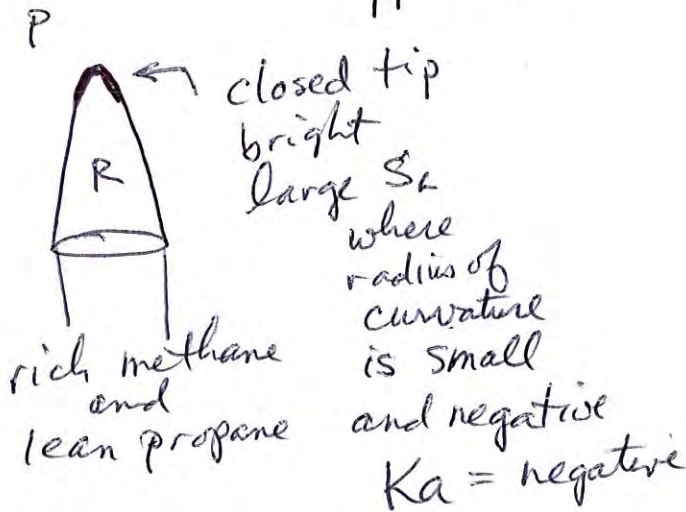K = stretch rate $\qquad S_{LO}$ = unstretched laminar burning velocity

α = thermal diffusivity (molecular) $= 0.15 \frac{cm^2}{s}$ at 300 K

$S_{LO}^2/\alpha = s^{-1}$ = reaction rate

$Ka = \dfrac{\text{stretch rate}}{\text{reaction rate}}$ = nondim. stretch rate

Observe $\quad$ laminar stretched burning velocity (S_L)
differs from unstretched burning velocity (S_{LO})

P

closed tip
bright
large S_L
where
radius of
curvature
is small
and negative
Ka = negative

R

rich methane
and
lean propane

open tip
very dim
small S_L

lean methane and
rich propane
Ka = negative

conclude

$$\boxed{\dfrac{S_L}{S_{L,0}} = 1 - Ka \cdot Ma}$$

Ma = Markstein number
depends on fuel and
equivalence ratio

6-4

$Ka = -$ for bunsen tip

$\boxed{Ma = + \text{ for rich methane}}$

$\left(\dfrac{S_L}{S_{LO}} = 1 - (-) \cdot (-)\right)$

so $\dfrac{S_L}{S_{LO}} > 1$

$\boxed{Ma = - \text{ for lean methane}}$

What is the Markstein number Ma?

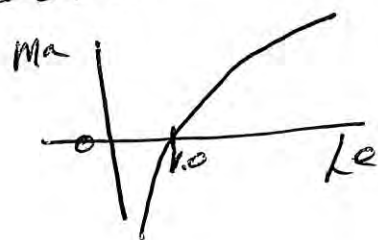Sung + Law, see CANVAS, paper shows that

$$Ma = \frac{1 - Le^{-1}}{c_1}$$

Le = lewis number
c_1 = some constant

$$Le = \frac{\alpha_R}{D_{DR}} = \frac{\text{thermal diffusivity of reactant mixture}}{\text{mass diffusivity of the deficient reactant}}$$

$$D_{DR} = D_{fuel} \quad \text{if fuel lean}$$
$$= D_{air} \quad \text{if fuel rich}$$

$$\frac{S_L}{S_{LO}} = 1 - Ka \, Ma$$

Markstein number given by
← from Sinibaldi, Driscoll Comb. Flame 133, 323,
shows rich methane → Ma = +
explains why tip is closed for rich methane

Fig. 1. Markstein numbers measured and computed by previous investigators, showing that larger values of Ma occur for cases of negative stretch. a) methane-air; b) propane-air; reactants at 300 K, 1 atm.

The figure contains two plots:

(a) METHANE — MARKSTEIN NUMBER Ma vs EQUIVALENCE RATIO
NEGATIVE STRETCH (SOLID SYMBOLS)
POSITIVE STRETCH (OPEN SYMBOLS)
- AUNG et al. (1995)
- BRADLEY et al. (1996)
- ECHEKKI and MUNGAL (1990)
- DUROX et al. (2001)

(b) PROPANE — MARKSTEIN NUMBER Ma vs EQUIVALENCE RATIO
NEGATIVE STRETCH (SOLID SYMBOLS)
POSITIVE STRETCH (OPEN SYMBOLS)
- TZENG et al. (1993)
- PALM-LEIS & STREHLOW (1969)
- SUN et al. (1999)
- IBARRETA & DRISCOLL (2002)
- DUROX et al. (2001)
- SUN et al. (1999)

EQUIVALENCE RATIO

6 - 5

Theory of Flame Stretch — Chung & Law CNF 72, 325, 1988.

consider counterflow premixed flame; and a planar unstretched flame:

unstretched planar case: heat diffuses upstream, fuel diffuses downstream
nothing leaves along sides of CV

stretched case: heat diffuses upstream in middle to the preheat zone
but some heat diffuses out curved sides of CV

☆ assume fuel = deficient reactant = fuel-lean $\phi < 1$

some fuel will diffuse downstream into CV across curved sides
if 1 kg/sec fuel diffuses in → 44,000 $\frac{kJ}{sec}$ extra heat liberated

heat diffusing out of CV — tends to reduce S_L

deficient reactant diffusing into CV — tends to increase S_L
why — reaction zone sees mixture that is
closer to stoichiometric

Physical Idea

— Stretch (= velocity gradients and/or curvature)
curves the streamlines wrt the flame surface

— causes "leakage" of heat — so of heat
generated by reaction zone does not make it
into the preheat zone — leakage + or neg. dep. on curvature
(deficient reactant, fuel if fuel lean)

— leakage ~~of fuel~~ also possible — counteracts
leakage of heat

α = thermal diff. of mixture

$D_{deficient} = D_F$ = mass diffus. of deficient reactant

$$\boxed{Le \equiv \frac{\alpha}{D_{deficient}}}$$ Lewis No.

T_{AD} = ad. flame temp. of unstretched flame

T_b = burned temp of stretched flame chemic

If $Le = 1$, heat lost thru side walls $\approx$ heat gained from fuel enthalpy

if $Le > 1$ $\alpha > D_F$ more heat lost than gained, fuel enthalpy $T_b < T_{AD}$
     fn stretch rate (K) > 0

$Le < 1$ $\alpha < D_F$ less heat lost than gained $T_b > T_{AD}$
     for K > 0 positive stretch

Law and Sung PECS 26, p. 159, (pp 470-472)

Prove that
$$S_L / S_{LO} = 1 - Ka \cdot Ma$$

S_L = laminar burning velocity of stretched flame, S_{LO} = unstretched

Ka = nondimensional stretch rate

(a) unstretched premixed flame
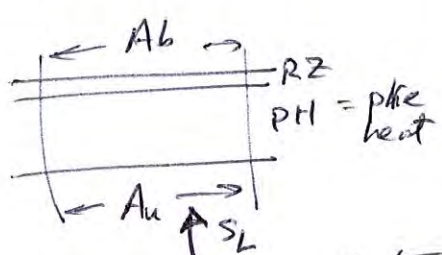
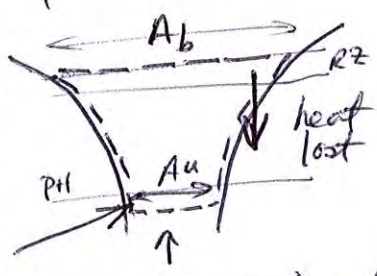
T_i = ignition T
T_u = unburned T
T_b = burned T

$q = \frac{kJ/kg}{reactant}$
δ_{RZ} = thickness of RZ

RZ
PH = preheat

Mallard LeChat. theory:

$$(\rho_u S_L A_u) c_P (T_i - T_u) = \frac{\lambda(T_i - T_u)}{\delta_T} A_u = (\rho_u RR) A_b \, \delta_{RZ} \, q$$

$\underbrace{}_{kJ/sec\ into\ preheat\ zone}$ $\underbrace{}_{kJ/sec\ diffusing\ out\ of\ RZ}$ $\underbrace{}_{kJ/sec\ produced\ in\ Reaction\ Zone}$

(b) consider a stretched flame: control volume

RZ
PH
A_u
heat lost

Law says:
[his Eq 45]

$$(\rho_u S_L A_u) c_P (T_i - T_u) = (\rho_u RR) A_b \, \delta_{RZ} \, q - \lambda \left(\frac{T_b - T_u}{\delta_T}\right)(A_b - A_u)$$

$\underbrace{}_{kJ/sec\ into\ preheat}$ $\underbrace{}_{kJ/sec\ produced}$ $\underbrace{}_{kJ/sec\ heat\ LOST\ through\ side\ walls}$

and

$$(\rho_u S_L A_u) Y_{DR} = \rho_u RR A_b \, \delta_{RZ} - \rho_u D_{DR}\left(\frac{Y_{DR}}{\delta_m}\right)(A_b - A_u)$$

$\underbrace{}_{kg/sec\ of\ deficient\ reactant\ gained\ by\ diffusion\ at\ side\ wall}$

inspection tells us:

$$Le = \frac{\alpha}{D_{DR}} = \frac{thermal\ diff = \frac{\lambda}{\rho_u c_P}}{mass\ diff.\ of\ deficient\ reactant}$$

$$Ka = (A_b - A_u)/A_u \qquad (Law\ Eq\ 51)\ are\ important$$
$$Ma = (1 - Le^{-1})/c_1 \qquad (Law\ Eq\ 54)\ also\ important$$

6-8

Thermo diffusive instability

observe lean hydrogen flames (laminar) automatically become cellular, which rich hydrogen does not

cellular flame — lean H_2

flat flame — rich H_2
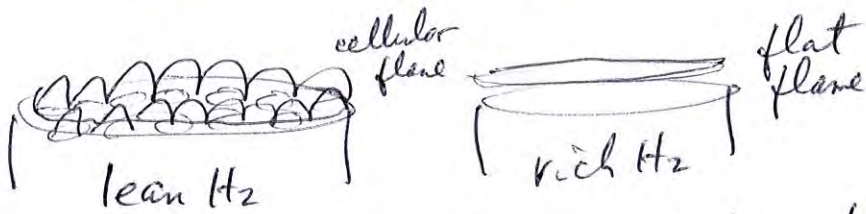
explanation: perturb a flat lean H_2 flame and the perturbation will grow in time (unstable)
perturb a flat rich H_2 flame and the perturbation will decay in time   WHY?

consider a lean H_2 flame — perturbed to be a sine wave

Prod.   P

R   ↑↑↑↑↑↑↑↑↑
         reactants
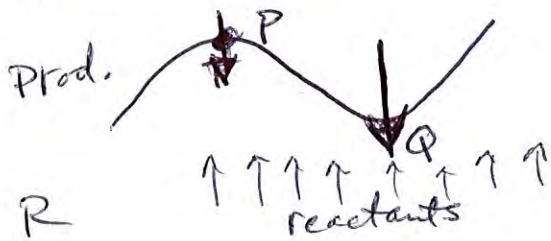
lean H_2 ⟹ Ma = negative

at P Ka = negative
at Q Ka = positive
         (like a spherical flame)

$$\frac{S_L}{S_{L0}} = 1 - Ka \, Ma$$ so
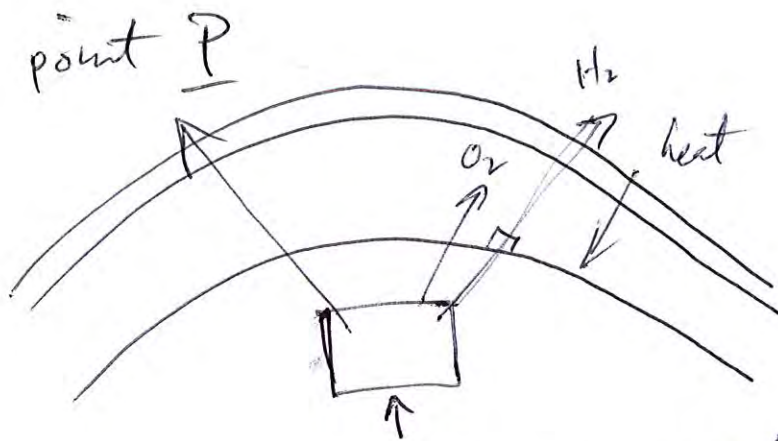
at P $S_L/S_{L0} = 1 - (-)(-) < 1$
at Q $S/S_{L0} = 1 - (+)(-) > 1$

stretch (curvature) causes P to propagate SLOWER
                      causes Q to propagate FASTER

so wrinkle will grow in time
[lean H_2 flame is T-D unstable]

$Ma = -$
$Le < 1$

6-9

Physical explanation of thermo diffusive instability

point P

as fluid element filled with lean H_2
approaches flame $\quad H_2 =$ deficient reactant

- hydrogen diffuses fast, radially outward as shown
  due to Fick's Law — down the H_2 gradient
  normal to flame contours

- so element becomes leaner and flame
  sees really lean reactants — very low
  flame speed at P

- point P is pushed downstream

$Le = \dfrac{\alpha}{D_{DF}}$ = small   — wrinkle grows in time

$\uparrow$ large O_2 also diffuses outward but not so fast
heat diffuses onward but not so fast
so dominate factor is H_2 diffusion

lean H_2, CH_4
(rich propane)

$\boxed{Le < 1 \quad \text{thermo diff. unstable}}$

6-10

Integral analysis of Law and Sung on CTOOLS

— on CTOOLS (Cheng + Law is not — too complicated to have both)

— note: $Ma°$ of Law is negative of normal Ma we use

Fig 8

un-burned

burned

l_R reaction zone thickness

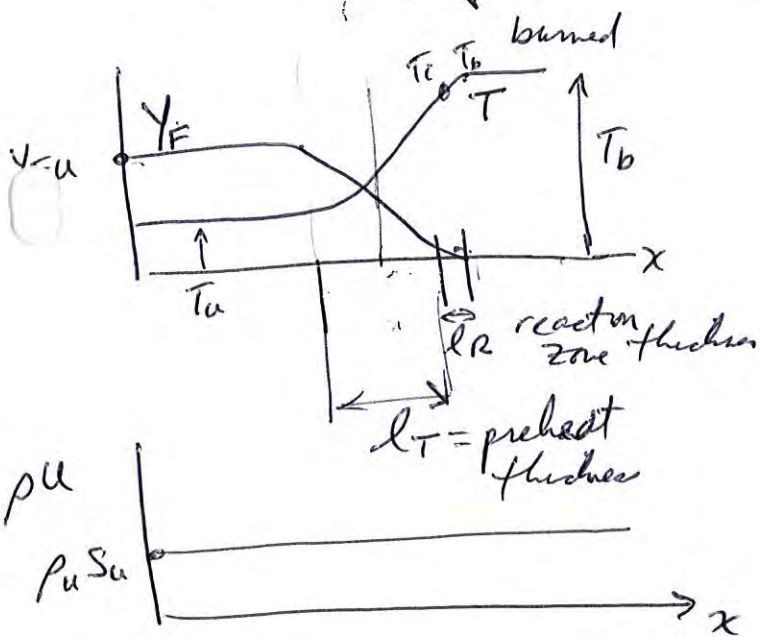$l_T = $ preheat thickness
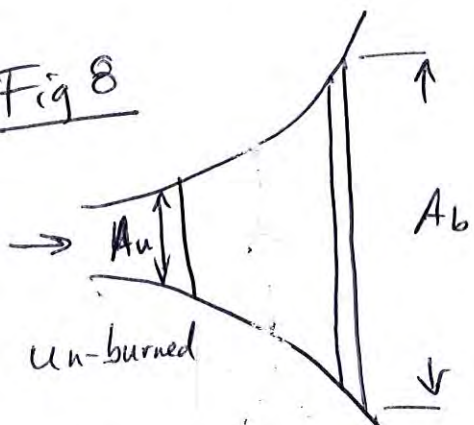
$f = \rho u$

$f_u = \rho_u S_{Lu}$

$S_{Lu} = S_L = $ stretched laminar burning velocity

(i) mass balance

$$\frac{d}{dx}(\rho U A) = 0$$

Law + Sung (39)

Law + Sung Eq (45a)

assume $T_i = T_B$

(ii) energy balance integrate over preheat zone,

$$m C_p (T_b - T_u) + \lambda \left.\frac{dT}{dx}\right|_{x_f} (A_b - A_u) = A_b \, q_c \, B_c \cdot \int_{x_f}^{x_f'} Y \cdot k \, dx$$

kg/s $\frac{kJ}{kgK}$ K

kJ/sec added to preheat zone

leakage of heat

kJ/sec created by reaction zone

1-22

$$m = \rho_u S_L A_u \quad \text{mass/sec}$$

$$q_c = kJ/kg \text{ fuel} = 119{,}000 \frac{kJ}{kg} \text{ fn } H_2, \ 45{,}000 \frac{kJ}{kg} \ CH_4$$

$$k = \text{Arrhenius factor} = \exp\left(-T_a/T\right)$$

B_c = pre exponential factor of reaction

Y = mass fraction of deficient reactant

Note: $\begin{cases} \text{planar flame} - \text{no stretch} \quad A_u = \quad A_b \\ \text{leakage } \wedge \text{ heat} = 0 \quad (A_b - A_u) = 0 \\ \text{reduces to Mallard-Le Chatlier integral analysis} \end{cases}$

(iii) species conservation for deficient reactant mass fraction (Y)

$$m Y + \rho D \left.\frac{dY}{dx}\right|_{x_f} (A_b - A_u) = - A_b B_c \int_{x_f}^{x_f'} Y k \, dx$$

Law + Sung Eq (45b)

(iv) set $\dfrac{A_b - A_u}{A_u} = Ka = \dfrac{K}{(S_L^2/\alpha)}$ $\quad$ stretch rate = $K_s + K_c$

Karlovitz No.

Law + Sung Eq (51)

proof:

define $K \equiv \dfrac{1}{A} \dfrac{dA}{dt} = \dfrac{1}{A_u} \dfrac{A_b - A_u}{\Delta t}$

$\Delta t = $ time for fluid to cross from A_u to A_b $= \dfrac{\delta_T}{S_L}$

$\delta_T = \dfrac{\alpha}{S_L}$ combine to get

$\left(\dfrac{A_b - A_u}{A_u} \right) = K \Delta t = \dfrac{K}{S_L^2 / \alpha} = Ka$

Law & Sung P. 471   combine Eqs (i) to (iv)

Eq 55:
Eq 58: $\tilde{S}_u \equiv \dfrac{S_L}{S_{L0}} = 1 + \sigma^0$

$\sigma^0 = Ma^0 \, Ka^0$
$(Eq 58)$

Law's Ma^0 is negative of normal Markstein number! $Ma^0 = -Ma$

$\therefore$ Eqns 55 + 58 $\Rightarrow$ $\boxed{\dfrac{S_L}{S_{L0}} = 1 - Ka \, Ma}$

Law also shows that stretch can lower the burned gas temperature locally –

1-24

Eq (54)
58

$$T_b = T_b^\circ + (T_b^\circ - T_u)\left(\frac{1}{Le} - 1\right) Ka^\circ$$

burned gas T with stretch

burned gas T with no stretch

Karlovitz non-dim stretch rate

idea: heat "leakage" across curved streamlines
can reduce final temperature locally
but fuel leakage into CV (for fuel lean conditions)
can raise final temperature, so result depends on Le

idea: same theory holds if streamlines are straight
but flame is curved

Bunsen tip — streamlines nearly straight,
curvature is negative   Ka < 0
same type of leakage occurs
(→ streamlines are curved wrt flame surface)

note — all of this applies for small stretch rates
— at large stretch rate — positive stretch
causes all flames to extinguish
no matter what their Lewis number
is.

1 — 25

Stability of a premixed counterflow flame (do for HW)
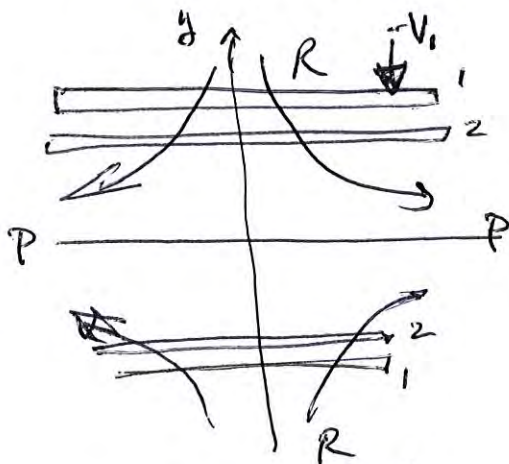
positive stretch

### stable at location 1

proof: $-V_1 = 40 \text{ cm/s}$

$S_L = 40 \text{ cm/s}$

perturb flame to location 2

$-V_1 = 35 \text{ cm/s}$

$S_L = 40 \text{ cm/s}$

flame propagates fwd to larger y → to location 1
moves at 5 cm/s

∴ positive stretch = stable
negative stretch = unstable
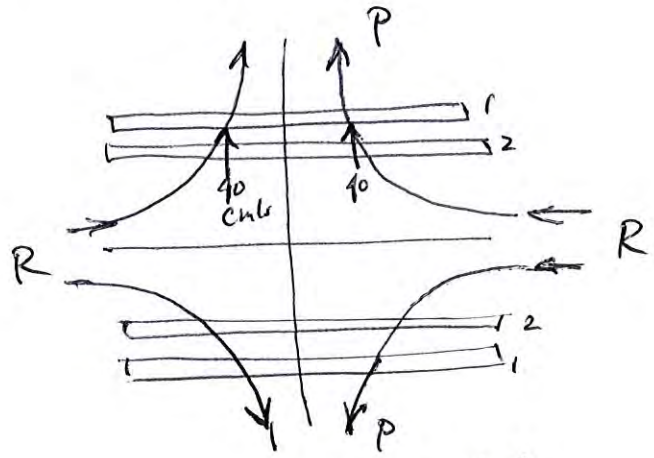
negative stretch

unstable at location 1

proof: $-V_1 = 40 \text{ cm/s}$

$S_L = 40 \text{ cm/s}$

perturb flame to location 2

$-V_1 = 35 \text{ cm/s}$

$S_L = 40 \text{ cm/s}$

flame will propagate toward stag pt. moves at 5 cm/s
to new location $-V_1 = 30 \text{ cm/s}$
will go to stag. pt!

final position —

"finds a stable position" positive stretch

initially
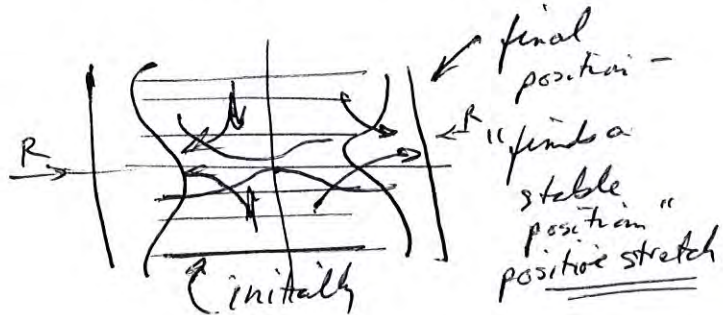
Outline for Monday = Physical concepts

Motivation -   premixed is the way of the future – low NOx, CO, soot

What problems   are important ?

Background   what does turbulence do ?
                        what do we need to model and to measure ? turbulent
                        burning velocity, flame surface density, reaction rate

Turbulent reaction rate

Probability density function   helps to model turbulent reaction rate

Fuel air mixing   and Flame stability

3

Good references

Fundamentals of Turbulent and Multiphase Combustion Kenneth K. Kuo and Ragini Acharya, 2012 John Wiley & Sons, Inc.

Turbulent Combustion, N. Peters, Cambridge U. Press, 2000

Libby, P.A, Williams, F.A., Turbulent Reacting Flows, Academic Press, 1994

Turns, S., An Intro to Combustion, McGraw Hill, 2000

Lewis, B. and von Elbe, G., Combust. Flames, Explosions, Academic Press, 1961

Peters N. Laminar flamelet concepts in turbulent combust. Proc Comb Inst 21 1986

 C. K. Law and C. J. Sung, Structure, aerodynamics, and geometry of premixed flamelets, PECS, 26, 4-6, 2000, 459-505RS

J. F. Driscoll, Turbulent premixed combustion: flamelet structure and turbulent burning velocities, Prog Energy Combust Sci 34, 91-134, 2008.

4